Doctoral Dissertations   Student Scholarship

Fall 2007

Analytical model development and experimental investigation of process model size effects in microforming

Richard M. Onyancha
University of New Hampshire, Durham

Follow this and additional works at: https://scholars.unh.edu/dissertation

ANALYTICAL MODEL DEVELOPMENT AND EXPERIMENTAL

INVESTIGATION OF PROCESS MODEL SIZE EFFECTS IN

MICROFORMING

BY

RICHARD M. ONYANCHA

Bsc. (hons), University of Nairobi, 1987

Msc., Brunel University, 1990

DISSERTATION

Submitted to the University of New Hampshire

in Partial Fulfillment of

the Requirements for the Degree of

Doctor of Philosophy

in

Mechanical Engineering

September, 2007

UMI Number: 3277144

INFORMATION TO USERS

The quality of this reproduction is dependent upon the quality of the copy submitted. Broken or indistinct print, colored or poor quality illustrations and photographs, print bleed-through, substandard margins, and improper alignment can adversely affect reproduction.

In the unlikely event that the author did not send a complete manuscript and there are missing pages, these will be noted. Also, if unauthorized copyright material had to be removed, a note will indicate the deletion.

UMI®

UMI Microform 3277144

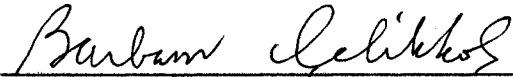Copyright 2007 by ProQuest Information and Learning Company.

All rights reserved. This microform edition is protected against unauthorized copying under Title 17, United States Code.

ProQuest Information and Learning Company
300 North Zeeb Road
P.O. Box 1346
Ann Arbor, MI 48106-1346

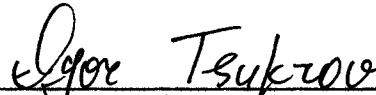This dissertation has been examined and approved.

Dissertation Director, Brad L. Kinsey,
Associate Professor of Mechanical
Engineering
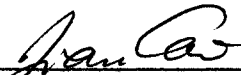
Barbaros Celikkol, Professor of
Mechanical Engineering

Robinson Swift, Professor of Mechanical
Engineering

Igor Tsukrov, Associate Professor of
Mechanical Engineering

Jian Cao, Associate Professor of
Mechanical Engineering, Northwestern
University

7/31/2007

Date

DEDICATION

This dissertation is dedicated to my wife Beatrice, and our three sons (Edward,

Enock and Elvin) for their sacrifices that made it possible for it to be completed.

iii

ACKNOWLEDGEMENT

PREFACE

This work deals with the development of new analytical models that can be used in the design of forming processes at the micro scale level. Microscale forming processes are those that fabricate parts with at least two dimensions in the sub-millimeter range. Macroscale processes cannot simply be miniaturized to produce microparts because of size effects. Size effects are caused by the orientation, size and position of grains within the specimen and simply the smaller size of the specimen. These size effects are due to the small number of grains through the dimension of interest. The following effects were investigated in this research:

- Material property size effects

- Process model assumption size effects

- Deformation size effects

It is shown that these size effects exist in the processes that were studied vis microbending and microextrusion. New analytical process models are proposed that account for these size effects. These proposed models are validated by empirical data from microbending experiments using brass (CuZn15) and 1100 Aluminum specimens and microextrusion experiments using brass CuZn30.

v

TABLE OF CONTENTS

LIST OF TABLES

ix

LIST OF FIGURES

xi

ABSTRACT

ANALYTICAL MODEL DEVELOPMENT AND EXPERIMENTAL INVESTIGATION OF PROCESS MODEL SIZE EFFECTS IN MICROFORMING

by

Richard M. Onyancha

University of New Hampshire, September, 2007

With the emergence of micromanufacturing technologies, a critical need to develop process models that can accurately predict the required parameters, such as process forces, has arisen. As with the manufacturing processes themselves, macroscale process models can not effectively be used at the microscale due to size effects, i.e. changes in material and process parameters with miniaturization. Size effects with respect to material properties and frictional conditions have been demonstrated in past research. This dissertation demonstrates the existence of size effects due to process model assumptions and specimen deformation.

The two processes investigated in this research were microbending and microextrusion. For bending, the dissertation focuses on two macroscale process model assumptions that may not hold at the microscale. These are the assumptions of a logarithmic strain distribution through the sheet thickness and that of a curved wall profile for the deformed sheet. For extrusion the focus is on the increased shear due to deformation size effects. The term in the process

model that is used to calculate the shear deformation force was altered to account for this increased shear. Using existing macroscale models, new models are proposed that include size effects for the two processes.

The new models were evaluated by comparing the predicted results to both experimental and finite element simulation results. These new models showed significantly improved predictions of the peak forces for the microscale processes investigated. This is significant because sheet metal forming processes such as bending and extrusion are ideal fabrication techniques for mass production of parts at very competitive unit costs.

INTRODUCTION

Demand for micro components and systems in the global market continues to increase significantly. Nearly 1.8 billion Micro Electro Mechanical Systems (MEMS) devices were shipped in 2005, for revenues of just under $7 billion, and the projected shipment growth over the next five years is 11% [1]. Developments in technology have led to the ability to produce progressively smaller devices capable of performing functions that are more complex. The small components, incorporated in these devices are produced by various technologies such as micro-machining, etching (both wet and dry), photolithography, thin film deposition, the LIGA process, which involves lithography, electroforming and plastic molding, and to a small extent, forming processes such as extrusion and bending. The Integrated Circuit (IC) based techniques, however, can only generate 2D and 2½D geometries and are limited in the materials available for use. Furthermore, these fabrication methods require the use of expensive clean room space and processes, are slow, and the relative accuracy (i.e. feature tolerance to object size) is of the order of 10^{-1} to 10^{-3}. See Figure 1 [2].

Recently, some traditional manufacturing processes that are cost effective, provide design flexibility and are environmentally friendly have been investigated for use at the microscale level (e.g. micromachining and microforming). These techniques can be used to produce precision 3D features using a wide variety of materials at very competitive unit costs. They also provide flexible design

1

capabilities and relative accuracies of between 10^{-3} and 10^{-5} with high aspect ratios (feature size to width).
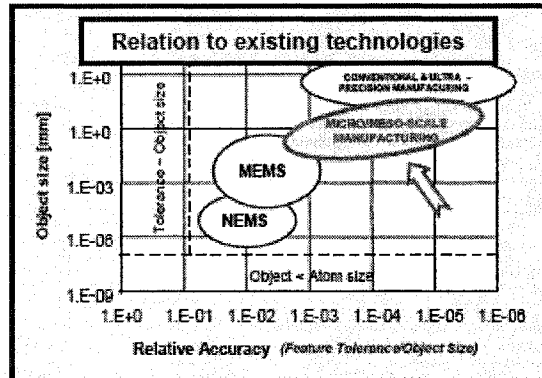
Figure 1 Micromanufacturing size/ precision domain [2]

As with the selection of macroscale manufacturing processes, the factors that determine the manufacturing method used for microscale components such as those shown in Figure 2 include specific design requirements such as size of component, accuracy, cost per unit part and environmental effects. The processes investigated in this dissertation are the bending and the forward extrusion of micro-sheet metal components. Microbending and microextrusion are typical fabrication methods for components such as micro-connectors and contact springs for the electronics industry. These microforming methods are used because they provide very competitive unit costs and involve plastically deforming material stock into particular shapes and sizes as dictated by the process geometry. The polycrystalline plasticity models that are used in the analysis and design of these processes at the macroscale level are based on physical insight and are reasonably tractable [3]. Because plasticity is a very

2

complicated phenomenon, it is difficult to capture all its attributes in a single model especially when different length scales are considered.
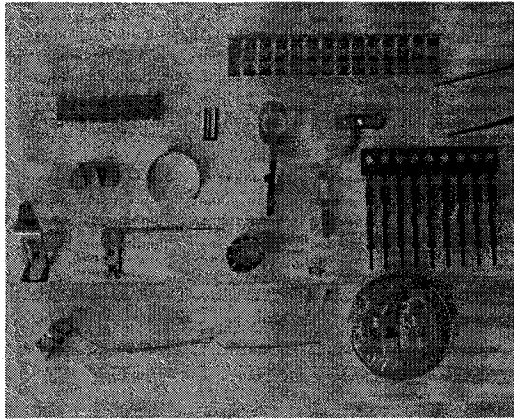
Figure 2 Examples of microformed parts [4]

Macroscale manufacturing processes cannot simply be miniaturized to produce components on the microscale due to "size effects". Microscale components may contain only a few grains through the dimension of interest and thus there are only a few grains located in the deformation zone. Size effects are caused by the orientation, size and position of grains within the specimen [5] and simply the smaller size of the specimen. Armstrong [6] and others have categorized these size effects into specimen size effects and grain size effects. Past research has shown that size effects cause the material properties and the frictional effects to vary as the ratio of feature size to grain size decreases. In scaled double cup extrusion experiments with CuZn15 specimens, using standard extrusion oil for lubrication, Tiesler [7] showed a significant increase in friction with decreasing specimen size from 4.0 to 0.5 mm in diameter (see

3

Figure 3). This friction factor was determined by comparing the wall heights in the experiments to numerical simulation results. This phenomenon was attributed to the presence of open and closed lubrication pockets. Using this friction model, Tiesler [7] concluded that closed lubricant pockets attenuated friction and surface flattening with decreasing specimen size.
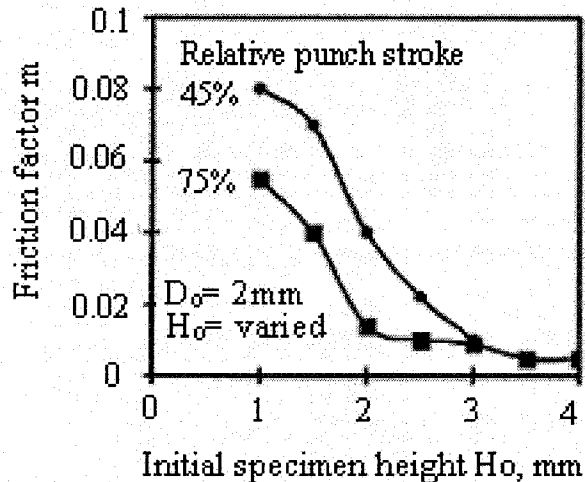
Figure 3 Variation of friction factor with increasing specimen size for a double cup extrusion process [7]

Krishnan et al. [8] investigated friction using a dry forward microextrusion process. Numerical simulations were conducted as well as experiments. The extrusion forces and final pin lengths from the finite element simulations and experiments were compared in order to determine an effective frictional coefficient for the experiments. Their research showed that the frictional behavior at the microscale is fundamentally different from that at the macroscale as is evident by the low extrusion force for the smallest diameter case with a correspondingly shorter pin length. Finally, Mori et al. [9] showed, using a stored energy Kolsky bar test with varying pressure and contact area, that the friction

4

coefficient is independent of grain size for various pressure values and contact areas. For bending, it has been shown from previous research, [10] that about 10% of the applied work is expended as friction work on the die shoulders.

The material property that has been specifically investigated for size effects that is relevant to this research is yield stress. When a metal is plastically deformed, the material behavior is characterized based on the stress and the strain induced. As the number of grains through the thickness reduces, the yield stress decreases as shown in Figure 4 for both bending and uniaxial tension tests [11]. A minimum occurs at a sheet thickness to grain size ratio of approximately one before it shows an increase in the yield stress as the ratio reduces further. The data to the left of the minimum yield stress shows considerably more scatter than that to the right due to the sometimes favorable and sometimes unfavorable orientation of the grains in the material. [12]. The increase in yield stress is attributed to strain gradient effects as more geometrically necessary dislocations are required in a smaller area as the specimen size is decreased. For data to the right of the minimum in Figure 4 , the yield strength decreases with miniaturization because a higher surface grains to interior grains ratio occurs. Surface grains experience fewer restrictions than interior grains and thus require less force to deform [11, 13]. The specimens used in these tension tests were in the microscale only with respect to the thickness dimension; the gauge length and width were still macroscale or mesoscale in size. The bending specimens on the other hand had no dimension in the microscale range since the sheet thickness, which was the smallest

5

dimension, was kept constant at 1 mm [11] but the number of grains through the thickness was reduced progressively. It should be noted that Cao et al. [14] did not see an increase in yield strength with reduction of the diameter while keeping the grain size constant. Their study of cylindrical tensile specimens with a diameter varying from 0.4 mm (2 grains through the thickness) to 1.32 mm (6 grains through the thickness), though did not include diameter-to-grain size ratios below 2. They explained this difference to be due to the fact that the specimen diameters were still at least twice that of the grain size. However, an increase in scatter of the data similar to that found by Raulea et al. [11] was observed when the diameter was reduced.
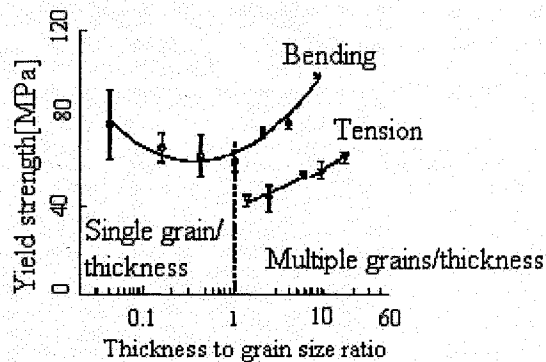
Figure 4 Variation of tension and bending yield strength with thickness-to-grain size ratio [11]

Another type of size effect which has been demonstrated in microextrusion is deformation size effects. For a microextrusion case (0.76 to 0.57 mm reduction), Parasiz et al. [15] found out that when the grain size became comparable to specimen feature size, the total deformation behavior of the cross sections was

6

dominated by the deformation of individual grains as was observed through microstructural analyses. This resulted in curving in the final shape of the pins. The curving observed was random in magnitude and direction for each pin size. In addition, microindentation investigations performed by the same authors showed higher hardness values for the larger grain size pins, which seems to contradict the Hall-Petch relationship. The Hall-Petch relationship indicates that the strength of the larger grain size material should be lower than that of smaller grain size material. The reason for this increased hardness is the higher shear deformation that occurs at the center of the pin because of the large grain sizes and small feature sizes. Another type of size effect that exists in microforming is with respect to process model assumptions. This type of size effect will be discussed in detail in this thesis with a focus on microbending and microextrusion.

Chapter I of this dissertation discusses bending theory and some of the assumptions that are made for macroscale process models and their applicability for microbending. Specifically the assumptions made about the strain distribution within a thin metal sheet and the deformed sheet profile are discussed. This chapter also provides the details of the experimental setup that was used to determine the material properties that were used to characterize the two materials that were investigated viz. 1100 Aluminum and α-brass (CuZn15). The microbending testing equipment and procedures are also discussed. The various models investigated are also presented and the predicted results from these models compared with experimental data.

7

Chapter II follows a similar pattern in presenting the work done in microextrusion whereby some background theory is provided first followed by the experimental work performed at Northwestern University, and then the analytical models (macroscale and microscale) are discussed. Finally the predicted results are compared to the experimental results.

Chapter III discusses the possible use of commercially available finite element software in the simulation of microscale forming processes. This is very preliminary work intended to find out how these packages handle microscale processes.

The conclusions are presented in Chapter IV. Final remarks about process model size effects with regard to microbending and microextrusion are given along with possible future work

8

CHAPTER I

BENDING

Background

Regardless of the size scale of interest, accurate process models provide essential information when designing a manufacturing process. For the case of bending, the required bending force to deform the material is the critical process parameter and much research in this area has been conducted [16 – 19]. Eckstein & Engel [20] measured the maximum bending forces for different orientations to the rolling direction and different grain sizes. They concluded that size effects occur during miniaturization of a bending process due to the small number of grains located in the deformation area and due to the increased share of surface grains. Diehl et al. [21] also investigated microscale bending of sheet metal (copper and aluminum) with regard to spring-back as a function of the microstructure and process parameters. They concluded that the sheet thickness to grain size ratio has a significant influence on the springback of metal foils. As Diehl et al. [22] indicated process parameters and the way sheet metal specimens behave during bending processes are influenced by two opposing size effects. The first effect is that of decreasing material strength due to an

9

increasing share of surface grains with miniaturization. The second is the increasing strength due to a higher density of geometrically necessary dislocations caused by the increased strain gradients as the sheet thickness is decreased. The grain size effect is a function of the number of grain boundaries present in a volume. These grain boundaries act as barriers for dislocation motion and require "internal stress concentrations that are proportional to the grain size to propagate plastic flow through the aggregate" [6]. Thus, the material strength increases with decreasing grain size according to the well known Hall-Petch effect. Such size effects lead to variations in the material and process parameters at the microscale as discussed earlier.

One of the goals of this dissertation is to determine if the process models traditionally used for macroscale bending can accurately predict the peak process force in microscale bending or if size effects exist with respect to assumptions in these process models. Two traditional models were investigated. One of the models used is based on elementary bending theory and it predicts the peak bending force, as a function of the specimen width, thickness, tensile yield strength and the die opening size [23]. The other model developed by Wang et al. [24], incorporates elastic, elasto-plastic, and plastic regions in a non-linear formed wall to predict the entire bending force versus punch displacement curve for a 3-point bending (air bending) process. This model has been shown to predict the peak force for a 3-point bending operation accurately for macro scale specimens [24].

Two microscale models were developed based on the model by Wang et al. [24], and included variations of two process model assumptions i.e. process model size effects. The macroscale model developed by Wang et al. assumes a nonlinear strain distribution through the sheet thickness and a curved wall sheet profile with a plastic, elasto-plastic and elastic regions. The first microscale model proposed assumes a linear strain distribution through the sheet thickness while the second one assumes a straight wall sheet profile from the point of contact of the die to the free end of the sheet and a linear strain distribution through the sheet thickness. For microscale sheets with thicknesses on the order of the grain size, it is more reasonable to assume a linear strain distribution because no significant non-linearities are expected in the strains within a single grain or a few grains. Similarly for microscale bending operations in which the die opening is of the order of a few grain sizes, the sheet profile from the point of contact of the die to the free end can be approximated to be a straight wall since there is not sufficient space for curvature to occur.

Microbending experiments were carried out in our laboratory at UNH to provide data for evaluation and validation of two new models that were developed as part of this work. Additional data was obtained from bending experiments by Lehrstuhl für Fertigungstechnologie (LFT) Laboratory for Forming Technologies at the University of Erlangen-Nuremberg, Germany [25]. The two traditional models and two additional models developed in this work were then compared. The data from LFT included data from flanging experiments for brass (CuZn15) of 0.1 and 0.25 mm thickness sheets with approximately fifteen grains

11

or less through the thickness and 0.5 mm thickness sheets that had 50, 18, and 7 grains through the thickness depending on the heat treatment used. Specimens with approximately fifteen grains or less through the thickness are considered microscale based on work by Hansen [26]. The data from the microbending experiments performed in our laboratory at UNH was for 1100 Al of 0.127, 0.254, 0.508, 0.813 and 1.588 mm thickness specimens. Samples of these specimens were heat treated at 450 °C, 550 °C 575 °C and 600°C to increase the grain size. In the following section, the properties of the materials used in the microscale experiments including size effects are discussed. The section after that discusses the experimental setup and procedures of the microbending experiments. In subsequent sections, each of the process models is discussed in detail and the predicted results from each of the models are compared with experimental data for both microscale and macroscale cases.

The microbending experiments that were used to validate the models were conducted at LFT, Germany for CuZn15 and at UNH for 1100 Aluminum specimens. The set up used in both of these labs was 3 point bending. The CuZn15 specimens had a constant width of 10 mm while the 1100 Aluminum specimens had a width equal to 10 times the sheet thickness to provide scaling according to the theory of similarity. The width of the sheet was large relative to the sheet thickness to ensure plane strain conditions during the testing.

It should be noted that the bending set up used in Wang et al.'s model [24], which was used here and is the basis for the other models that were developed, was 3-point bending. While our internal experiments were 3-point

12

bending, the experimental bending force data from LFT is for flanging experiments [25]. Flanging is reasonably assumed to be equivalent to half of a 3-point bending operation with the punch and die interchanged as shown in Figure 5. The binder and die in flanging provide a horizontal constraint that is analogous to that provided by symmetry in 3-point bending, as the horizontal center of the sheet is constrained from moving in the horizontal direction. The die opening, L_d, for the 3-point bending is twice that for flanging (see Figure 5).

(a)

(b)
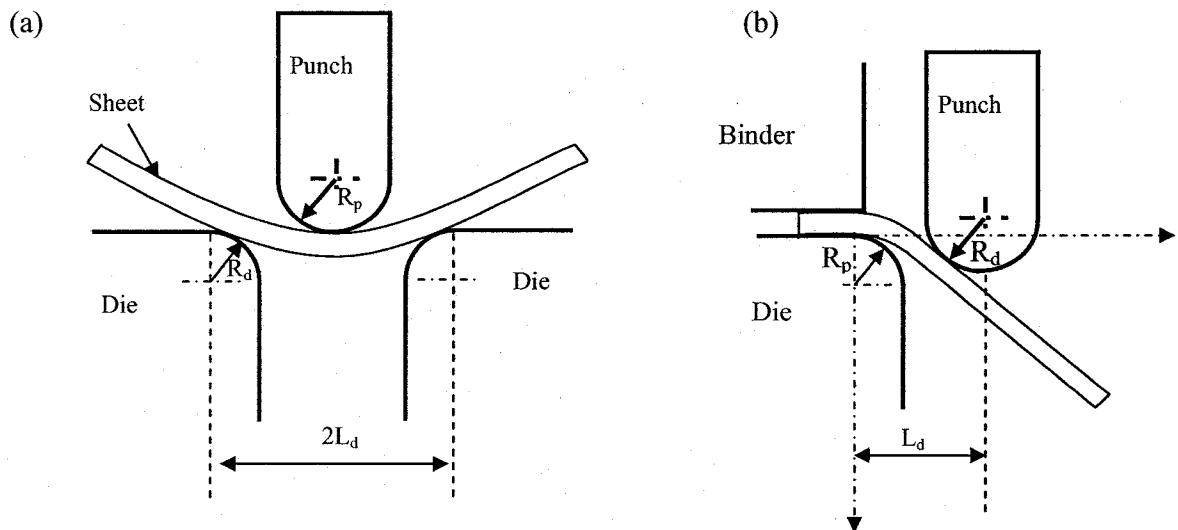
Figure 5 Process schematic for (a) 3-point bending and (b) flanging

Before specifics with respect to the bending experimental set up are presented, properties with respect to the materials used will be provided. As indicated earlier the bending experiments that were conducted in our lab used 1100 aluminum of the following sheet thicknesses: 0.127 mm (0.005 inch), 0.254 mm (0.010 inch),

13

0.508 mm (0.020 inch), 0.813 mm (0.032 inch) and 1.588 mm (0.0625 inch). This material was selected because of it's wide application especially in the electronics industry and it's ability to grow up to very large grains. It was intended to prepare specimens with different number of grains through the thickness so that we could investigate grain size effects for the different thicknesses. This material is divided into four broad sections viz.

1. Material properties in which the materials and thicknesses used are provided. This section discusses the details of determining the different material properties that are needed in the process models. The materials that were selected for this investigation were α brass (CuZn15) and 1100 aluminum with the thicknesses indicated against each material below:

    a. CuZn15 – 0.1 mm, 0.25 mm and 0.5 mm

    b. 1100 Al – 0.127 mm, 0.254 mm, 0.508 mm, 0.813 mm and 1.588 mm (0.005 inch, 0.010 inch, 0.020 inch, 0.032 inch and 0.0625 inch)

    These specimens were heat treated to different temperatures to produce specimens with varying number of grains through the sheet thicknesses so that we could investigate size effects with respect to material properties and then apply these experimental material constants to the process models being studied.

2. Experimental set up in which the details of the microbending experiments that were conducted at UNH are provided

3. Check of the measurement system for accuracy

14

4. Experimental results from the microbending tests are presented in the final section of this chapter

Determination of Grain Sizes

The determination of average grain sizes of the material specimens was performed in accordance with ASTM E112 standard procedures. The techniques outlined in this standard are only used to determine the average planar grain size i.e. the characterization of the 2D sections revealed by the sectioning plane. For the very coarse grains (>1000 μm), the planimetric procedure was used in which the number of grains per unit area was obtained and used to determine the ASTM grain size number from which the average grain size was calculated. For the other specimens the circular intercept procedure (Hilliard Single-Circle Procedure) was used. This procedure involves counting the actual number of grain boundaries that intercept a circle. This number is then used to determine the mean lineal intercept length which is then used to determine the ASTM grain size number according to the ASTM E112 standard from which the average grain size was calculated. For each specimen, a number of pictures of the microstructure were taken and the average ASTM grain size number obtained by taking the algebraic mean of all the different samples. Figure 6 shows an example micrograph for the 0.813 mm 550 °C case, with a circle used to determine the number of grain boundary intercepts.

Table 1 Variation of the average grain sizes and the number of micrographs used to determine grain size for 1100 Aluminum

Thickness, t, mm	Heat Treat Temp. °C	Max. average grain size, µm	Min. average grain size, µm	Mean average grain size, µm	Number of micrographs used
0.127	As received	-	-	20.0*	-
	325	27.05	22.00	24.7	4
	450	35.30	32.00	33.6	2
	550	69.93	38.82	51.0	8
	575	87.28	49.95	63.7	6
0.254	As received	-	-	22.0*	-
	325	29.36	24.63	26.7	4
	450	50.76	47.49	49.1	4
	550	61.19	50.74	55.8	4
	575	48.32	17.02	34.8	19
0.508	As received	36.73	35.07	35.6	3
	325	57.51	52.84	55.2	2
	450	42.52	35.59	38.0	6
	550	47.65	43.47	45.5	3
	575	-	-	1065	1
0.813	As received	-	-	37.2	1
	325	-	-	60.3	1
	450	64.51	60.00	62.2	3
	550	83.26	64.61	73.3	5
	575	99.74	71.94	71.9	5
1.588	As received	43.56	41.22	42.4	3
	325	-	-	44.0*	-
	450	47.23	43.65	46.5	3
	550	51.18	49.94	50.6	2
	575	-	-	1363.0	1

* Estimated using extrapolation techniques

16
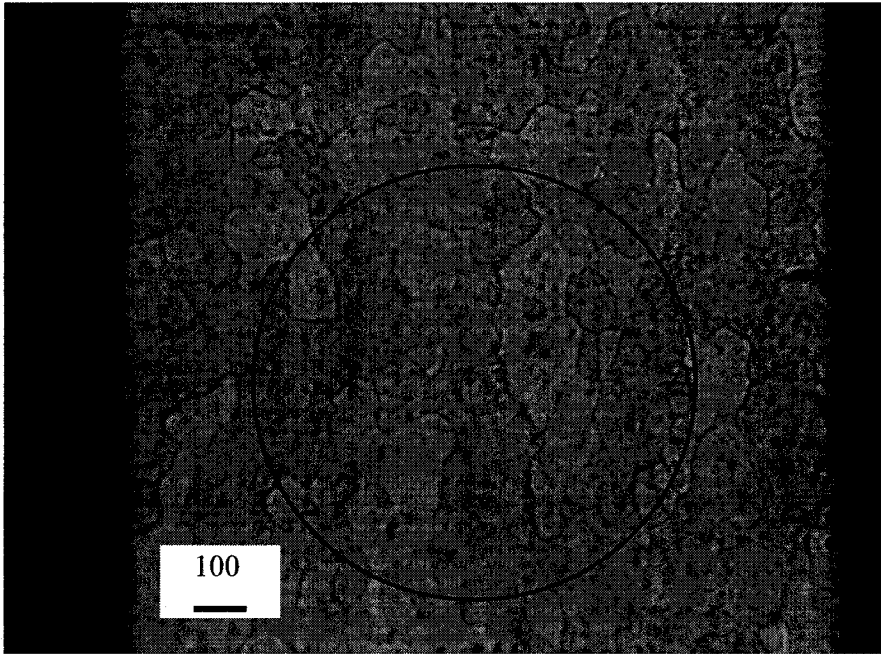
Figure 6 Micrograph for 0.813 mm, 1100-H14 Aluminum specimen heat treated at 550 °C for one hour

Most of the as received specimens were found to have very elongated grains along the rolling direction, see Figure 7, as opposed to those that were heat treated as can be seen in Figure 6. In some cases, such as the 0.127 mm and 0.254 mm as received specimens, the microstructure observed was such that no grain sizes could be obtained. These specimens showed long dark bands. The grain sizes for these cases were estimated by extrapolating from the data from the other heat treatment temperatures. An interpolation method was used to determine the grain size for the 1.588 mm 325 heat treat case because the microstructure did not show a clear grain structure.

17
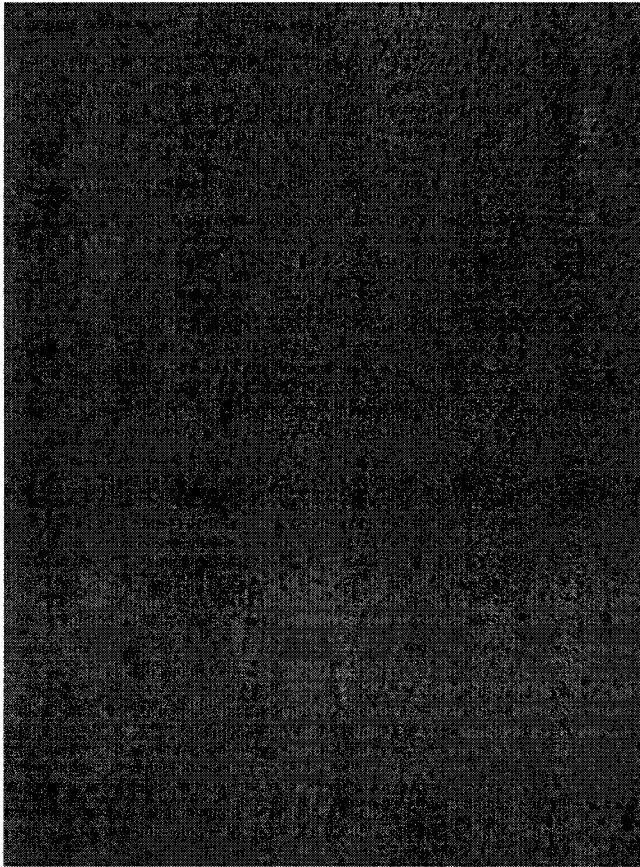
Figure 7 Grain structure of the 0.813 mm 1100-H14 Aluminum as received specimen

Hall Petch Grain Size Effects on Material Properties

The characteristic properties for the materials heat treated at different temperatures were determined by conducting uniaxial tensile tests. The test specimens were prepared according to ASTM E8 standards for 12.7 mm (½ inch) wide specimens and tested on a model 350 Instron machine. The specimens had a gage length of 50.8 mm (2 inch). These specimens were then heat treated at 325°C, 450°C, 550°C and 575°C for one hour and air cooled before being tested. The tensile tests were conducted at a constant rate of 0.010 mm/sec. A total

18

number of five samples were used for each case and average values were determined. From these tests, true stress (σ) versus true strain (ε) curves were generated for each thickness and heat treatment case from which the average pertinent material properties (Young's modulus, tensile yield stress, strength coefficient and work hardening exponent) were obtained, see Table 2. A power hardening law

$$\sigma = K\varepsilon^n \tag{1}$$

where, K is the strength coefficient and n is the work hardening exponent, was assumed and validated by comparing the experimental stress-strain curves to those generated by assuming the power hardening model. This model was found to be valid for 1100 Aluminum as can be seen from Figure 8. Note that strain rate effects were not considered in this constitutive relationship due to the quasi-static nature of the tests.

19

Table 2 Variation of material constants with sheet thickness and grain size for 1100 Aluminum

Sheet thickness, mm (Temper)	Heat Treatment	Average Grain Size, μm	Average Number of Grains	Average Values		
				Yield Stress, MPa	Strength Coeff. K, MPa	Work Hardening Exponent, n
0.127 (H18)	AR	20	6.4	167.7	235.8	0.059
	325	24.7	5.1	32.5	199.4	0.324
	450	33.6	3.8	30.8	179.3	0.300
	550	51.0	2.5	28.9	173.0	0.314
	575	63.7	2.0	24.8	145.1	0.291
0.254 (H18)	AR	22	11.5	200	252.6	0.038
	325	26.7	9.5	43.6	180.5	0.248
	450	49.1	5.2	36.4	181.9	0.272
	550	55.8	4.6	31.2	182.7	0.296
	575	31.5	8.1	30.2	177.8	0.277
0.508 (O)	AR	35.6	14.3	41.9	199.4	0.299
	325	55.2	9.2	29.1	148.8	0.263
	450	38.0	13.4	27.8	162.6	0.279
	550	45.5	11.2	27.5	168.1	0.307
	575	1065.0	0.5	20.7	149.2	0.369
0.813 (H14)	AR	37.2	21.9	109.3	144.6	0.048
	325	60.3	13.5	23.2	132.3	0.241
	450	62.2	13.1	22.8	136.9	0.246
	550	73.3	11.1	21.4	138.9	0.254
	575	71.9	11.3	20.4	180.1	0.325
1.588 (O)	AR	42.4	37.5	46	160.2	0.232
	325	44.0	36.1	29.3	150.8	0.257
	450	46.5	34.2	27.6	160.4	0.265
	550	50.6	31.4	17.1	165.0	0.361
	575	1363.0	1.2	21.9	201.1	0.419
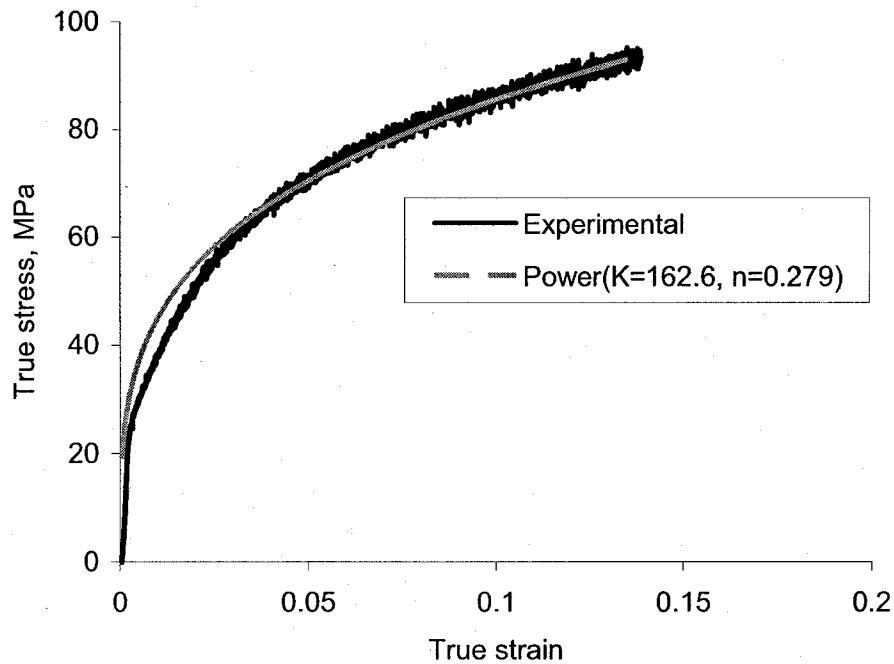
Figure 8 Comparison of experimental true tensile stress versus true tensile strain and power hardening model simulated plots for 0.5 mm thick 1100 Al specimens heat treated at 450°C for 1 hour.

As can be seen from Table 2 the grain size increases with increasing heat treatment temperature for all cases except 0.254 mm 575 °C and 0.508 mm 325 °C. As noted earlier grain coarsening results when a metal is heated above its recrystallizing temperature and at sufficiently high temperature rapid grain growth, such as seen for the O temper cases, occurs due to secondary recrystallization (exaggerated grain growth). Heating beyond the recrystallization temperature leads to grain growth due to one of several mechanisms at play [27]:

- Gradual uniform growth due to elimination of small grains with unfavorable shapes and orientations. This mechanism is enhanced by the presence of small recrystallized grains, high temperatures

21

and extensive heating. This mechanism is restricted by the presence of impurities and intermetallic compounds of elements such as chromium and manganese, which slow down the process, pin the grain boundaries and prevent further movement.

- Exaggerated growth (secondary recrystallization) which leads to rapid growth of a few grains because the effect of impurities and intermetallic compounds is attenuated or lost at high temperatures through solution or changes in particle size. The first few grains that experience this effect act as growth centers consuming other potential growth centers leading to very large grains. Other factors that promote this growth are small primary grain size and well developed annealing texture.

As was discussed in the introduction, size effects with respect to material properties exist as the size of specimens decreases. Using the tensile test data, the dependence of material constants on both grain and specimen size was determined. The 0.127 mm and 0.254 mm aluminum specimens were fabricated from 1100-H18 Al because of non-availability of the zero temper (1100-O) at these thicknesses, while 0.813 mm specimens were made from 1100-H14 and the 0.5 mm and 1.588 mm thick specimens originated from 1100-O stock. The 1100-O aluminum is fully annealed. The 1100-H18 on the other hand is highly cold worked (equivalent to 75% cold reduction). The intermediate temper of H14

22

indicates that the material has been cold worked (equivalent to 37.5% cold reduction).

The second set of experimental force data was obtained from LFT [25]. As discussed previously the material used in these experiments was brass (CuZn15), in its spring hard state (non-heat treated), heat treated at 475°C for 2.5 hours (Heat Treat. 1), and heat treated at 700°C, 650 °C, or 600°C (Heat Treat. 2) for two hours for the 0.1, 0.25, and 0.5 mm thickness specimens investigated respectively. The materials were heat treated to increase the grain sizes and therefore reduce the number of grains through the thickness of the sheet as shown in Table 3. This heat treatment also made material of different thickness values, t, comparable with respect to the grains through the thickness. Other dimensions included a constant width of 10 mm (thus a plane strain condition since width $\geq 20t$), a specimen length of $6t$ and a die radius, R_d, of $4t$. From the tensile test data that was obtained from LFT [25] to enable material characterization, it was also shown that the stress –strain of CuZn15 can be approximated by the power law, see Figure 9.

23

Table 3 Variation of material constants with sheet thickness and grain size for CuZn15 [25, 28]

Sheet Thickness, t (mm)	Heat Treatment	Grain Size (μm)	Number of Grains Through Thickness	Average Values		
				Yield Stress, σ_y (MPa)	Strength Coeff., K (MPa)	Work Hardening Exponent, n
0.1	Non-Heat Treat.	17	6	356.3	431.8	0.036
	Heat Treat. 1	23	4	96.2	525.8	0.339
	Heat Treat. 2	53	2	60.5	471.9	0.412
0.25	Non-Heat Treat.	20	13	413.5	510.0	0.040
	Heat Treat. 1	23	11	109.9	557.3	0.341
	Heat Treat. 2	65	4	66.2	645.1	0.501
0.5	Non-Heat Treat.	10	50	346.1	492.8	0.070
	Heat Treat. 1	28	18	104.0	576.1	0.353
	Heat Treat. 2	71	7	70.0	587.2	0.432
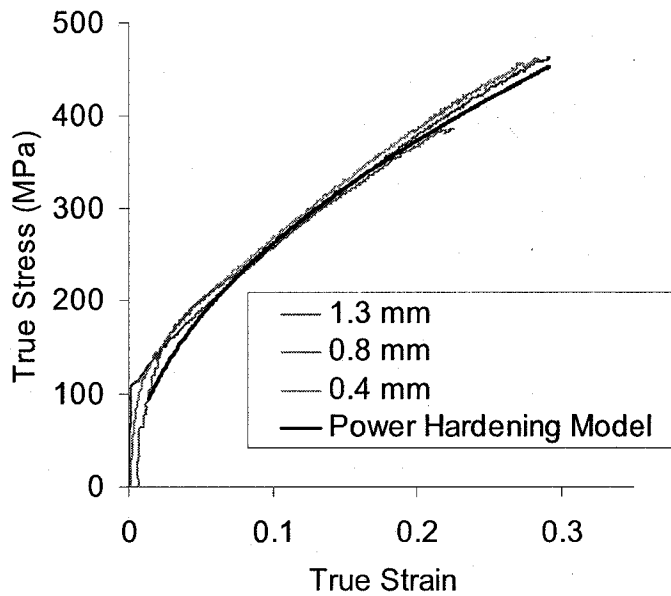
Figure 9 Comparison of experimental true stress versus true strain plots for different specimen thicknesses and the power hardening model simulated plot for CuZn15 heat treated at 475°C for 2.5 hours

For the 1100 Aluminum, the yield stress shows the following trends with increasing heat treatment temperatures:

- 0.127 mm – decreases

- 0.254 mm – decreases

- 0.508 mm – decreases

- 0.813 mm – decreases

- 1.588 mm – decreases except for the 550°C case which shows a
  lower value than the 575 case

For brass (CuZn15) the yield stress decreases, with increasing grain size, as expected from the Hall-Petch relationship.

25

The hardening exponent *n* shows greater and more consistent variance for brass than it does for aluminum. For brass, the work hardening exponent increases as the grain size increases, due to the increased annealing. For aluminum, there is no clear pattern seen for the 0.127 mm specimens while for the other sizes there is a general increase with increasing grain size.

The strength coefficient does not have a clear pattern for both materials. For aluminum, no clear pattern is seen for the strength coefficient but the H18 temper material in general shows higher values followed by those of the O temper. For the 0.1 mm thickness case for brass, the strength coefficient increases with an increase in grain size for Heat Treatment 1 and then decreases as the grain size increases with Heat Treatment 2. For the 0.5 mm thickness, the strength coefficient increases with increasing grain size. Microscale tensile test data for round specimens from Cao et al. [14] was also evaluated, and a similar inconsistent effect for the strength coefficient was found, see Table 5. The cause of this phenomenon is the methodology to determine the strength coefficient value from the experimental data. The strength coefficient is determined from the intersection of a log stress versus log strain plot with a log strain value of zero, which is equal to a unity strain value. The decreasing yield stress and the increasing strain hardening exponent are competing factors, which lead to either a decrease or an increase in the strength coefficient respectively. Thus, a consistent pattern is not observed for this material parameter.

Experimental Investigations

The bending experiments were performed on a 4448 N (1000 lb) SEM loadstage manufactured by Ernest F. Fullam Inc., NY, see Figure 10. Tooling (a die and a punch) were mounted into the loading stage to vary the tooling dimensions for the various material thicknesses investigated (i.e. 0.127 mm, 0.254 mm, 0.508 mm, 0.813 mm and 1.588 mm). A schematic of the tooling is shown in Figure 11.

The die and the punch, shown in Figure 11 were fabricated using standard milling of 1018 steel with two different thicknesses 6.35 mm and 15.875 mm ((1/4 and 5/8 inch) for use with specimens of different sheet thicknesses. The smaller thickness was used to fabricate die/punch sets for the three smallest test specimens i.e. 0.127, 0.254 and 0.508 mm (0.005, 0.010 and 0.020 inch) thicknesses while die/punch sets for the two larger specimens viz. 0.813 and 1.588 mm (0.032 and 0.0625 inch) were made from the 15.875 mm steel plate in order to provide the necessary material in the width direction for plane strain conditions. The dimensions of the specimens used in the bending tests were varied in accordance with the theory of similarity, and also to ensure plane strain conditions during the bending process with the width $\geq 10t$. The dimensions of the specimens, dies and punches used are given in Figure 11 and Table 4 along with the scaling factors with respect to thickness (t) for the law of similarity.

27
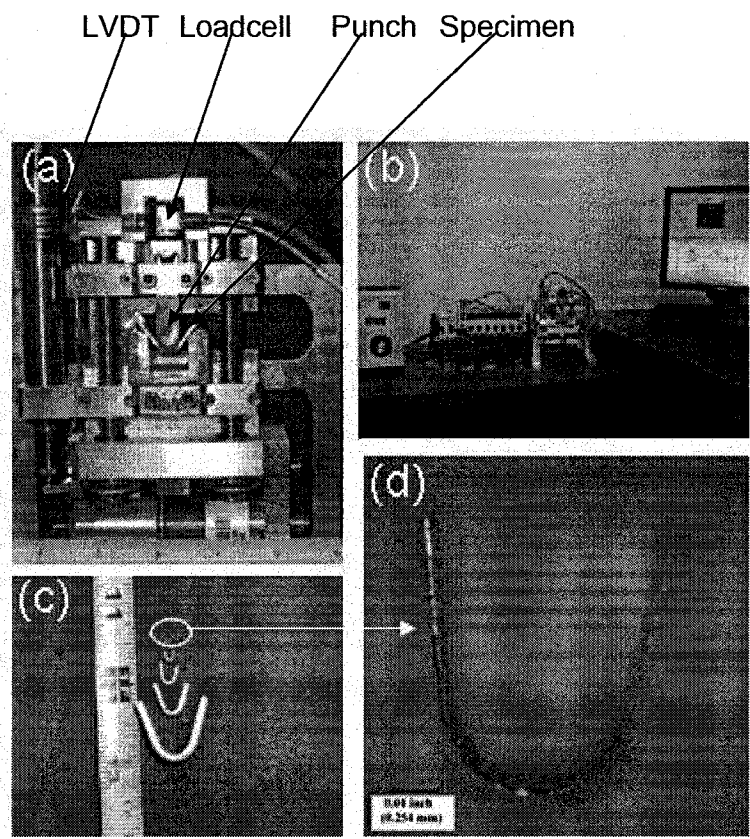
Figure 10 Microbending (a) load stage (b) setup and (c) sample specimens. (d) 0.127 mm thickness specimen
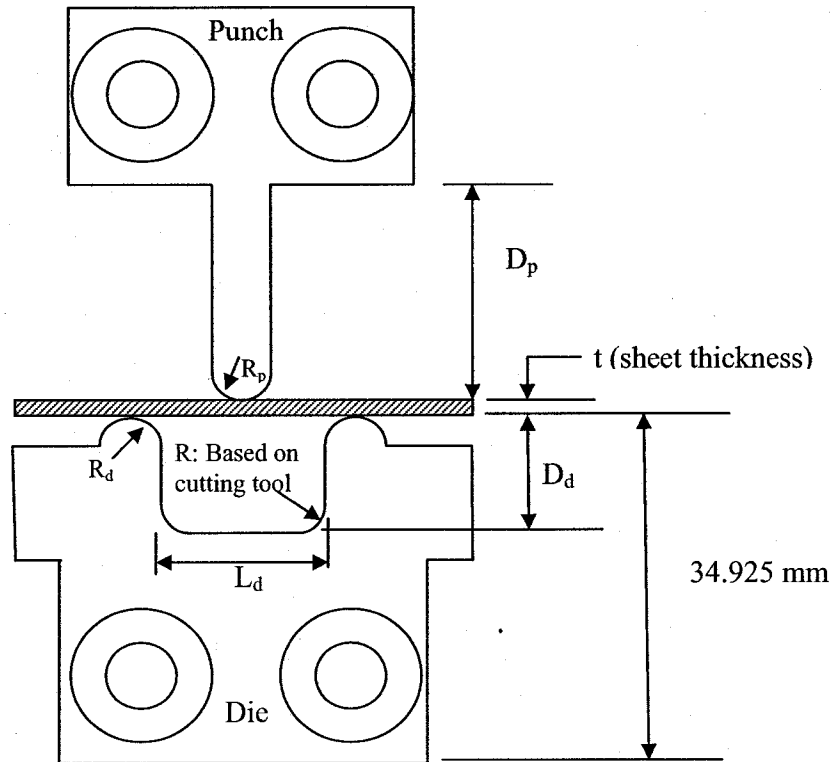
Figure 11 Die and Punch design dimensions (see Table 1 for variable descriptions)

Table 4 Design parameters for the punch and die sets used

Sheet thickness, t, mm	Specimen width W_s, mm	Specimen Length L_s, mm	Die Opening L_d, mm	Die Depth D_d, mm	Die Radius R_d, mm	Punch Height D_p, mm	Punch Radius R_p, mm	Punch Speed, mm/sec
t	10t	26t	10t	12t	3t	14t	3t	-
0.127	1.27	3.302	1.27	1.524	0.381	1.778	0.381	0.03
0.254	2.54	6.604	2.54	3.048	0.762	3.556	0.762	0.04
0.508	5.08	13.208	5.08	6.096	1.524	7.112	1.524	0.05
0.813	8.13	21.138	8.13	9.756	2.439	11.382	2.439	0.08
1.588	15.88	41.288	15.88	19.056	4.764	22.232	4.764	0.15

The motor speed was varied to ensure comparable strain rates for the different specimen sizes. This was in keeping with the theory of similarity. A velocity of 0.1t (mm/sec) was targeted. All of the experiments were slow enough

29

for the process to be considered quasi-static. Due to limitations of the loading stage on which the experiments were performed, the targeted punch speed (0.013 mm/sec) for the smallest specimens could not be achieved. Therefore, a slightly higher speed (0.03 mm/sec) was used. Therefore the punch speed for the 0.254 mm specimens was also increased to be midway between that for the 0.127 mm and the 0.508 mm specimen sizes.

The displacement of the punch is measured using a Linear Variable Differential Transducer (LVDT) while the force is measured using a load cell, see Figure 11. The LVDT used is a Vishay Micro-Measurements Linear Displacement Sensor HS25 that uses a fully active 350-ohm strain gauge bridge to sense spindle displacement with infinite resolution. The rated full scale displacement range of the LVDT is 25 mm with a rated full scale output of 6.445 mV/V, a 2-10V excitation voltage and a 0.06% linearity error.

The force was measured using a 9.81 N (1000g) (0.127 mm and 0.254 mm thicknesses), 111.2 N (25 lb) (0.508 mm and 0.813 mm thicknesses) or 4448 N (1000 lb) (1.588 mm thickness) Sensotec precision miniature load cell model 31. These were full bridge, metal foil strain gauge load cells with an accuracy of 0.1% of the full scale reading and an excitation voltage 5 V for the smallest and 10 V for the two largest load cells. A total number of five tests were done for each thickness and heat treatment case and average plots and peak force values were obtained.

Heat Treatment. The aluminum specimens that were used for both the tensile and bending tests were heat treated to 325°C (Heat1), 450°C (Heat2),

550°C (Heat3), 575°C (Heat4) for 1 hour to re-crystallize the material and grow different sizes of grains. This was done to vary the number of grains through the thickness of the specimens. The resulting average grain sizes are given in Table 2. Cold worked 1100 Aluminum can be recrystallized by heating up to 410°C; therefore the heat treatment at 325°C is intended to anneal the material without necessarily recrystallizing the material. However, some grain growth is observed at this temperature, see Table 2. Annealing occurs in several stages starting with the recovery process which occurs at the lowest temperatures followed by recrystallization. No significant change in texture or preferred orientation occurs during the recovery process. Recrystallization leads to the gradual growth and appearance of a microscopically resolvable grain structure that is mostly residual stress free, whose orientation is usually different from that of the grains in the original deformed sheet.

"Complete annealing and recrystallization produce the properties of the original unstrained metal (O temper) except as they are changed by differences in grain size and preferred orientation. Heating at temperatures above the recrystallization temperature produces grain coarsening. The grain coarsening proceeds by the gradual elimination of small grains with unfavorable shapes or orientations relative to their immediate neighbors" [29]

The final size of grains achieved depends not only on the heat treatment temperature but also on the initial grain size and annealing texture. Starting off with small initial grains with a well developed annealing texture tends to promote

31

the growth of very large grains [26]. The heat treatment done at different temperatures produced varying grain sizes as shown in Table 2.

Measurement Check

Since this was the first time that the equipment was used in conjunction with the National Instruments (NI) 9237 data acquisition (DAQ) module and Labview software, it was necessary to check the system and assure that it was measuring accurately according to the calibration data provided by the manufacturer. The NI DAQ equipment measures strain which is converted to the appropriate parameter depending on which sensor is connected. The sensor manufacturer provides a calibration factor which is used to determine the output parameter versus strain (input) linear relationship for Labview data conversion. For the LVDT, a calibration factor of 6.445 mV/V was given. For a 10 V excitation, the output of the LVDT would be 64.45 mV at the full scale of 25 mm. From this calibration factor, the slope of the displacement (output parameter) versus strain (input) was determined assuming a gage factor (GF) of 2, which is typical for a metal foil type gage. The strain (ε) is given by

$$\varepsilon = \frac{\Delta V/V}{\text{GF}} \qquad (2)$$

Where $\Delta V/V$ is the calibration factor. Since the LVDT has a linear response for displacements up to 25 mm, the Slope (multiplier) is calculated from

32

$$\text{Slope} = \frac{\text{LVDT Range}}{\text{Strain}} \qquad (3)$$

This slope (7757.95 mm/strain) was used as the scaling factor to provide an accurate displacement output in mm in terms of strain. Experimental displacement measurements using precision gage blocks were performed to confirm the accuracy of the LabView displacement output, see Figure 12. The system was confirmed to measure to an uncertainty of less than 0.1% full scale, which was stated as the accuracy by the sensor manufacturer. Since the LVDT was measuring the displacement of only one jaw of the load stage, the slope was multiplied by a factor of two to provide the total displacement between the two LVDT jaws.

33
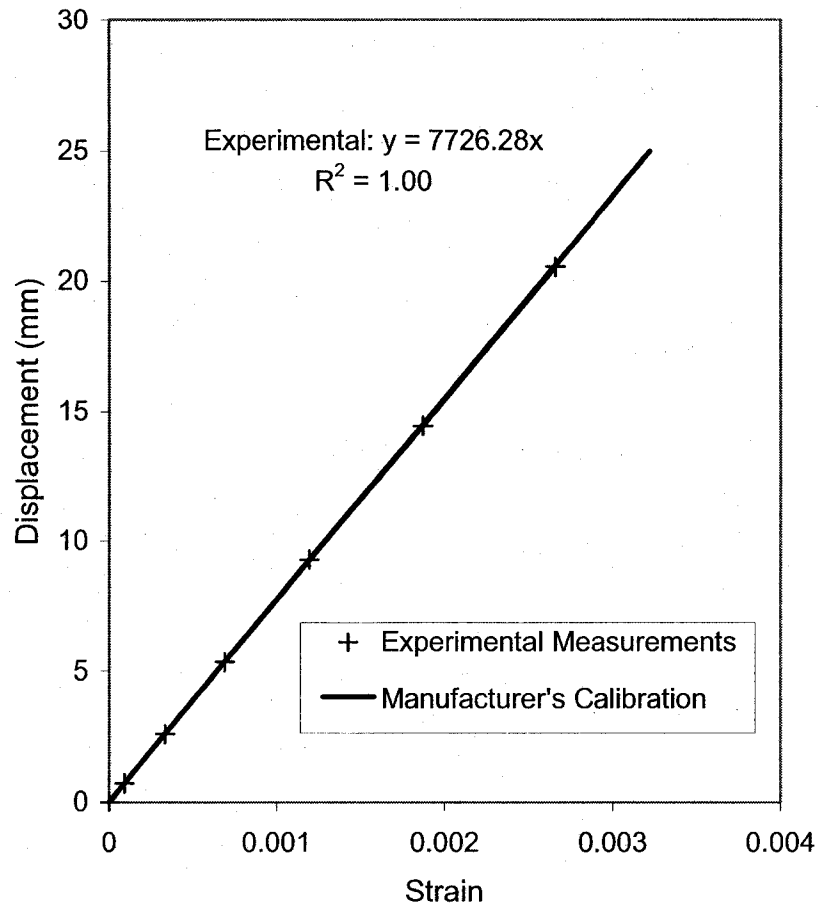
Figure 12 Curve for LVDT showing that the displacement is a linear function of the strain with a slope very close to that obtained using manufacturer's calibration data

The accuracy of the load cells, which are also metal foil type gages, was checked in a similar manner using certified weights traceable to the National Institute of Science and Technology (NIST) standards NIST 105-1 with class F tolerances. Using the calibration factor provided in the calibration certificate the relationship for force versus strain was determined. The slope for the 111.2 N (25 lb) load cell

34

(99320.15 N/strain) was determined from the manufacturer's calibration data and used as a scale multiplier in Labview. This scaling factor was then used to measure known weights to assure its accuracy. The manufacturer's calibration curve along with experimental data points for the 111.2 N (25 lb) load cell is shown in Figure 13. The 9.81 N (1000g) load cell was checked in a similar fashion.
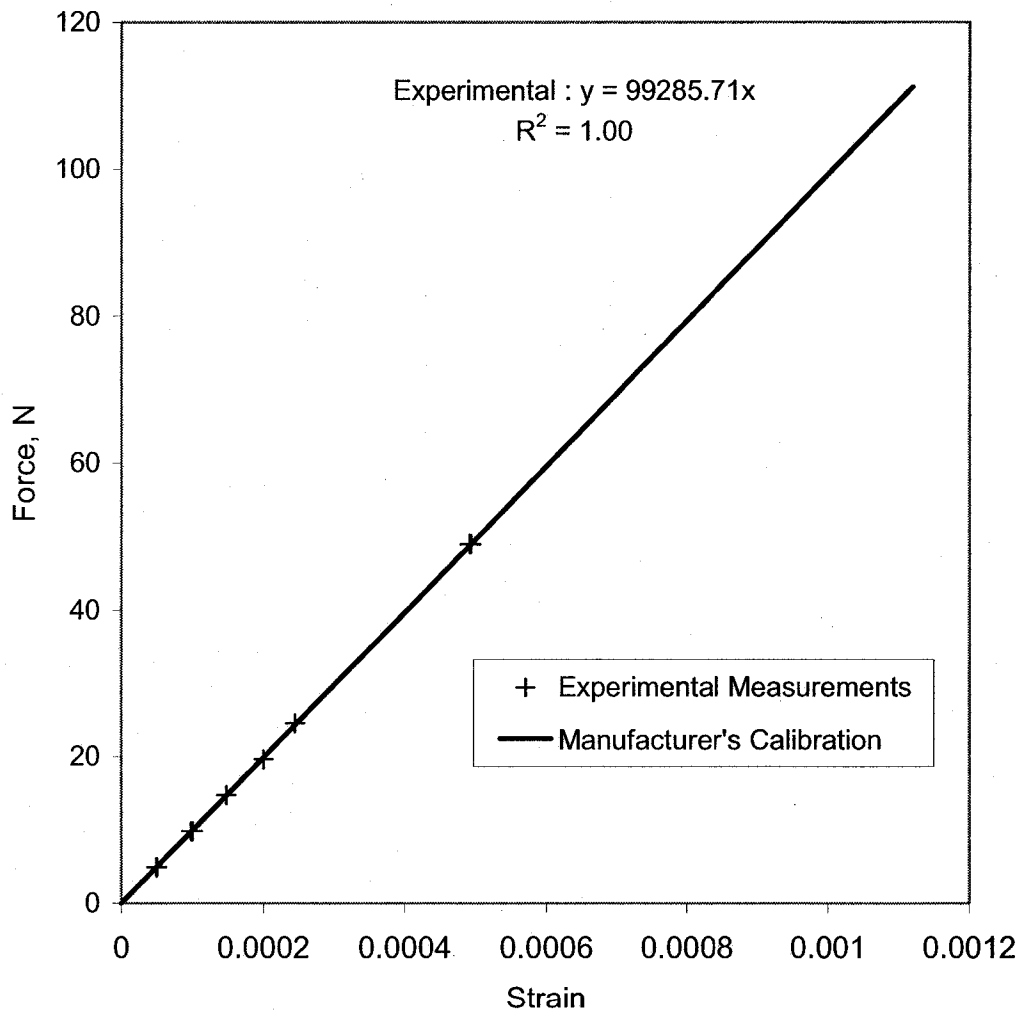
Figure 13 Calibration curve for the 111.2 N (25 lb) load cell showing that the force is a linear function of the strain with a slope very close to that obtained using the manufacturers calibration data

The data from the two transducers (LVDT and load cell) is read via the data acquisition module NI 9237 using LabView which outputs it to a file in a format appropriate for further analysis.

Bending Results

Once the experimental set up was in place and checked for measurement accuracy, bending experiments were conducted and the punch force versus punch depth data obtained is shown in Figure 14 to Figure 18. While the heat treatment did mitigate the effects of the materials deformation history clearly as can be seen from Figure 14 to Figure 18 it did not completely remove those effects.

36
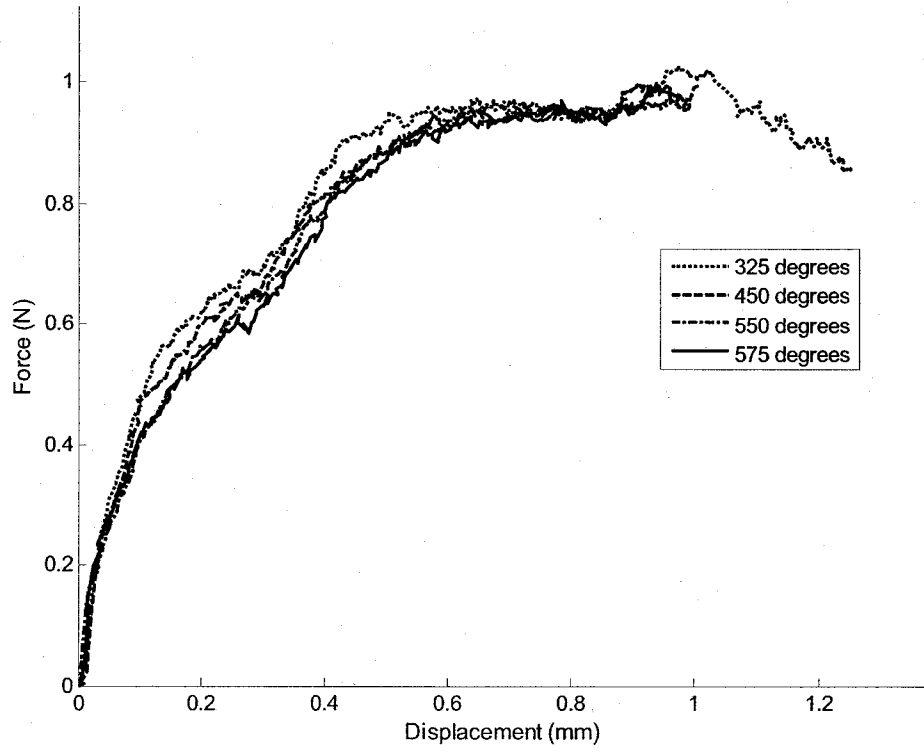
Figure 14 Variation of the bending force versus bending stroke curves with heat treatment temperature for 0.127 mm 1100 Al specimens

37
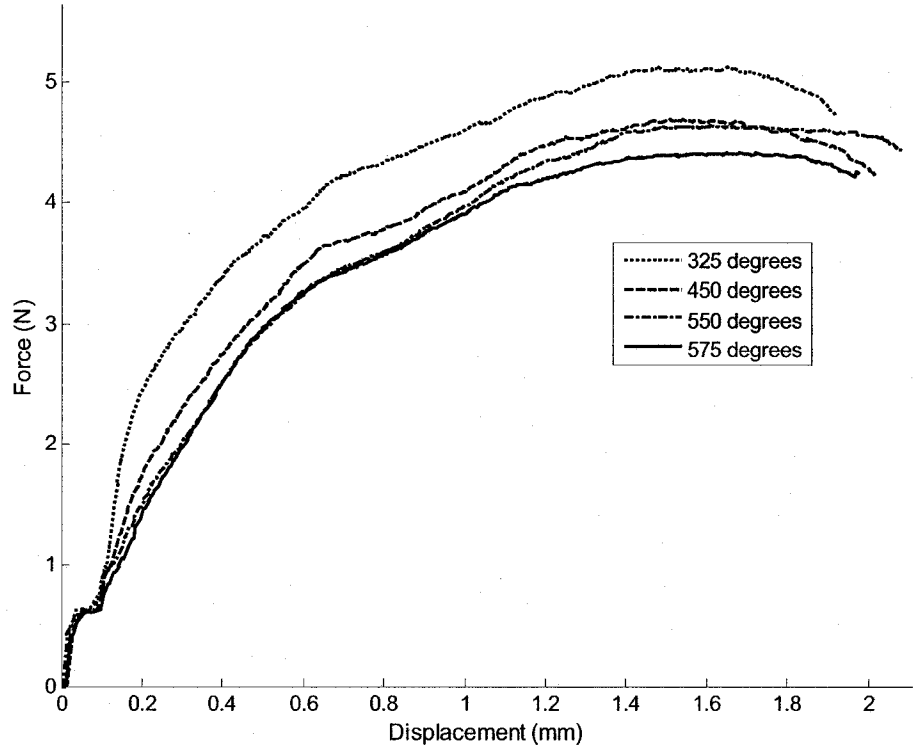
Figure 15 Variation of bending force versus bending stroke curves with heat treatment temperature for 0.254 mm 1100 Al specimens

38
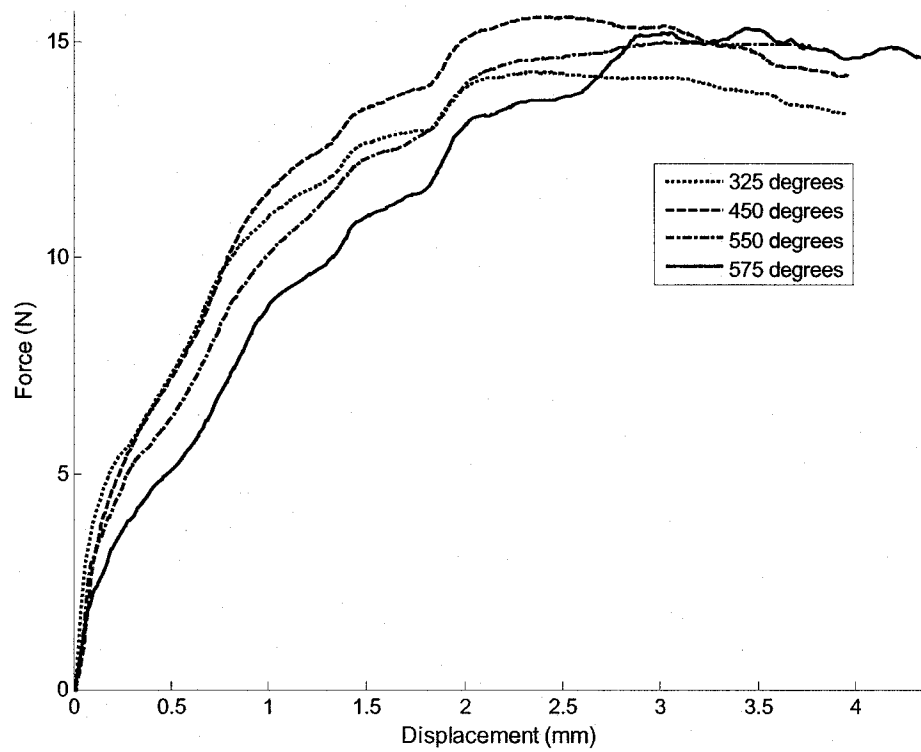
Figure 16 Variation of bending force versus bending stroke curves with heat treatment temperature for 0.508 mm 1100 Al specimens

39
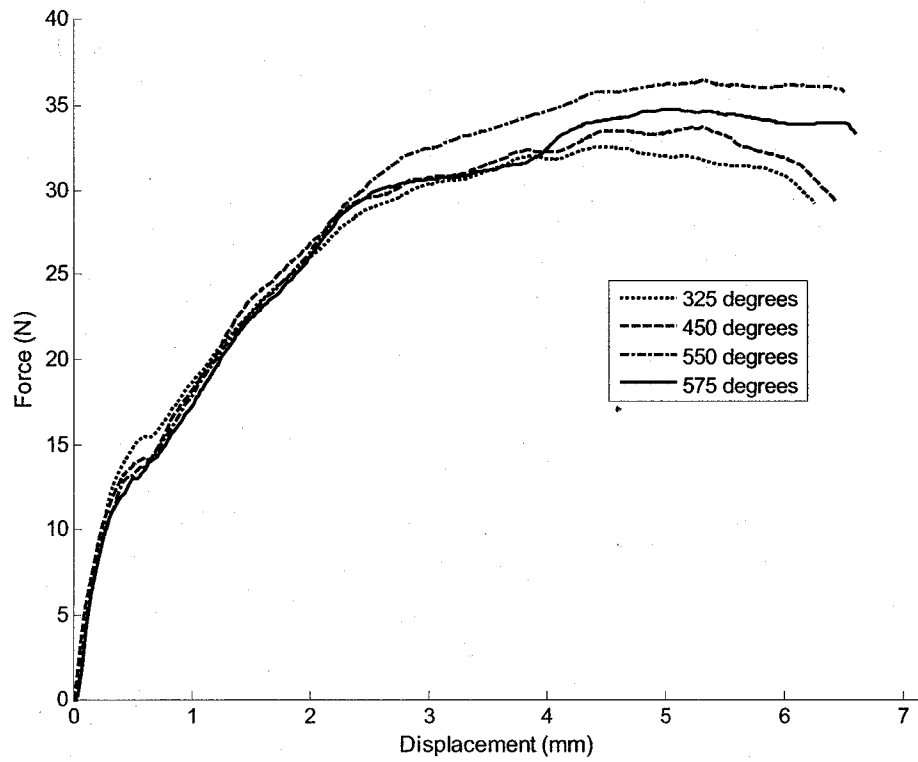
Figure 17 Variation of bending force versus bending stroke curves with heat treatment temperature for 0.813 mm 1100 Al specimens
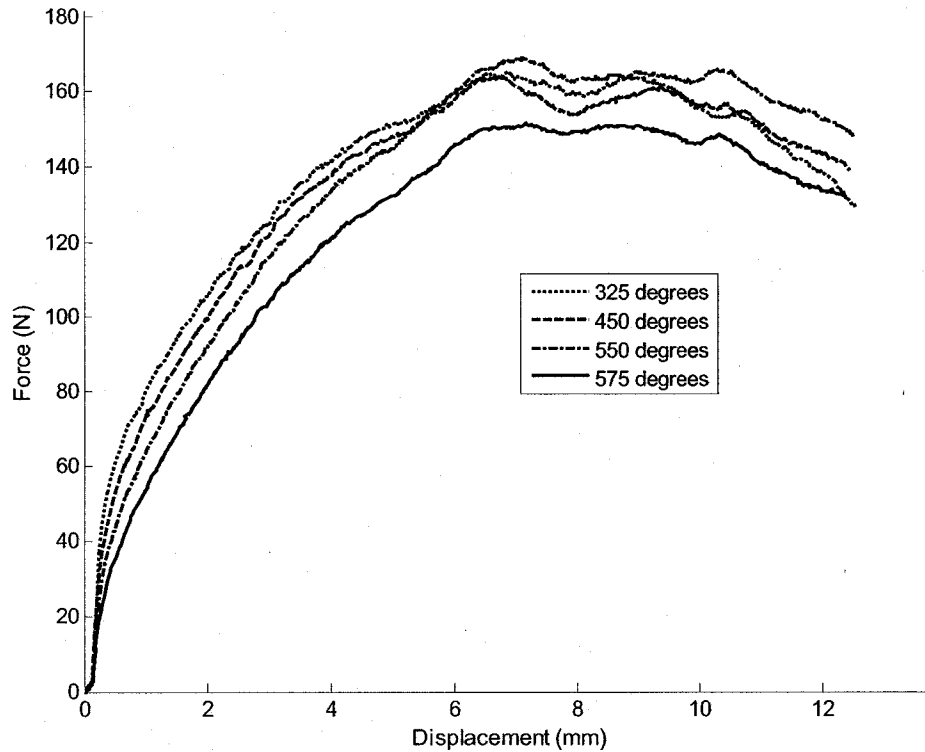
Figure 18 Variation of bending force versus bending stroke curves with heat treatment temperature for 1.588 mm 1100 Al specimens

All the samples are seen to have a pattern of reducing bending force with increasing heat treatment temperature (increasing grain size) before reaching the peak force. As the peak force is approached from the left of the curve any distinction or pattern that may have existed gets lost. The 0.254 mm and 1.588 mm cases show the clearest such pattern while for the others the pattern is less clear. For the 0.508 mm 325 °C heat treat case shows a lower bending force than that of the 450 °C case. This maybe due to the larger grain sizes observed for the 325 °C case (55μm) as compared to those for the 450 °C case (38μm), see Table 2 . The sample's deformation history becomes less significant as the

41

heat treatment temperatures are increased as can be seen from the normalized

force versus normalized displacement curves in Figure 19 to Figure 22. These

curves were plotted to factor out the effect of the sheet thickness.
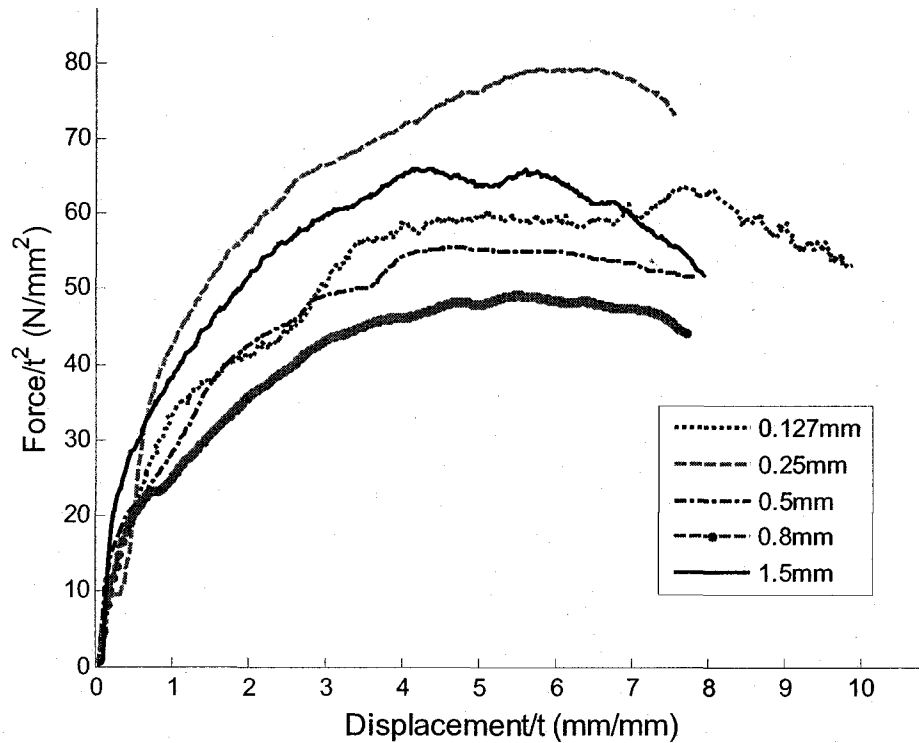
Figure 19 Normalized force versus normalized displacement curves for 1100 Al samples heat treated at 325 degrees
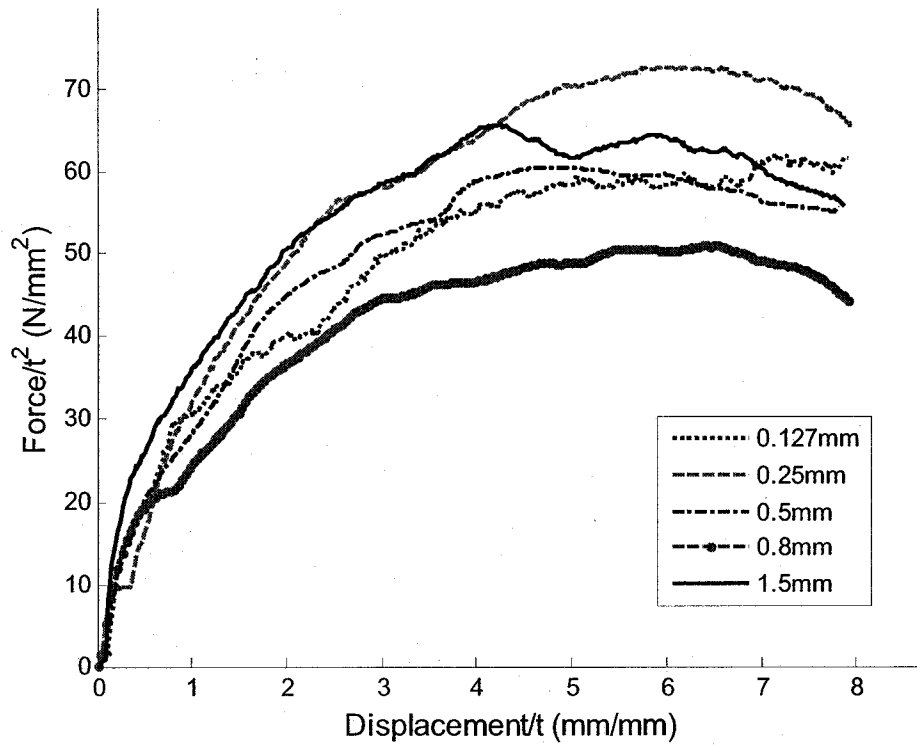
Figure 20 Normalized force versus normalized displacement curves for 1100 samples heat treated at 450 degrees

43
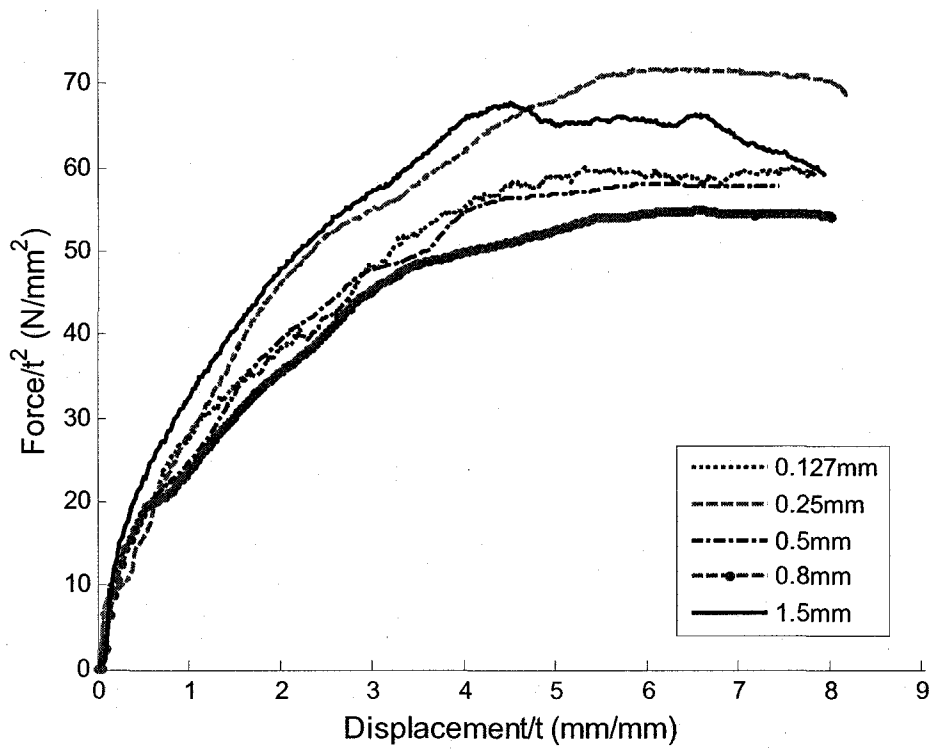
Figure 21 Normalized force versus normalized displacement curves for 1100 Al samples treated at 550 degrees
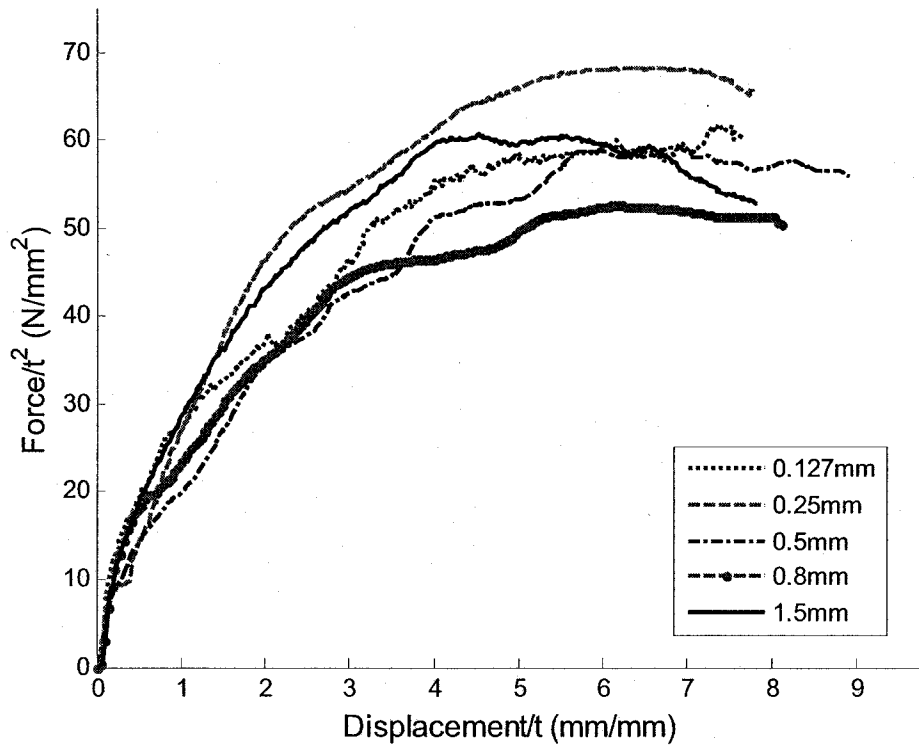
Figure 22 Normalized force versus normalized displacement curves for 1100 Al samples heat treated at 575 degrees

Peak Force (PF) Model

With experimental work completed, the focus shifts to the goal of investigating process model size effects in microbending. The first process model considered in this research simply predicts the peak bending force as opposed to a force versus displacement curve for the bending operation [19]. This model was developed from elementary bending theory of sheet material and gives the bending force as:

$$P = \frac{cwt^2\sigma_y}{L} \tag{4}$$

45

where P is the maximum punch bending force, w is the width of the sheet, t is the sheet thickness, L is the die opening clearance, σ_y is the yield strength of the material and c is a constant that varies from 0.3 for a wiping die, 0.7 for a U-die to approximately 1.3 for a V-die. This model excludes any friction and anisotropic effects and makes the following assumptions [30]:

1. Linear strain distribution through the sheet thickness and plane cross sections remain plane during the bending process

2. Transverse stresses are negligible

3. The neutral layer coincides with the mid-plane axis since the bend radius is much larger than the sheet thickness

4. The removal of bending moment after bending is equivalent to the elastic response by superposition of a moment with equal magnitude but opposite sign

5. Isotropic and elastic-perfect-plastic material

Curved Wall (CW) Model

The second process model considered, was developed by Wang et al. [24], and provides a curve of the force versus the depth of punch. Their model was shown to be reliable for macroscale bending operations using 2024-O Aluminum sheets. This model assumes

1. A logarithmic true strain distribution (for plastic bending) through the sheet thickness as shown in Figure 23 where:

46

$$\varepsilon_x = \ln\left(1 + \frac{z}{R_n}\right) \tag{5}$$

2. Plane strain deformation – neglects transverse stresses

3. Strain hardening

4. Hills non-quadratic yield theory for normal anisotropic sheet

   materials

According to Hill [31], the error in the elementary bending theory is a function of the ratio of radius of curvature (R) to sheet thickness (t) whereby for ratios of $R/t > 4$, the effects of the transverse stresses can be ignored without significant loss of accuracy. For ratios of $R/t < 4$, the transverse (normal) stresses viz. shear and radial stresses, can no longer be neglected as they can be of the same magnitude as the axial stresses. These transverse stresses cause the neutral axis to shift and increase the thinning of the sheet.

This model divides the sheet profile into three deformation sections: elastic bending region (**CE**), an elasto-plastic bending region (**BC**) and a fully plastic bending region (**AB**) as shown in Figure 24. (It should be noted that the experimental set-up in Wang et al. [24] is actually 3-point bending, which is equivalent to flanging when half of the geometry is considered. See Figure 5.

47
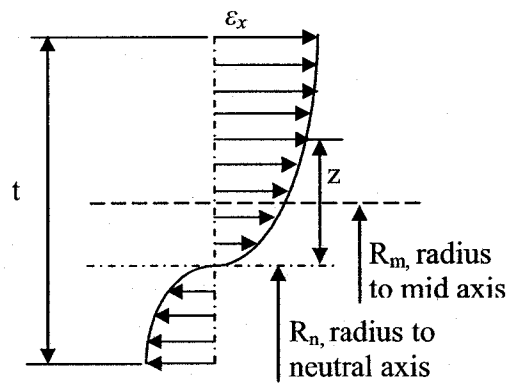
Figure 23 Logarithmic strain distribution through the sheet thickness [24]
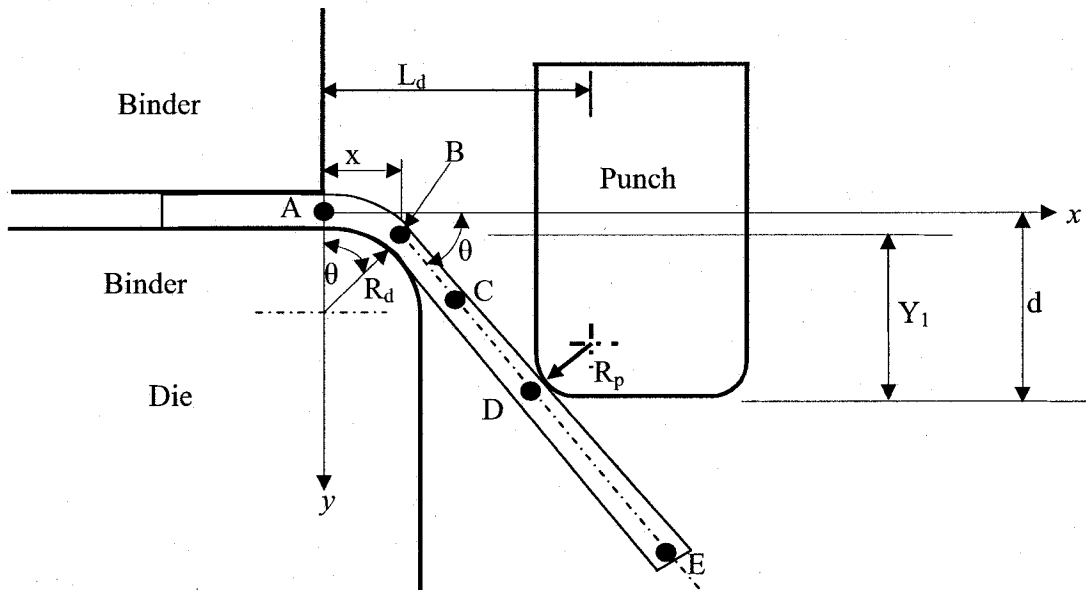
Figure 24 Schematic for the bending models

48

The length **BD** represents the bent arc length S_1 of the sheet, while θ represents the bend angle. The equations from Wang et al. [24] are presented again here for clarification and comparison to the new process models developed. The internal bending moment in the different regions is given as follows.

For the fully elastic bending region:

$$M_E = \frac{wt^2}{6} \frac{\sigma_y}{1-v^2} \tag{6}$$

where w is the width, t is the thickness, σ_y is the elastic yield stress and v is the Poisson's ratio.

For the elasto-plastic bending region:

$$M_{ep} \approx C_3 R^2 + \frac{C_2}{R^n} + \frac{C_1}{R^{n+1}} \tag{7}$$

where

$$C_1 = \frac{3t}{4} \frac{n+2}{n+3} C_2, \qquad C_2 = \frac{2wKF^{n+1}}{n+2} \left(\frac{t}{2}\right)^{n+2}, \qquad C_3 = \frac{2}{3} \left(\frac{\sigma_0\left(1-v^2\right)}{E}\right)^2 \sigma_0 w$$

In addition, σ_0 is the initial yield stress, E is the Young's modulus, K is the strength coefficient, n is the work hardening exponent and F is the anisotropic index of the material.

Finally for the fully plastic bending region:

$$M_A = \frac{KF^{n+1}}{2(2+n)} wt^2 \left(\frac{t}{2R_p'}\right)^n \left(1+\frac{3n+2}{2n+3}\frac{t}{2R_p'}\right) \tag{8}$$

where $R_p' = R_p + \frac{t}{2}$, R_p is the radius of the punch, and t is the sheet thickness [24].

49

It should be noted that Wang et al. [24] assumed a linear distribution of moment, with the maximum bending moment being experienced at the die tip for their bending model. The maximum external moment is given as the sum of the moments due to bending and friction around the die shoulders:

$$M = PL_d \left(1 - \frac{R_d}{L_d} \sin\theta \right) + PL_d \frac{\tan\theta - \mu}{1 + \mu\tan\theta} \left(\frac{d}{L_d} - \frac{R_d}{L_d}(1 - \cos\theta) \right) \tag{9}$$

where μ is the friction coefficient between the die and the sheet.

From Eq. (9) the punch force, P, for a flanging operation (taken as one half of the punch force for a 3-point bending operation), which is a function of the depth of the punch stroke, is found to be:

$$P = \frac{M}{L_d \left[\left(1 - \frac{R_d}{L_d} \sin\theta \right) + \frac{\tan\theta - \mu}{1 + \mu\tan\theta} \left(\frac{d}{L_d} - \frac{R_d}{L_d}(1 - \cos\theta) \right) \right]} \tag{10}$$

The internal bending moment, M_A, from Eq. (8) and the external bending moment, M from Eq. (9), are equal. Thus Eq. (9) is substituted into Eq. (10) to solve for the bending force, P, as a function of the blank properties, tool parameters, and other process parameters such as friction coefficient, μ, punch displacement, d, and the bending angle, θ, such that:

$$P = \frac{\dfrac{KF^{n+1}}{2+n} wt^2 \left(\dfrac{t}{2R_p'} \right)^n \left(1 + \dfrac{3n+2}{2n+3} \dfrac{t}{2R_p'} \right)}{2L_d \left[\left(1 - \dfrac{R_d}{L_d} \sin\theta \right) + \dfrac{\tan\theta - \mu}{1 + \mu\tan\theta} \left(\dfrac{d}{L_d} - \dfrac{R_d}{L_d}(1 - \cos\theta) \right) \right]} \tag{11}$$

The punch displacement, which is assumed to be a non-linear function of the bend angle, is obtained as the sum of the vertical component of the bent arc

50

length S_1 and the corresponding components of the punch and the die. The vertical component, Y_1, see Figure 24, of the bent arc length S_1 is:

$$Y_1 = \int_0^{S_1} dy = \int_0^{S_1} \sin \theta \, dS \tag{12}$$

The punch displacement corresponding to θ under load is:

$$d = Y_1 + \left(R_d + \frac{t}{2}\right)(1 - \cos\theta) + \left(R_p + \frac{t}{2}\right)(1 - \cos\theta_c) \tag{13}$$

$$d = \int_0^{S_1} \sin\theta dS + \left[R_d - (R_d + t/2)\cos\theta\right] + \left[R_p - (R_p + t/2)\cos\theta_c\right] + t \tag{14}$$

where the bent arc length is:

$$S_1 = \int_{\theta_c}^{\theta} \frac{dX}{\cos\theta} \qquad 0 \le X \le X(\theta) \tag{15}$$

and

$$X(\theta) = L_d - \left(R_p + t/2\right)\sin\theta_c - \left(R_d + t/2\right)\sin\theta \tag{16}$$

This model was shown to predict experimental results well for 2024-O Aluminum test samples with a thickness of 1.27 mm, subjected to 3-point bending [24], see Figure 25. The bent arc length given by Eq. (15) provides more accurate estimates of the punch stroke than either a straight line approximation of the sheet between the die and the punch contact regions or a circular arc approximation. According to Wang et al. [24], the straight line approximation underestimates the arc length and overestimates the punch stroke while the circular arc approximation overestimates the bent arc length and underestimates the punch displacement. A straight line approximation would therefore underestimate the punch force. It should be noted that this model requires a

51

punch radius. The tooling for the experiments by LFT [25] did not have a specified radius but a broken edge to eliminate any burrs. Therefore, a punch radius of 0.25 mm was assumed in the analysis of that specific data set.
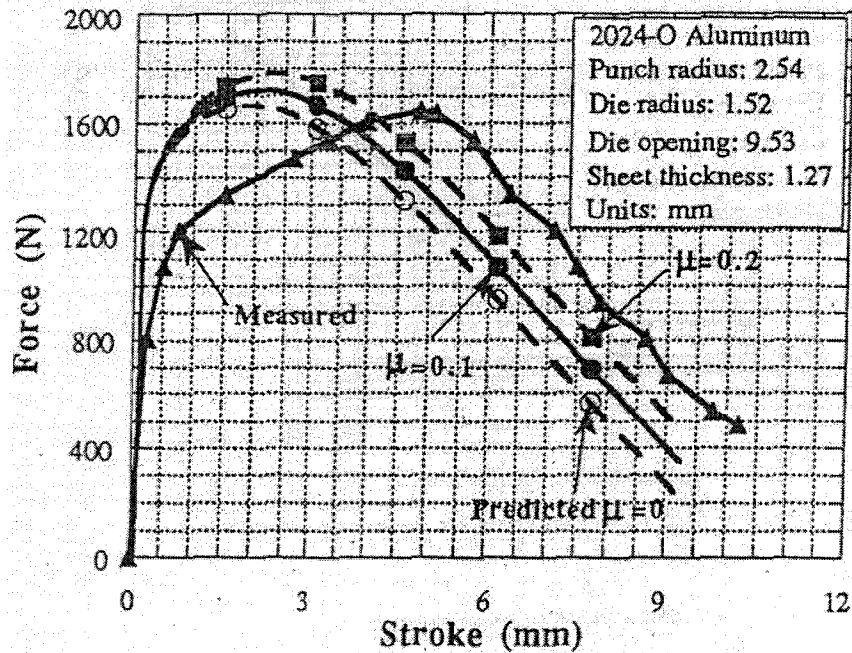
Figure 25 Comparison of predicted and experimental punch force versus punch displacement for a 3-point bending process for 2024-O Aluminum sheets [24]

Straight Wall Approximation (SW) Model

For microscale specimens with less than approximately fifteen grains through the thickness, it may be more reasonable to assume that the sheet will be approximately linear between the die and punch contact points (see segment **BD** on Figure 24). This model takes the bending force equation as developed by Wang et al. [24] and assumes a straight wall from the point of contact with the die to the end of the sheet (**BE**) as shown in Figure 24. The justification for using the

52

linear approximation is that the span length of the sheet is too short for any significant curvature to be experienced.

Assuming section **BD** is straight, the depth of stroke is then found to be a function of the bend angle as follows. From trigonometry:

$$y = R_d - \sqrt{R_d^2 - x^2} \tag{17}$$

and

$$\tan \theta = \frac{x}{R_d - y} = \frac{d - y}{L_d - x} \tag{18}$$

This gives the depth of stroke as a function of only x as:

$$d = \frac{x(L_d - x)}{\sqrt{R_d^2 - x^2}} + R_d - \sqrt{R_d^2 - x^2} \tag{19}$$

Reorganizing Eq.(19) results in a quadratic expression of the unknown value x:

$$\alpha x^2 - \beta x + \delta = 0 \tag{20}$$

where

$$\alpha = L_d^2 + d^2 - 2dR_d + R_d^2 \qquad \beta = -2L_d R_d^2 \qquad \delta = 2dR_d^3 - R_d^2 d^2 \tag{21}$$

From this equation, x and thus also y are solved for based on a given depth of stroke and the angle θ is solved for from Eq. (18). These values of **θ** and **d** are substituted into Eq. (11) to solve for the force using this model.

Curved Wall Modified Moment (CWMM) Model

As sheet thickness decreases and thus also the number of grains through the thickness decreases, it may be more reasonable that a linear strain

53

distribution through the thickness of the sheet exists as opposed to the logarithmic distribution shown in Figure 23 since the strain distribution in individual grains can not exhibit a significant non-linearity. A linear strain distribution through the sheet thickness can be shown from strain data given for 0.5 mm thick α brass (CuZn15) specimens for both fine and coarse grains [20].Therefore, a modified moment equation based on a linear strain distribution was used. From bending theory [26, 30], the elasto-plastic bending moment experienced in a symmetrical (pure) bending operation is:

$$M = \int_A \sigma_x z dA \qquad (22)$$

Since these models assume a linear true strain distribution across the sheet thickness as shown in Figure 26, the strain is:

$$\varepsilon_x = \frac{z}{R_m} = \kappa z \qquad (23)$$

where κ is the curvature and R_m is the radius to the mid axis and z is the distance from the mid axis in the thickness direction. Such a linear strain distribution has been used extensively in past research efforts as well [16, 30-34].
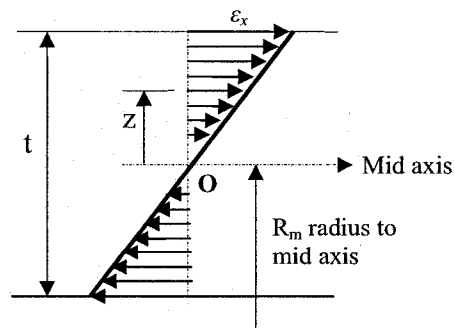
Figure 26 Linear distribution of strain across the sheet thickness

54

For plane strain conditions, a strain hardening material and assuming Von Mises yield criterion, $\sigma_x = \left(\dfrac{2}{\sqrt{3}}\right)\bar{\sigma}$ and $\bar{\sigma} = K\bar{\varepsilon}^n$, $\bar{\varepsilon} = \left(\dfrac{2}{\sqrt{3}}\right)\varepsilon_x$, it follows that:

$$M = 2\left(\frac{2}{\sqrt{3}}\right)^{n+1} Kw\kappa^n \int_0^{t/2} z^{n+1} dz \tag{24}$$

Where K is the strength coefficient, n is the strain hardening exponent, and κ is the curvature of the sheet. The bending moment is:

$$M = \frac{2wK\kappa^n}{n+2}\left(\frac{2}{\sqrt{3}}\right)^{n+1}\left(\frac{t}{2}\right)^{n+2} \tag{25}$$

This moment expression is substituted into Eq. (10) resulting in a modified bending force equation. In order to solve for the moment of Eq. (25), and thus for the punch force, the curvature κ is required. Thus, κ terms for both the curved wall model and the straight wall model were determined.

The curvature for the CWMM Model is obtained from the following expressions as given by Wang et al. [24], for the plastic region:

$$\kappa_p = \frac{1}{R_d} \tag{26}$$

For the elasto-plastic region:

$$S = S_1 - \frac{C_6}{\kappa_{ep}^2} - C_7\kappa_{ep}^n - C_8\kappa_{ep}^{n+1} \qquad 0 \leq S \leq S_E \tag{27}$$

This is solved numerically to provide curvature values for every arc length S within the elasto-plastic region. These values are then averaged to obtain the mean curvature κ_{ep} for this region. The curvature for the elastic region is:

$$\kappa_e = C_5\left(S_1 - S\right) \qquad S_E \leq S \leq S_1 \tag{28}$$

55

where the constants are:

$$C_5 = \frac{C_4 M_E}{E'I}, \qquad C_4 = \frac{M_E}{M_A S_1} \qquad C_6 = \frac{S_1}{M_A} C_3, \qquad C_7 = \frac{S_1}{M_A} C_2$$

$$C_8 = \frac{3t}{4} \frac{n+2}{n+3} C_7$$

(29)

The total effective strain experienced in the beam, at every punch displacement depth, is the sum of the effective strains in the different regions, thus:

$$\overline{\varepsilon}_T = \overline{\varepsilon}_p + \overline{\varepsilon}_{ep} + \overline{\varepsilon}_e$$

(30)

Assuming a linear distribution of strain through the sheet thickness as shown earlier, a plane strain situation and von Mises yield criterion,

$\overline{\varepsilon}_p = \frac{2}{\sqrt{3}} \kappa_p z$, $\overline{\varepsilon}_{ep} = \frac{2}{\sqrt{3}} \kappa_{ep} z$ and $\overline{\varepsilon}_e = \frac{2}{\sqrt{3}} \kappa_e z$ which gives the total effective strain:

$$\overline{\varepsilon}_T = \frac{2}{\sqrt{3}} \left(\kappa_p + \kappa_{ep} + \kappa_e \right) z = \frac{2}{\sqrt{3}} \kappa_T z$$

(31)

Therefore the total curvature is:

$$\kappa_T = \kappa_p + \kappa_{ep} + \kappa_e$$

(32)

This modified moment model was then used with the non-linear approximation for the wall section **BC** in Figure 24 (Curved Wall Modified Moment Model (**CWMM Model**)), which affects the depth of stroke *d* with bend angle *θ* relationship.

Straight Wall Modified Moment (SWMM) Model

Development of this model assumed a straight wall profile, as shown earlier for the **SW** model and a linear strain distribution through the sheet

56

thickness as shown for the **CWMM** model. The bending force for this model then is given as Eq. (10) with the bending moment determined using Eq. (25). and Eq. (19) respectively.

While this model includes a straight formed wall assumption, the entire sheet has an overall curvature because of the curved section, which is the plastically deformed portion of the sheet in contact with the die radius. The sheet profile is estimated as a quadratic function from which the curvature is determined from Eq.(33):

$$\kappa = \frac{d^2 y/dx^2}{\left[1 + \left(dy/dx\right)^2\right]^{3/2}} \tag{33}$$

Comparison of Experimental and Predicted Results

Using experimental data for 2024-O aluminum alloy obtained from a macroscale 3-point bending process with a sheet thickness of 1.27 mm, a die opening of 9.53 mm, die radius of 1.52 mm and a punch radius of 2.54 mm [24], predictions of the peak bending force for each of the models were obtained. Figure 27 is a plot showing peak forces as predicted by the different models compared to experimental investigations [24]. The material was assumed to be isotropic and in plane strain with the following properties: Young's modulus 73.08 GPa, Poissons ratio of 0.3, Yield stress of 90 MPa, strength coefficient, K, of 266 MPa and a strain hardening exponent, n, of 0.134.

57
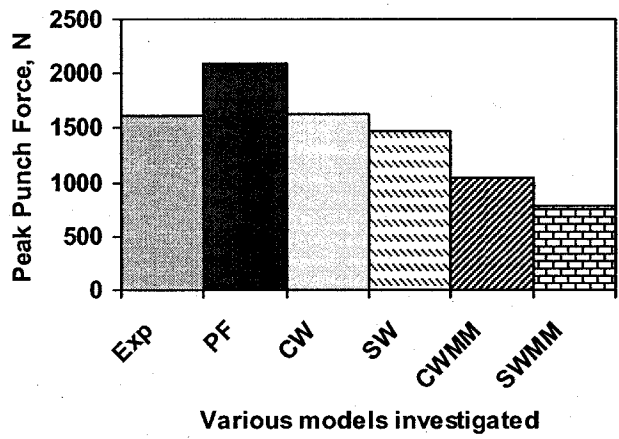
Figure 27 Comparison of peak bending force for different models with experimental data from Wang et al. [24]

As indicated earlier, the second set of experimental force data was obtained from LFT [25] using brass, CuZn15.

The third set of data was from experiments conducted by the author using 1100 Aluminum as outlined in the experimental investigations section earlier.

The different models were compared at each thickness and heat treatment condition. Note that since size effects exist with respect to material properties, the material properties used in the models varied for each heat treatment and thickness case based on the information provided in Table 2 and Table **3**. However, the friction coefficient, which was set at 0.2, was not varied since friction is not a dominant effect in bending. Figure 28 shows the plots of the peak bending punch force versus the punch displacement for the five models for brass (CuZn15). Figure 29 shows typical curves of punch force versus punch displacement obtained for different models compared with the experimental curve for 0.1 mm thickness CuZn15 specimens with no heat treatment.

58

(a)

(b)

(c)
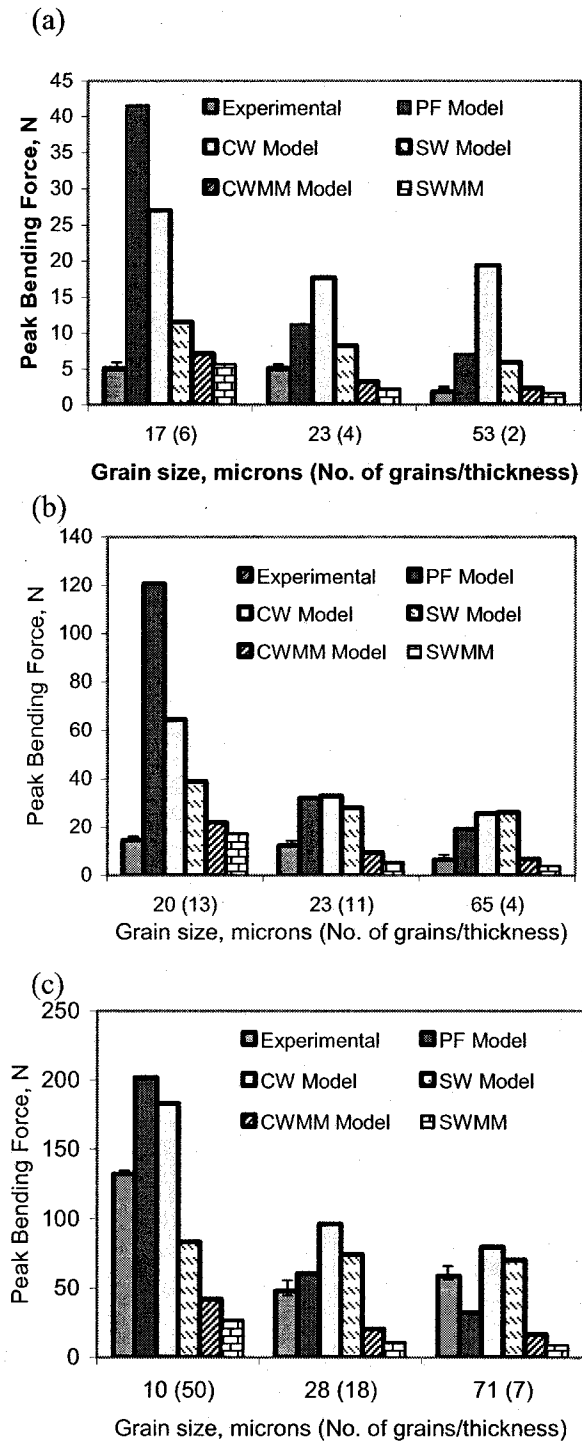
Figure 28 Comparison of the peak bending force for the (a) 0.1 mm, (b) 0.25 mm, and (c) 0.5 mm thickness cases for the various models and experimental data [25] for CuZn15.
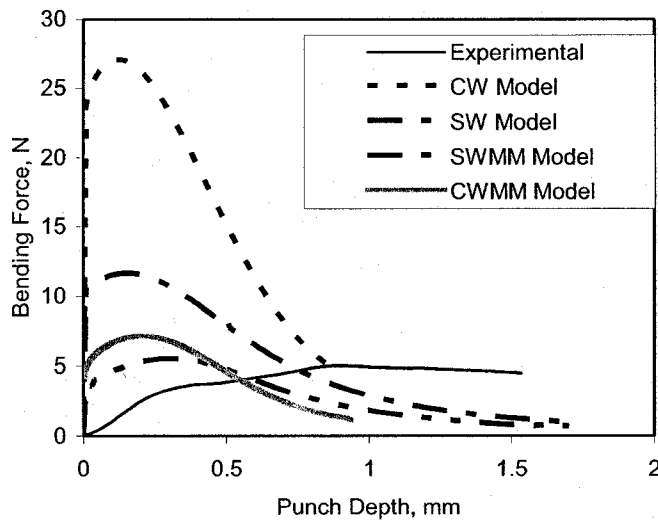
Figure 29 shows characteristic curves of the bending force versus punch displacement for the different models and experimental data for 0.1 mm thickness, non-heat treated case for CuZn15.

Discussion – Brass

For the data from Wang et al. [24] with a sheet thickness of 1.27 mm, the Curved Wall, **CW**, model which assumes a logarithmic strain distribution through the sheet thickness and curved sheet profile, provides the most accurate prediction of the peak bending force followed by the Straight Wall, **SW**, model that assumes a logarithmic strain distribution through the sheet thickness and a straight wall profile. The Peak Force, **PF**, model over predicted the peak bending force for this case. These three are considered macrocsale models and predicted the peak bending force accurately, see Figure 27. The other two models i.e. Curved Wall Modified Moment, **CWMM**, and Straight Wall Modified Moment, **SWMM**, both assumed a linear strain distribution through the sheet thickness and both significantly under predicted the peak force for the macroscale specimen.

60

For the microscale data from LFT where there are less than about 15 grains through the thickness, i.e. 0.1 mm and 0.25 mm cases, the **CWMM** and **SWMM** models, provided a better estimate for the peak bending force. Since there are fewer grains through the thickness and the strain distribution in a given grain cannot contain significant non-linearities, a linear strain distribution is more physically reasonable for these microscale cases. The macroscale models, **CW** and **SW** models, over predicted the peak bending force. An exception to this is the 0.5 mm Heat Treat 2 case where there are only seven grains through the thickness and the experimental results are between the predicted values for the macroscale and microscale models but are closer to the macroscale ones. The lack of agreement for this case may be due to specimen size effects.

For the LFT data where the sheet contains more than about 15 grains through the thickness but still a relatively modest number compared to the number of grains that would be present through the thickness in a macroscale specimen, i.e. 0.5 mm Non-heat Treat (50 grains through the thickness) and Heat Treat 1 (18 grains through the thickness) cases, the experimental results are between the predicted values from the macroscale and microscale models. Due to the relatively small number of grains through the thickness, these cases can be considered mesoscale. Therefore, a model that assumes a "slightly" non-linear strain distribution across the thickness may in fact be more accurate for these mesoscale cases.

A plot of the punch force versus punch displacement is given in Figure 29 for the 0.1 mm, Non-heat treat case. For this particular case, the **SWMM**

61

provided the most accurate results. However, for the six microscale cases (i.e. the 0.1 and 0.25 mm cases), three were better predicted by the **SWMM** model and three by the **CWMM** model. The cause of this inconsistency is possibly due to the random orientation of the grains in the individual specimens at the microscale. Thus, one of these models can not be claimed to be unequivocally better than the other. Also, as Figure 29 shows, all of the models predict an early location of the peak bending force compared to the experimental data and the shape of the curves are not exact. These are consistent with the results from Wang et al. [24] for the macroscale case. Finally, it is apparent that assuming a linear strain distribution through the thickness has a more significant effect on the accuracy of the predicted process forces than assuming a straight sheet wall profile for microscale bending cases as shown in Figure 28.

For the **PF** model, the results are highly dependent on the yield value of the material. For the non-heat treated cases, the **PF** model significantly over predicted the peak bending force as the yield stress value for the non-Heat Treated material was high due to strain hardening during the rolling process. For the annealed cases of brass (Heat Treat. 1 and 2), the accuracy of the peak force model improved but still generally over predicted the peak bending force.

Assuming a linear strain distribution seems to have a greater effect in improving the prediction of the peak force for microscale cases than assuming a straight sheet wall profile. However for comparison and clarity of the results presented above for brass a summary is shown in Figure 30 through Figure 32 in which the experimental peak forces are compared only to one macroscale (**CW**)

62

Model and one microscale (**SWMM**) model. The macroscale model over predicts the peak force and is more accurate for the macroscale cases such as the 0.5 mm non-heat treat case with 50 grains through the sheet thickness. For mesoscale cases such as the 0.5 mm thickness heat treat I the macroscale and microscale models over and under predicted respectively.
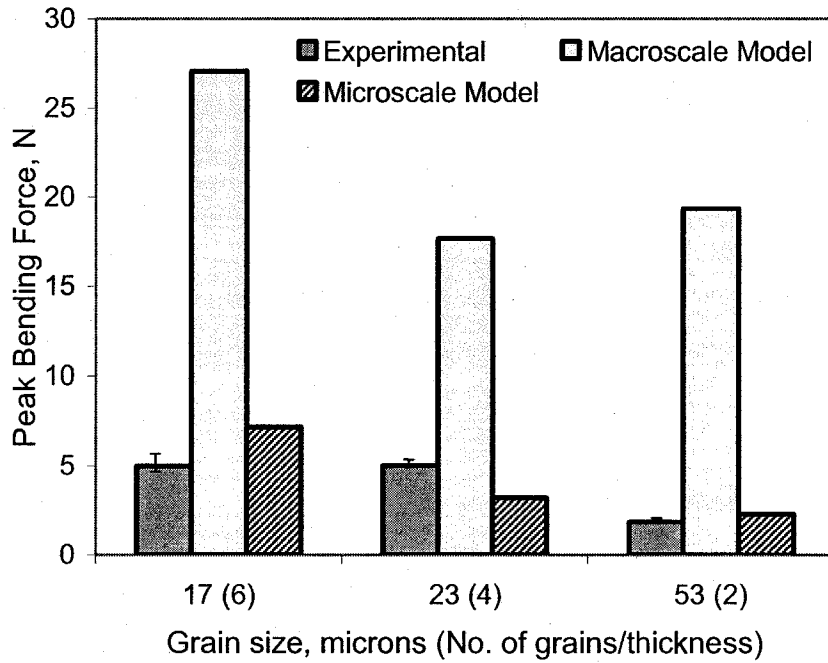
Figure 30 Comparison of the experimental peak bending force [25] for the 0.1 mm thickness cases with the macroscale, microscale models for CuZn15.
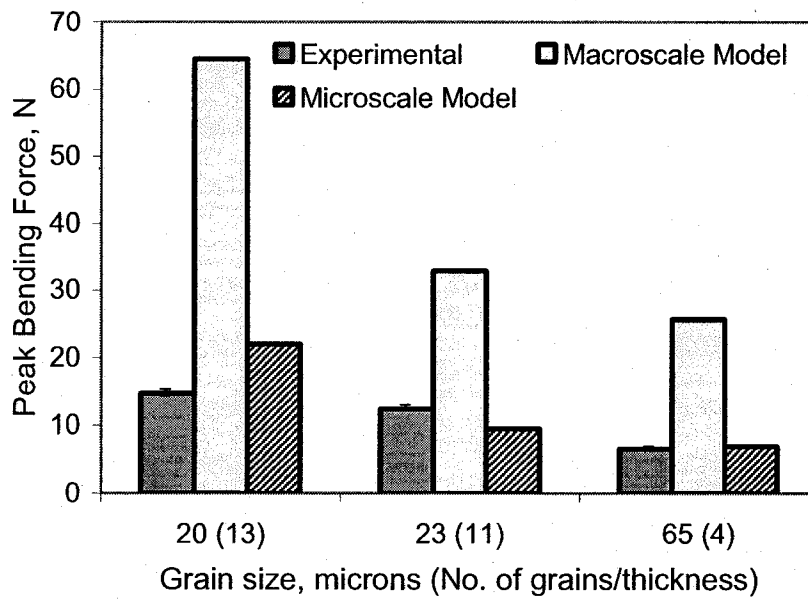
Figure 31 Comparison of the experimental peak bending force [25] for the 0.25 mm thickness cases with the macroscale, microscale models for CuZn15.
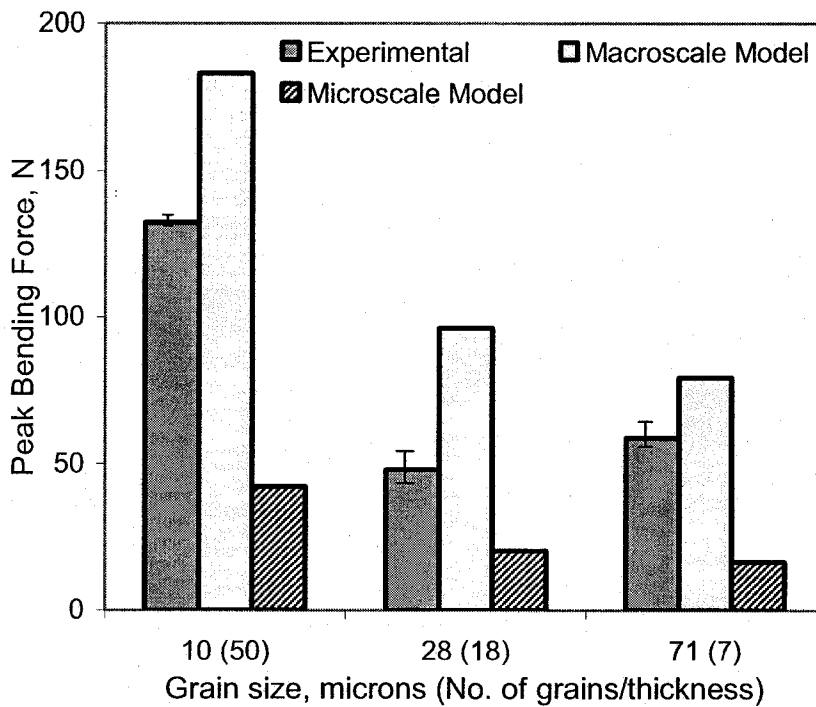
Figure 32 Comparison of the experimental peak bending force [25] for the 0.5 mm thickness cases with the macroscale, microscale models for CuZn15.

Similarly only two models are used in presenting the 1100 Aluminum results viz. the results of only one macro and one microscale model will be compared to the experimental results. As with the brass, the **CW** model will be used as the macroscale model while the **SWMM** will be used as the microscale model from this point forward.

The experimental peak force data for aluminum for each of the different sizes and heat treatment cases were compared with predictions from the macroscale and microscale models and the results are shown in Figure 33 to Figure 37. The as received specimen results are excluded from this analysis because of the uncertainty of their deformation history and inability in some cases to determine the average grain sizes and therefore cannot fully characterize the material.

65
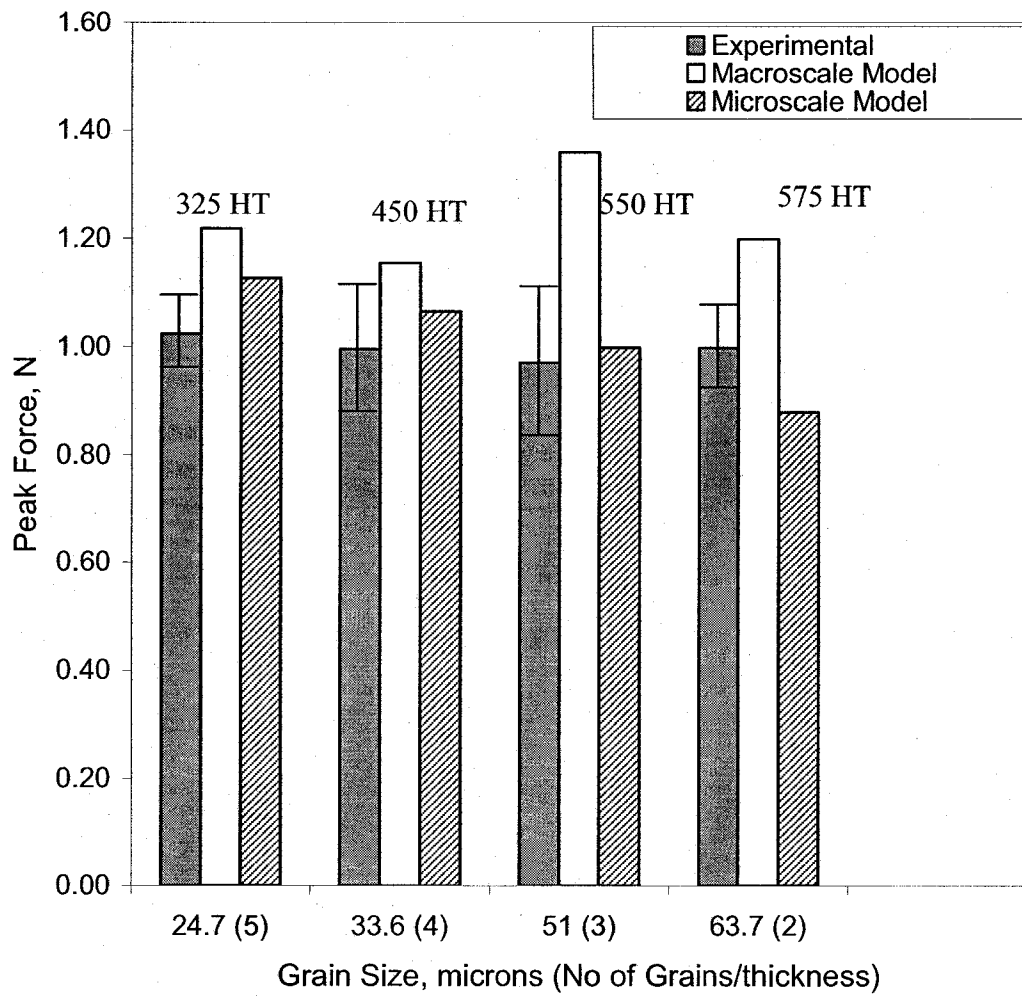
Figure 33 Comparison of predicted peak forces to experimental peak forces for 0.127 mm thickness 1100 Al specimens
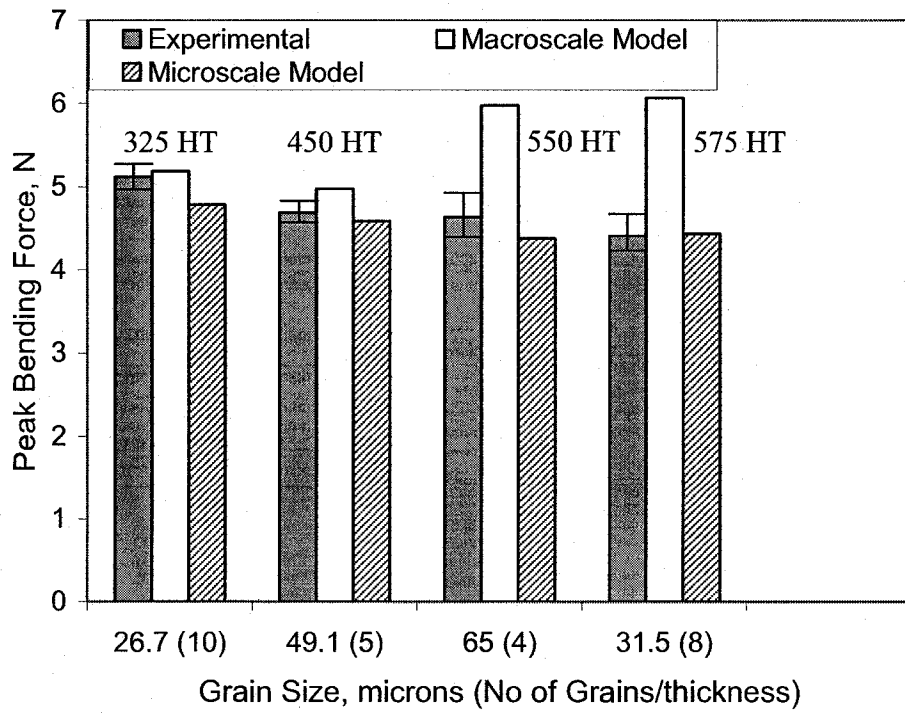
Figure 34 Comparison of predicted to experimental peak forces for the 0.254 mm thickness 1100 Al specimens
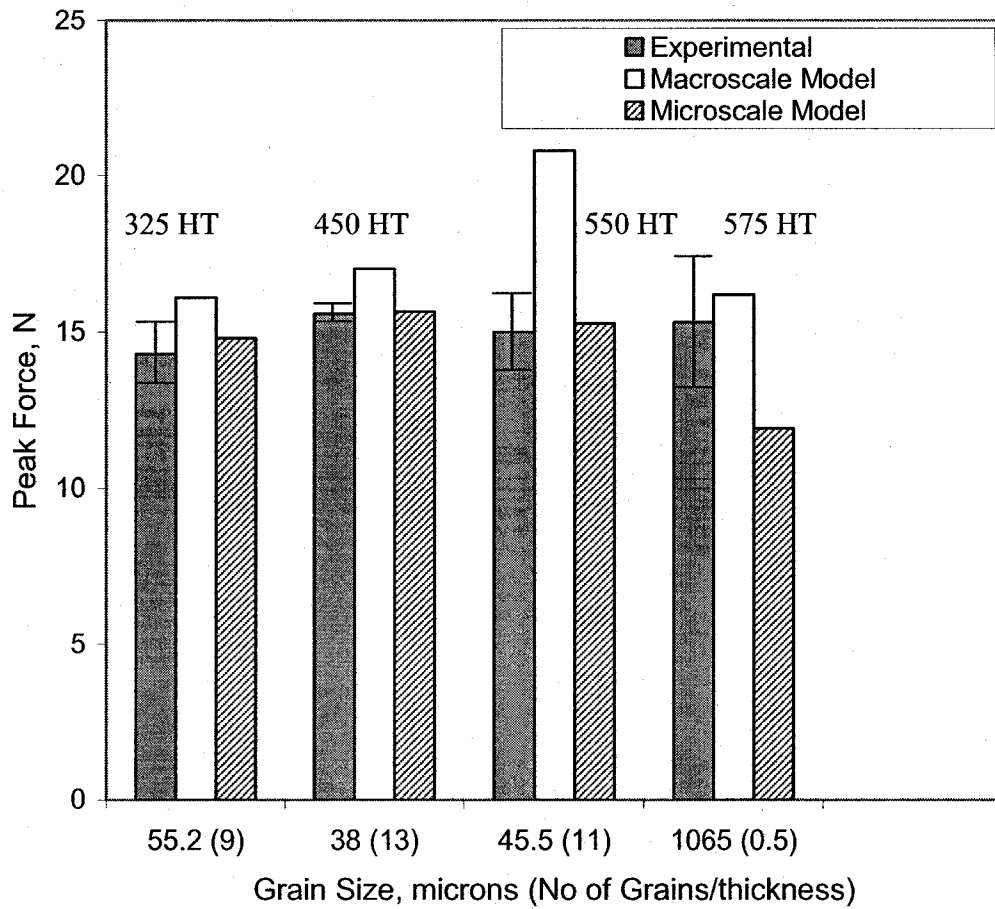
Figure 35 Comparison of predicted to experimental peak forces for the 0.5 mm thickness 1100 Al specimens
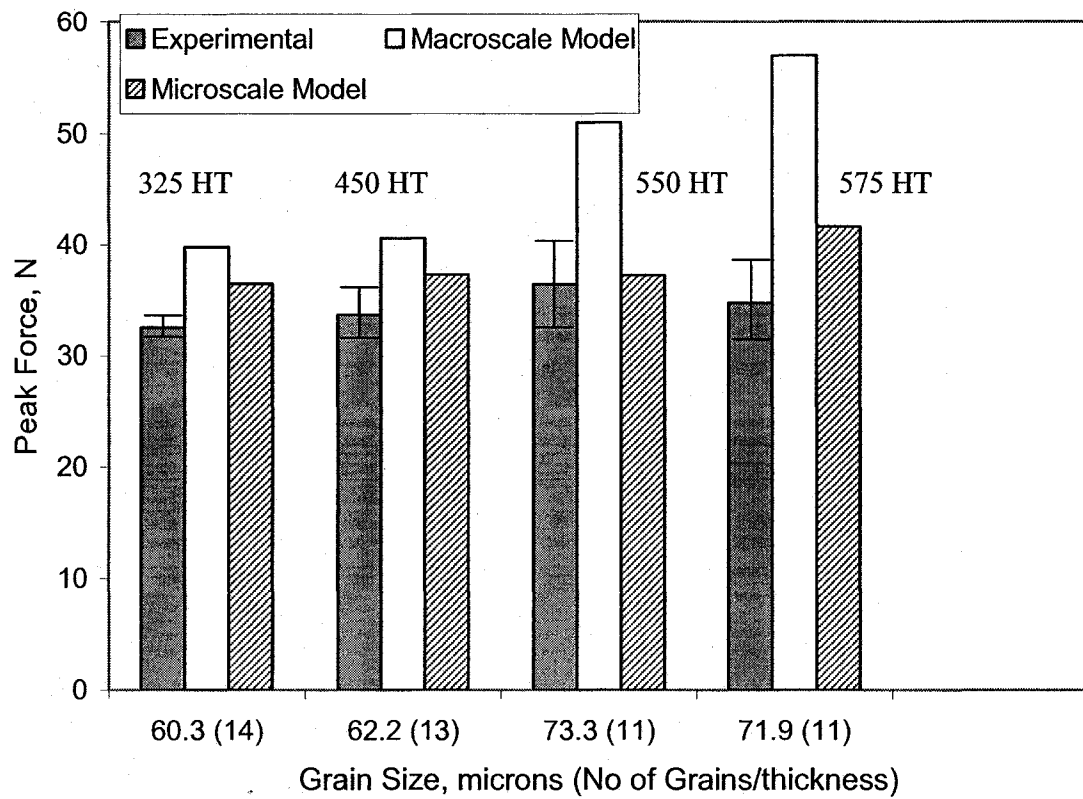
Figure 36 Comparison of predicted to experimental peak force for 0.813 mm thickness 1100 Al specimens
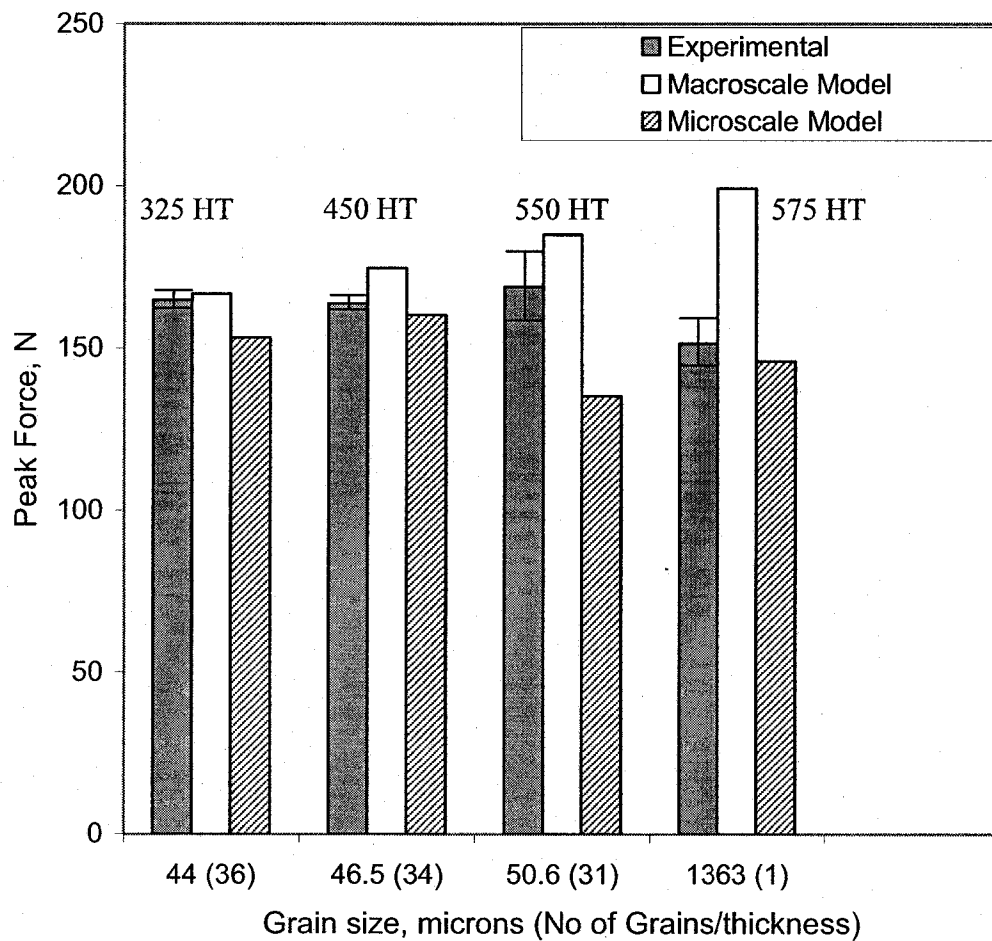
Figure 37 Comparison of predicted and experimental peak forces for 1.588 mm thickness 1100 Al specimens

Discussion - Aluminum

The macroscale model predicts the macroscale cases i.e. those with more than about 15 grains through the thickness more accurately than the microscale model does except for 1.588 mm thickness 450 °C heat treat. The microscale model is more accurate in predicting the peak force for all microscale cases except for the 0.254 mm 325 °C heat treat with 10 grains, and 0.508 mm 575

70

heat treats with less than 1 grain through the thickness. For the microscale cases with 2 grains through the thickness or less, the grain orientation of each grain has a very significant effect, on the experimental peak forces seen. For example while the 0.127 mm, 0.508 mm and 1.588 mm heat 575 $^{\circ}$C treat specimens each have about 2 grains or less through the thickness, they responded differently to the microscale model with the 1.588 mm case being predicted more accurately by the microscale model and the other two being predicted more accurately by the macroscale model. There is increasing scatter with decreasing number of grains through the thickness similar to that which has been shown by previous work [11, 12].

71

CHAPTER II

EXTRUSION

Background

The second process investigated in this research is forward microextrusion which is used to fabricate components such as the micropins shown in Figure 38. In forward extrusion, material is forced through a die to vary the initial billet into the final desired shape. Here the diameter of a cylindrical billet will simply be reduced during the process. Extrusion is a high rate process and therefore ideal for mass production. There are several process models that are available for predicting the extrusion force such as those described by Avitzur [36], Bhupatiraju et al. [37], Sheppard [38], Lange [39], Kalpakjian & Schmid [23], and Groover [40]. These models cannot simply be used at the microscale as they need to be modified to account for size effects.

72
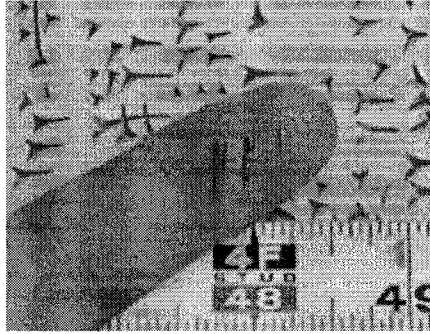
Figure 38 Cold forward extruded micropins [41]

Again, specimen size effects occur when only a few grains (less than approximately 15) are present through a feature of interest (e.g. diameter in this case). This is due to variations in the ratio of volume grains to surface grains, which have fewer physical restrictions. Furthermore, scatter increases when only a few grains exist through a feature due to variations in the grain orientation. According to Armstrong [6] the specimen size effect is independent of grain size.

Another variation due to size effects that has been demonstrated in past research is changes in the deformation pattern. Such deformation size effects were shown to exist in microbending i.e. change in strain distribution through the cross section and formed wall shape and may exist in microextrusion as well. To assure accurate prediction of microscale process parameters, the process models used must account for such size effects. As with microbending, "macroscale" model assumptions in micrextrusion need to be reevaluated for the deformation in the microscale process.

In this chapter, a new process model is developed for forward microextrusion that more accurately predicts the increased simple shear

73

deformation which occurs as the number of grains through the diameter decreases. When the traditional "macroscale" models are used to predict the peak extrusion force, the increased simple shear deformation is not accounted for and therefore the peak forces are under-predicted. The microscale model that is developed here captures this variation in the deformation and more accurate results are obtained.

Experimental Investigation

The experimental setup that was used to measure the force-displacement response is given in [14] and summarized here. This experimental work was performed by collaborators at Northwestern University. A segmented die, see Figure 39, was mounted onto a specially designed forming assembly, see Figure 40. This forming assembly consists of a ram mounted on a yoke that slides along linear bearings to guide the ram into a segmented die that is mounted and clamped in a die block. This assembly was then inserted onto a loading stage equipped with an 8909 N (2000 lb) capacity load cell and an LVDT to measure the ram displacement.

Three dies were used with the following inlet/outlet diameters of 0.76/0.57 mm, 1.50/1.00 mm and 2.00/1.33 mm. The larger dies were fabricated using standard drilling and then polished using a lapping compound, while the smallest

74

ones were fabricated using EDM. This gave average surface roughness (R_a) values of between 0.8 and 1.0 µm.

The extrusion specimens were made from brass (CuZn30) with three different grain sizes viz. 32 µm (heat treated at 550°C for one hour), 87 µm (heat treated at 610°C for 1 hour) and 211 µm (heat treat at 700°C for 1 hour). The specimens were fabricated in such a way as to ensure similar surface finishes were obtained. These specimens were then extruded and ram-force-displacement plots obtained. Three tests were conducted for each case to assure repeatability. The average peak force results are presented in Figure 44.

The experimental peak extrusion force decreases with increasing grain size due to material property changes. This decrease is observed for all three die sizes.
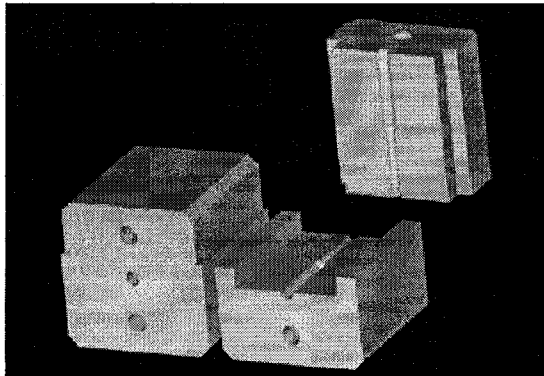
Figure 39 Segmented die used for microextrusion [14]

75
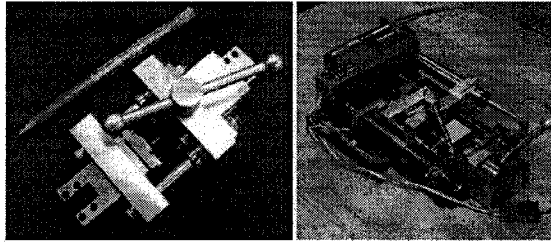
Figure 40 Forming assembly and tensile loading stage [14]

Tensile tests were conducted for each grain size to obtain the strength coefficient, K, and the strain hardening exponent, n, (for the power hardening law). From these parameters, the average flow stress was calculated using [40]

$$\sigma_o = \frac{K\bar{\varepsilon}^n}{1+n} \tag{34}$$

The material properties determined are shown in Table 5. Assuming a power hardening model provides very consistent results as can be seen from Figure 41 in which the results of the power hardening model are compared to experimental tensile data. This confirms that this model is valid for brass especially at higher strains.

The patterns for the material properties are the same as was observed for the microbending material tests. The flow stress, equivalent to yield strength, decreases with increasing grain size, which follows the Hall-Petch relationship, as well as decreasing with specimen size. The strain hardening exponent, on the other hand, increases with increasing grain size due to the increased annealing. Finally, the strength coefficient does not have a consistent pattern. Again the cause of this phenomenon is the methodology to determine the strength coefficient value from the experimental data. The strength coefficient is determined from the intersection of a log stress versus log strain plot with a log

76

strain value of zero, which is equal to a value of unity for strain. The decreasing yield stress and the increasing strain hardening exponent are competing factors, which lead to either a decrease or an increase in the strength coefficient respectively. Thus, a pattern is not observed with this material parameter. Note that both specimen and grain size effects are accounted for in the process models through adjusting of these material parameters.

Table 5 Tensile test material properties for brass (CuZn30) used in the investigation

Grain size, (microns)	K, (MPa)	n	Flow Stress (MPa)		
			0.76/0.57	1.5/1.0	2.0/1.33
32	853.6	0.513	423.46	506.60	508.20
87	890.9	0.601	397.78	490.68	492.49
211	834.9	0.638	356.63	445.74	447.49
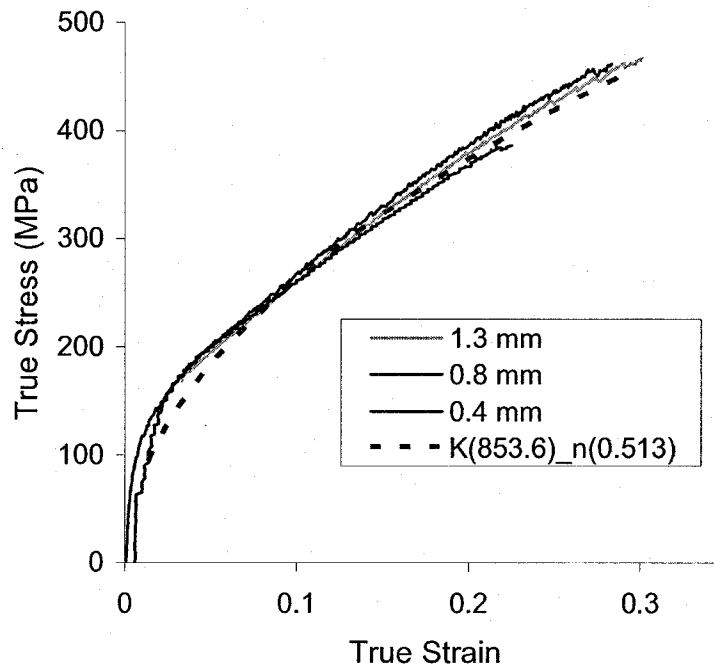
Figure 41 True stress vs. true strain for brass (32 micron grain size) for different sheet thicknesses

The deformation of the extruded pins was investigated by conducting microhardness tests and x-ray texture analysis and the results are reported in [15, 42]. A brief summary of the results of these investigations is given below. From the microhardness tests, it was found that surface grains had higher hardness values than interior grains for all grain sizes, see Figure 42 for a plot from the Ø0.76/0.57 mm reduction case. This implied that surface grains experienced higher strain hardening than the interior grains. Due to more simple shear deformation that occurs at the surface due to the diameter reduction and frictional effects.

78
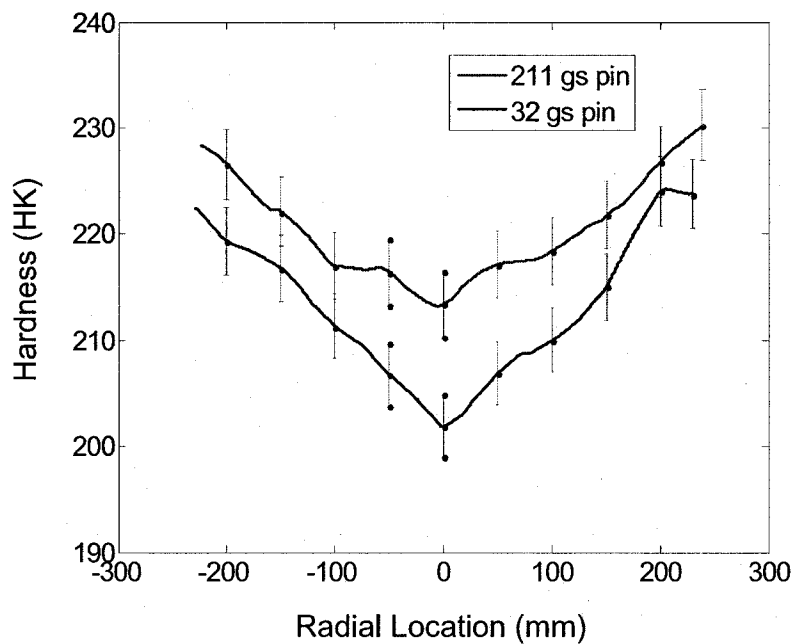
Figure 42 Average hardness distribution in the radial direction of coarse and fine grained extruded pins for the Ø0.76/0.57 mm reduction case[42]

More simple shear deformation occurs in the center of microextrusion specimens as the number of grains through the diameter is reduced [42]. See Figure 43 for the microstructure analysis pictures of pins with 32 μm and 211 μm grain sizes reduced from ø0.76 mm to ø0.57 mm. Microhardness tests [42] have indicated that the hardness of submillimeter microextruded specimens increases with increasing grain size, see Figure 42, which seemingly contradicts the Hall-Petch effect. It has also been shown by use of x-ray texture analysis techniques [42] that coarse grained pins experience higher strain hardening than fine grained pins due to increased shear deformation penetration, This clearly indicates the existence of deformation size effects.

79
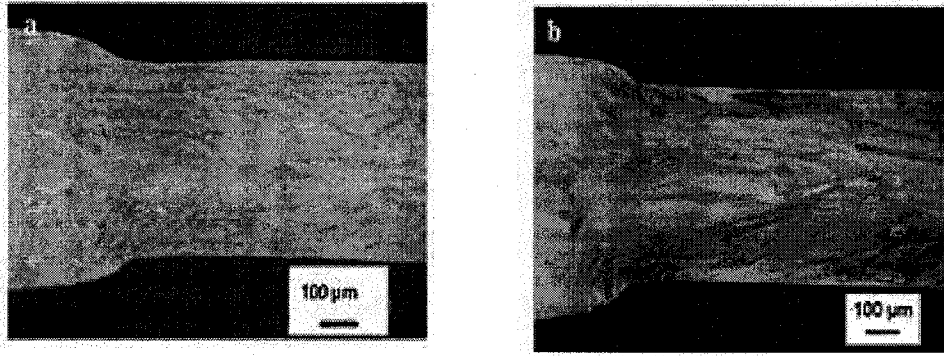
Figure 43 Microstructure of (a) 32 micron and (b) 211 micron grain size extruded pins for the Ø0.76/0.57 mm reduction case [41]

Macroscale Extrusion Model

There are many traditional macroscale models available for predicting the peak extrusion force. For this investigation, a slab analysis model for cold axisymmetric forward extrusion proposed by Altan et al. [43] was used. This model being an upper bound model predicts the maximum possible value for the extrusion force therefore it was selected to see if it would accurately replicate the increased shear stress that is observed in microscale cases. According to this model the extrusion force is given as

$$F = F_{hd} + F_{sd} + F_{cf} + F_{df} \qquad (35)$$

Where,

$$F_{hd} = \pi r_0^2 \sigma_0 \ln(R) \qquad (36)$$

80

$$F_{sd} = 2\pi r_0^2 \tau \left(\frac{\alpha}{\sin^2 \alpha} - \cot \alpha \right) \tag{37}$$

$$F_{df} = \pi r_0^2 \frac{\sigma_0}{\sqrt{3}} m_3 \frac{\ln(R)}{\sin \alpha \cos \alpha} \tag{38}$$

$$F_{cf} = 2\pi r_0 L m_4 \frac{\sigma_0}{\sqrt{3}} \tag{39}$$

F_{hd} is the force required for homogeneous deformation of the material, F_{sd} is the force required for internal shearing due to inhomogeneous deformation, F_{cf} is the force required to overcome the cylinder wall friction and F_{df} is the force required to overcome the die wall friction.

The variables in these equations are r_0 which is the initial radius of the billet, σ_0 which is the average flow stress, R which is the reduction ratio, α the die angle, L the billet length before extrusion, and m_3 and m_4 which are the friction factors at the cylindrical and conical sections respectively. These friction factors are assumed to be constant and equal because of the similarity of the surface topographies for the cylindrical and conical sections and because the same material and fabrication process was used in the production of both areas. Therefore the friction factor for each die is given as a constant m. For high pressures such as those experienced in metal forming, the assumption of a constant friction factor m is more prevalent than that of a coulomb friction factor [44].

Microscale Extrusion Model

As was found in the work by Parasiz et al. [42], more simple shear deformation occurs for coarse grain size microscale pins, therefore, the traditional macroscale model must be adjusted to account for this increased simple shear as the grain size increases and the specimen size decreases. The force term which was focused on for this adjustment was the internal shear deformation term F_{sd} in Eq. (37). The reason for this is that from all the evidence this is the only term that seems to suffer significant size effects. The adjustment proposed is based on the surface layer model [5] as discussed below.

The geometry of the specimen is divided into two sections − surface (outer) and volume (inner) areas [5]. The behavior of the surface grains is assumed to be similar to that of a single grain/crystal, while the volume grains are assumed to behave like a polycrystalline material. This model was initially developed to account for the reduced flow stress observed on the surface grains [45]

$$\sigma_t = \alpha_v \sigma_{f,v} + \alpha_s \sigma_{f,s} \tag{40}$$

where σ_t is the total flow stress, α_i is the decimal percent of the volume grains, α_s is the decimal percent of the surface grains, $\sigma_{f,v}$ is the flow stress of the

82

volume grains, and $\sigma_{f,s}$ is the flow stress for the surface grains. The grains are either considered volume or surface grains, i.e.:

$$1 = \alpha_v + \alpha_s \qquad (41)$$

The same methodology is applied with regard to the shear stress experienced at the extrusion cylinder wall i.e. divide the geometry of the specimen into two sections viz. surface and volume areas. The transition from volume to surface is taken to be discontinuous. The surface grains experience simple shear due to friction on the wall and the reduced effect of grain boundaries. The interior grains on the other hand experience pure shear deformation which is modeled accurately using standard yield criteria such as the Von Mises yield criterion. The proportion of grains experiencing simple shear increases with increasing grain size and/or decreasing specimen size. Since surface layers are typically a couple grains thick, "single grain" mechanisms are assumed for these layers. The shear stress associated with the surface layer is therefore based on single grain mechanisms. According to the Schmid Law, "a single crystal yields on any particular slip system if the shear stress resolved on that slip plane and slip direction reaches a critical value, the yield strength, on that slip system" [46]. The shear stress for a single grain is given by:

$$\tau_s = M\sigma_0 \qquad (42)$$

83

where M is an orientation factor obtained by taking the average of the orientation factors given by the Taylor model, which is an upper bound model, and the Sach's model which is a lower bound model. The average value of M is 2.65 which is used here.

The shear stress for the volume grains is obtained by assuming Von Mises yield criterion and is given as

$$\tau_v = \frac{\sigma_0}{\sqrt{3}} \qquad (43)$$

Therefore the total shear stress experienced by the billet is

$$\tau = \alpha_v \tau_v + \alpha_s \tau_s \qquad (44)$$

According to Geißdörfer et al. [5], the ratio between grain size and work piece dimension controls size effect on material flow. Therefore for this model the share of surface grains is given by

$$\alpha_s = \frac{d}{D_0} \qquad (45)$$

84

where d is the average grain size and D_0 is the billet diameter. Substituting τ in Eq. (37) gives the modified force required for the inhomogeneous shear deformation that takes place during the extrusion process viz.

$$F_{sd} = 2\pi r_0^2 \left(\alpha_i \frac{\sigma_0}{\sqrt{3}} + \alpha_s M\sigma_0 \right) \left(\frac{\alpha}{\sin^2 \alpha} - \cot \alpha \right) \tag{46}$$

This is then substituted into Eq. (35) to obtain the microscale extrusion model as shown in Eq. (44). Note that the only difference between the forward extrusion models is the equation used for the internal shear deformation term (F_{sd}), either Eq. (37) or Eq. (46) for the macroscale and microscale models respectively.

$$F = \pi r_0^2 \sigma_0 \ln(R) + 2\pi r_0^2 \left(\alpha_i \frac{\sigma_0}{\sqrt{3}} + \alpha_s M\sigma_0 \right) \left(\frac{\alpha}{\sin^2 \alpha} - \cot \alpha \right) +$$
$$\pi r_0^2 \frac{\sigma_0}{\sqrt{3}} m_3 \frac{\ln(R)}{\sin \alpha \cos \alpha} + 2\pi r_0 L m_4 \frac{\sigma_0}{\sqrt{3}} \tag{47}$$

Comparison of Macroscale and Microscale Models with Experimental Results

The friction factor to use in the process model was not known for each die. Recall that Mori et al. [7] demonstrated that the friction factor does not vary with grain size. Thus, a single friction factor could be used for each die size. In order to determine this parameter, the experimental extrusion force for the 32 μm grain size case which is considered macroscale, due to the large number of grains through the thickness (approximately twenty four), was used in the traditional

85

macroscale slab analysis model. With the extrusion force specified, it is possible to solve for friction factor m which is the only unknown in Eq. (35). The value of m obtained was then used to predict the extrusion force for the 87 and 211 µm cases. This was done for all the die sizes.

The predicted results for the macroscale and microscale models are shown in Figure 44 along with the experimental data for comparison purposes. Both models show a decrease of peak extrusion force with increasing grain size which is in agreement with the experimental trends. Note that since the experimental force for the 32 µm case was used in the models to predict the friction factor for a given die size, the forces match exactly.

86

(A)
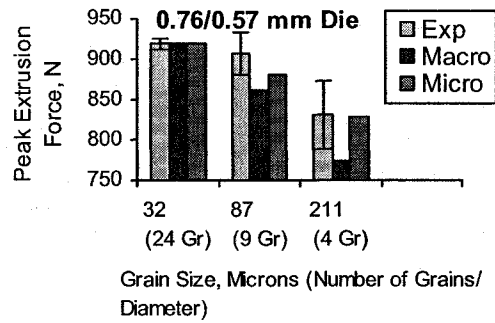
(B)
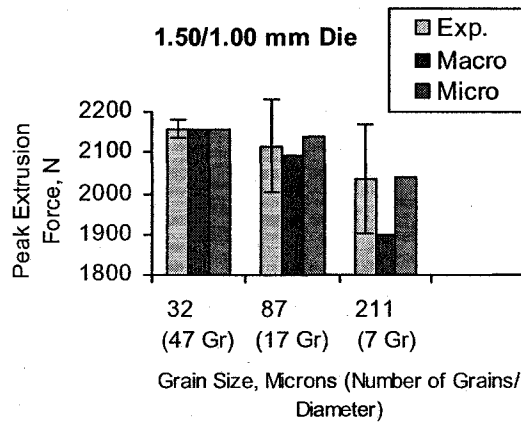
(C)
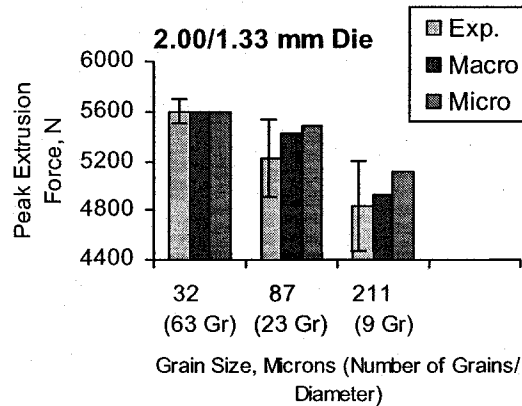
Figure 44 Comparison of macroscale and microscale predicted peak extrusion forces with experimental peak extrusion forces for (a) 0.76/0.57 mm, (b) 1.50/1.00 mm, and (c) 2.00/1.33 mm dies

87

Discussion

Recall that one measure to define a specimen as being microscale is if less than approximately fifteen grains exist through the diameter. The macroscale model provides more accurate results with respect to the experimental peak extrusion force for the macroscale cases of the 1.50/1.00 mm die and 2.00/1.33 mm die with 87 μm grain size and 17 and 23 grains through the diameter respectively. For those cases with the 0.76/0.57 mm die and 1.5/1.0 mm die and less than 10 grains through the diameter the macroscale model under-predicts the peak force by as much as 7%. For these cases, the microscale model, on the other hand, under-predicted the peak extrusion forces to within 2.7% for microscale specimens. The largest improvement in using the microscale model instead of the macroscale model was found in the case with four grains through the diameter for the 0.76/0.57 mm die, 7% to 0.3% for the macroscale and microscale models respectively.

An exception to the trends for the macroscale and microscale models is the 2.0/1.33 mm die case with 211 μm grain size and about 9 grains through the diameter. The macroscale model over-predicts the peak extrusion force for this case and the microscale model further over-predicts the value. This difference possibly demonstrates an interaction between the specimen size effects and the grain size effects.

88

CHAPTER III

FINITE ELEMENT SIMULATION OF MICROBENDING PROCESS

Background

The use of computer tools in the design and optimization of manufacturing processes has increased greatly since the 1990's. These tools play a very significant role in enabling the simulation, analysis and optimization of different processes before they are implemented. The optimization of a process requires that the designer understands how the different parameters such as the material properties, work piece geometry and friction affect the process. This understanding is developed by running simulations of the process. The simulation can be done using either a commercially available general purpose software such as Algor, Abaqus, MSC. Marc, and ANSYS among others or it can be done with special purpose packages that have been developed to solve specific problems. The advantages of using the general purpose packages over the special purpose ones include [47]:

- User interfaces to ease use of the software

89

- The ability to solve many different types and sizes of problems with the same input format.

- Addition of new modules to solve new types of problems or to take advantage of new technology

- Implementation on desktop computers

- Very cost effective for given range of capabilities

One downside of general purpose FEA packages is their lower efficiency because of the wide range of parameters which needs to be checked which would not be required for special purpose software.

The advantages of the special purpose packages include [47]

- High program efficiency

- Ease of adding to the program at low cost

- Implementation on desktop computers

The one main disadvantage of special purpose packages is the limited range of problems that each package can solve.

The goal of this part of the research was to evaluate whether commercially available FEA software would capture one observed phenomenon in microforming, increased scatter due to miniaturization. The ability of the FEA software to reasonably model the bending process was also evaluated. Past research by Geißdörfer et al. [5] emphasized the generation of complex meshes based on the crystal structure. Gailletaud et al. [48] have also presented details of the β-model and other FEA computational tools that they say significantly

90

reduce the computational resources needed. The Reproducing Kernel Element Method (RKEM) developed by Cao et al. [14] addresses some of the limitations of FEM in microforming simulations. There are numerical tools available through these special purpose packages to simulate microforming. The approach taken in this part of the research was more simplistic and was aimed at evaluating the ability of the nonlinear finite element package MSC. Marc to capture scatter effects that are observed at the microscale. MSC. Marc, which is a general purpose FEA package was used to simulate the microbending process. As with most FEA packages Marc includes continuum mechanics assumptions, such as the homogeneity of the work piece which may not apply at the microscale. It provides a high level of flexibility to the user in areas such as the design details, control of the mesh, material properties, and load case functions. Here, the simulation of grains by assigning different material properties to groups of uniform elements was investigated. Because the bending process investigated involves deformation, plastic properties (strength coefficient and work hardening exponent) of the materials were assigned to different groups of elements that represent grains. These properties were empirical values calculated from tensile tests of material that was cut at 0, 45 and 90 degrees to the rolling direction [20]. Isotropic elasticity was assumed in all cases because the deformations being studied are dominantly plastic and Marc did not handle elastic anisotropy accurately.

91

FEA Implementation

The microbending process was modeled as a flanging contact problem with a fixed rigid die and a moveable rigid punch, see Figure 45. This is the same set up from LFT bending experiments, where $L_d = 6t$, $R_d = 4t$, $R_p = 0.25$ mm, and t is the sheet thickness. The motion of the punch was prescribed to a vertical depth of 8t.
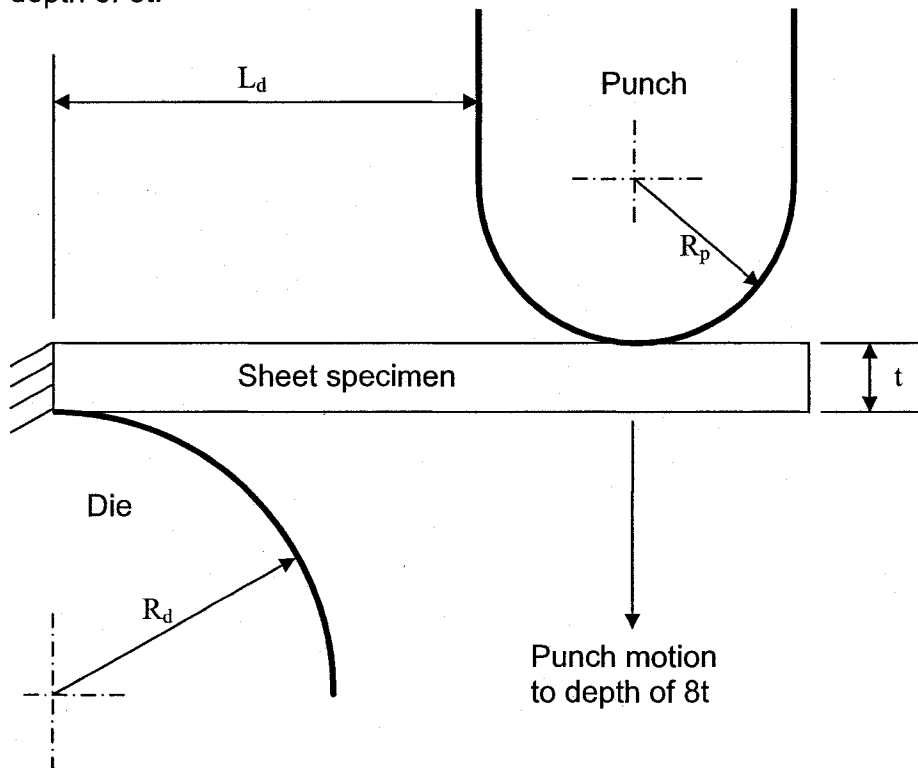
Figure 45 Flanging process geometrical set up for the FEA simulation

The width of the specimen was assumed to be 10 mm, and it was therefore modeled as a plane strain problem. The specimens were discretized using four node, isoparametric arbitrary quadrilateral elements (element type 11 in Marc), developed for plane strain applications. The strains in this element type tend to be constant throughout the element because of the bilinear interpolation

92

functions that are used. The element stiffness is calculated using four-point Gaussian integration, see Figure 46. For contact problems, this is the recommended element type and thus was used here [49]. A coefficient of friction of zero was assumed between all surfaces in contact.
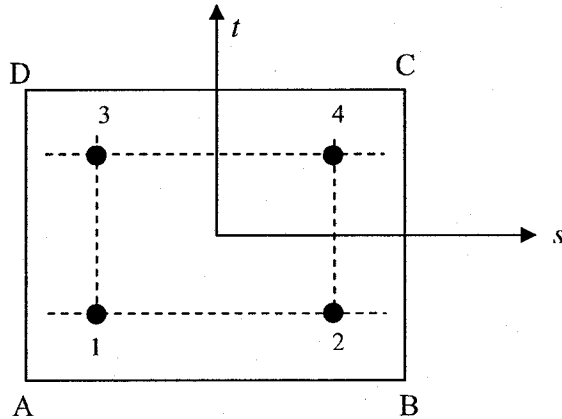
Figure 46 Gaussian Integration Points for element type 11 in Marc

Integration point locations are given by

$$s_i, t_i = \pm \frac{1}{\sqrt{3}}$$, where: A,B,C and D are the nodes
$$i = 1,2,3,4$$

To model a strain hardening anisotropic material, Marc allows the use of several different material models. These models are differentiated primarily in how they handle the elastic effects, yield function, flow rule and hardening rules. The models available in Marc include the following:

93

Elasticity Models:

- Isotropic

- Orthotropic

- Anisotropic

- Hypoelastic

Among others

Plasticity Models

- Elastic-plastic

- Rigid-plastic

Hardening Rules: Isotropic, Kinematic and Combined

Plasticity Methods

- Piecewise linear

- Power law

- Rate power law

- Chaboche

- Kumar

- Johnson-Cook

- Viscoplasticity

To model brass, the isotropic elastic-plastic isotropic hardening model was used. This model treats the material as isotropic until it reaches the yield point and the post yield behavior is controlled by the work hardening rule that is assumed, in this case the Power Law isotropic rule. The center of the yield surface is taken to be at a stationary point in the stress space but the size of the yield surface

94

increases as the material flows beyond the yield point [50]. In this model, yielding is assumed to initiate when the following equation, that represents a special case of uniaxial loading, is satisfied

$$\sigma_y = K\left[\sqrt{\frac{2\left(1+2v^2\right)}{3}}\frac{\sigma_y}{E}\right]^n \qquad (48)$$

where σ_y is the flow stress at yield, K is the strength coefficient, n is the work hardening exponent, E is Young's modulus and v is Poisson's ratio. The power law model is selected because it matches the experimental data reasonably well, see Figure 9. As shown from Eq. (24) the flow stress $\overline{\sigma}$ is given by

$$\overline{\sigma} = K\overline{\varepsilon}^n \qquad (49)$$

where K is the strength coefficient, n is the work hardening exponent, and ε_0 is the pre-strain experienced by the material which is assumed to be zero. Note that strain rate effects were not considered due to the quasi-static nature of the process.

The specimens were designed to be t mm thick by $10t$ mm long, with 2000 elements for the 0.1 mm thick specimens and 25000 elements for the 0.5 mm specimens. This was to maintain the same element density so that any differences between the fine and coarse grained specimens would solely be due to the difference in grain sizes. To simulate the effect of grains, a number of elements were grouped together, in a consistent pattern, and assigned different plastic material properties. An Elastic-plastic plasticity model using the Power Law method was assumed for all cases, with Young's modulus of 110 GPa and a

95

Poisson's ratio of 0.34. Examples of a fine and a coarse grained material are shown in Figure 47.

(a)

96

(b)
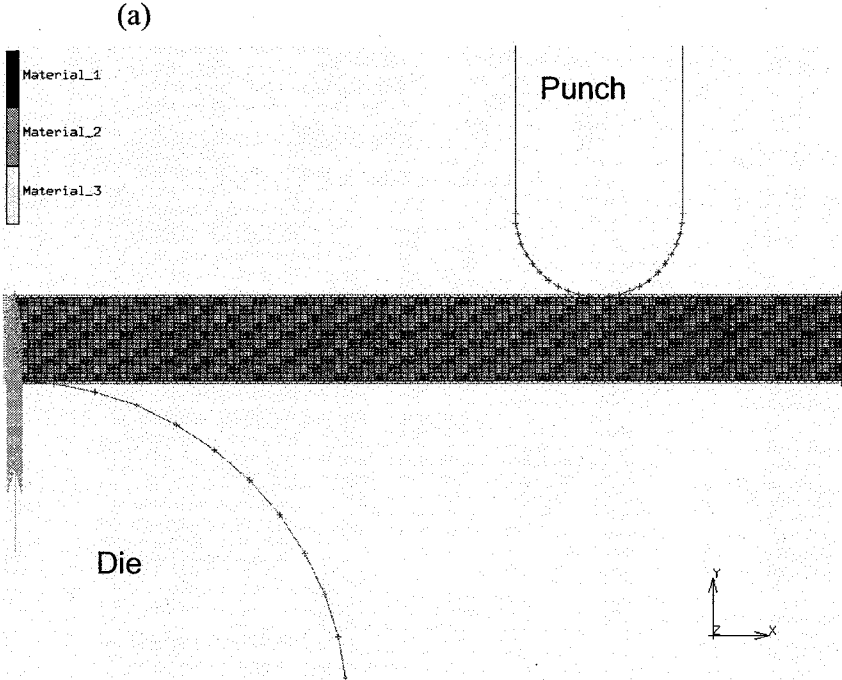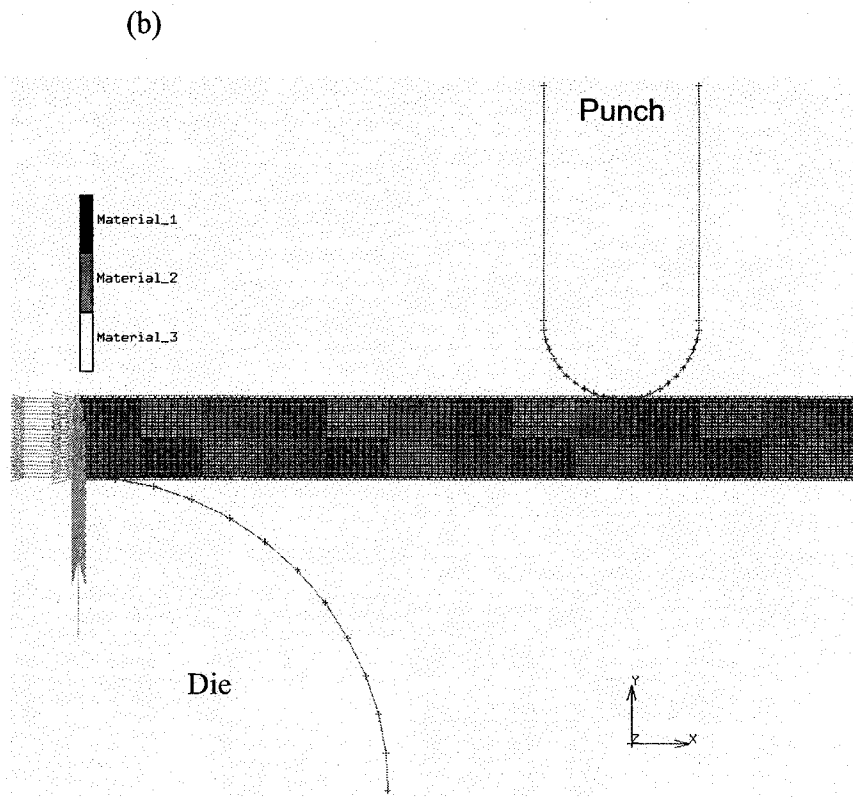
Figure 47 Model of a 0.1 mm thick (a) fine (~10 micron) and (b) coarse (~50 micron) grained specimen showing grains of different orientations

The properties of the material were assumed to be isotropic elastic and anisotropic plastic. This is because of the much larger plastic strains that are experienced as compared to the small elastic strains, so that any anisotropy in the elastic region will have minimal effect on the observed overall anisotropy. In metals, anisotropic plastic properties are due to directional effects of prior cold working. Uniaxial tensile test specimens that are cut at different orientation angles to the rolling direction are used to determine the plastic properties of the material for this preliminary investigation. Using tensile test data for CuZn15 from [25] the strain hardening parameters for specimens cut at 0°, 45° and 90° to the rolling direction were found, see Table 5.

97

Table 6 Variation of plastic material constants with rolling direction for CuZn15 specimens

Sheet Thickness, mm	Av. Grain Size, microns	Av. No. of Grains Through Thickness	Yield stress, MPa			Strength Coefficient, K, MPa			Work Hardening Exponent, n		
			0 deg	45 deg	90 deg	0 deg	45 deg	90 deg	0 deg	45 deg	90 deg
	17	6	356.3	327	360.7	431.8	337.2	439.6	0.036	0	0.031
0.1	23	4	96.2	62	98.7	525.8	655.5	645.2	0.339	0.415	0.441
	53	2	60.5	35	66.7	471.9	716.5	680.1	0.412	0.52	0.576
	10	50	346.1	333	336.7	492.8	425	483.6	0.070	0.053	0.08
0.5	28	18	104.0	93	106.3	576.1	542.5	674.8	0.353	0.275	0.427
	71	7	70.0	41	59.5	587.2	505.6	717.6	0.432	0.362	0.524

As with the other material data presented in this thesis, the strength coefficient did not show a consistent pattern other than that the value at 45 degrees to the rolling direction was lower than those for the 0 and 90 degrees for all cases except the 0.1 mm Heat treat II case. The work hardening exponent increased and the yield stress decreased with increasing grain size for all the three thicknesses at all the three angles to the rolling direction as noted previously.

During the rolling process the grains elongate and a preferred crystallographic orientation of grains occurs resulting in directional anisotropy of the rolled sheet. From x-ray diffraction studies it has been shown that in the rolling direction the {112} <111> grain orientation occurs as the major orientation with the {110} <100> as the minor orientation [3, 48] for materials such as 1100 aluminum, copper, silver and brass. In this orientation, in which the crystals line up with the <111> direction parallel to the rolling direction, the material exhibits its highest strength. At 45 and 90 degrees from the rolling direction, it follows that for rolled sheets, different grain orientations exist leading to different anisotropic

98

properties. The strength coefficient and the work hardening exponent values determined for specimens cut at 0, 45 and 90 degrees to the rolling direction are used to characterize the plastic anisotropy of the specimens. These values, see Table 6, were used in the Marc simulations to model plastic anisotropy. It is important to note that this is only a preliminary investigation and that these values do not represent different crystallographic orientations of the lattice structure.

Results

One of the goals was to determine if the increased scatter could be predicted by FEA simulations. Therefore, the material properties for the different meshes were altered to determine if a noticeable change in scatter would occur as the grain size increased, as observed experimentally. Since there are three different materials, there are six different variations for the material assignments, represented as O-E in Table 7 and Table 8. For comparison purposes four parameters were used viz. peak bending force, von Mises stress (maximum and residual), equivalent plastic strain and springback. The results are shown in Table 7 and Table 8. The springback was determined by subtracting the residual displacement from the maximum displacement in the y-direction of the bottom right corner node of the mesh.

99

Table 7 Comparison of simulation results for 0.1 mm CuZn15 specimens with different grain sizes

Grain size, μm	Pattern	Peak Force, N	Von Mises Stress, MPa		Displacement, mm		Springback, mm	Eq.Plastic Strain
			Max	Residual	Max	Residual		
10	O	34.4	445.3	367.6	0.486	0.478	0.008	0.251
	A	30.2	452.7	332.8	0.693	0.685	0.008	0.293
	B	32.9	456.9	342.5	0.692	0.686	0.006	0.282
	C	33.0	448.0	343.0	0.693	0.686	0.007	0.270
	D	31.1	453.1	406.5	0.693	0.685	0.008	0.288
	E	32.1	442.7	328.4	0.693	0.686	0.007	0.290
50	O	12.6	286.4	195.7	0.484	0.478	0.006	0.212
	A	12.8	294.5	194.3	0.484	0.479	0.005	0.234
	B	13.7	306.1	185.7	0.484	0.478	0.006	0.194
	C	13.9	300.5	200.1	0.484	0.479	0.005	0.232
	D	11.7	251.3	164.5	0.483	0.478	0.005	0.179
	E	12.9	323.9	237.4	0.484	0.479		0.215

Table 8 Comparison of simulation results for 0.5 mm CuZn15 specimens with different grain sizes

Grain size, μm	Pattern	Peak Force, N	Von Mises Stress, MPa		Displacement, mm		Springback, mm	Eq.Plastic Strain
			Max	Residual	Max	Residual		
10	O	169.6	490.1	439.3	3.480	3.396	0.084	0.326
	A	171.4	451.9	469.3	3.479	3.370	0.109	0.281
	B	165.6	475.0	451.9	3.480	3.377	0.103	0.290
	C	164.2	473.9	462.8	3.481	3.363	0.118	0.280
	D	167.7	498.7	451.7	3.480	3.358	0.122	0.272
	E	169.1	470.9	438.6	3.479	3.428	0.051	0.266
100	O	82.1	315.7	288.8	3.467	3.414	0.053	0.334
	A	76.5	297.3	297.8	3.466	3.433	0.033	0.320
	B	83.8	322.8	391.0	3.467	3.073	0.394	0.367
	C	81.7	300.2	314.5	3.467	3.433	0.214	0.394
	D	78.0	305.2	480.5	3.466	2.208	1.258	0.564
	E	82.6	356.4	386.8	3.467	2.733	0.734	0.441

The scatter (variation) of each of these data sets was computed so that it could

be compared between the macroscale and microscale cases and the results are

100

shown in Table 8. All the microscale cases show significantly higher scatter than the macroscale cases for all the four parameters recorded.

Table 9 Comparison of scatter of different parameters with grain size for CuZn15 FEA simulations

Thick, mm	Grain size, µm	Peak Force Scatter %	Von Mises Stress Scatter, %		Springback Scatter %	Eq. Plastic Strain Scatter, %
			Max	Residual		
0.1	10	13.9	3.2	23.8	14.3	16.7
	50	18.8	28.9	44.3	20.0	30.7
0.5	10	4.4	5.9	5.5	139.2	26.0
	100	9.5	19.9	66.4	3712	76.3

Discussion

The scatter pattern observed in Table 9 is consistent with that which is expected viz. as the grain size increases (i.e. with fewer grains through the thickness) the scatter increases. It is also observed that the higher the change in grain sizes for a given thickness, the higher the amount of scatter. The 0.1 mm thick specimen cases with a 5 times change in grain size showed less increase in scatter than the 0.5 mm thick specimens which had a 10 times change in grain size. These observations are for all the four parameters that were recorded. Comparing these results to the experimental results and the predictions from the macroscale and microscale process models from Chapter I, see Figure 48 and Figure 49, shows clearly that Marc simulations predict the peak bending force reasonably well for the 0.5 mm specimen cases but over predict the peak bending force for all the 0.1 mm cases.

101
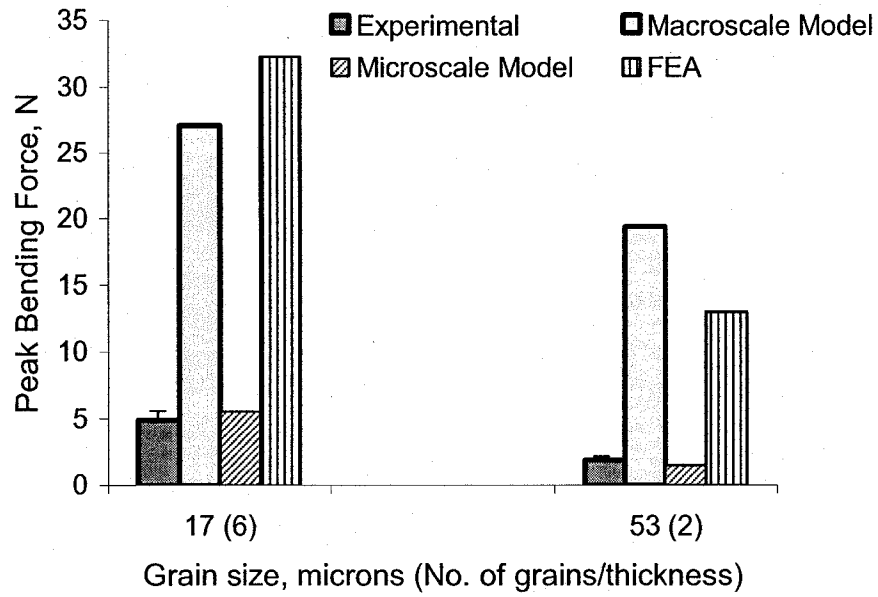
Figure 48 Comparison of FEA predicted peak forces for 0.1 mm specimens with the experimental and other models

102
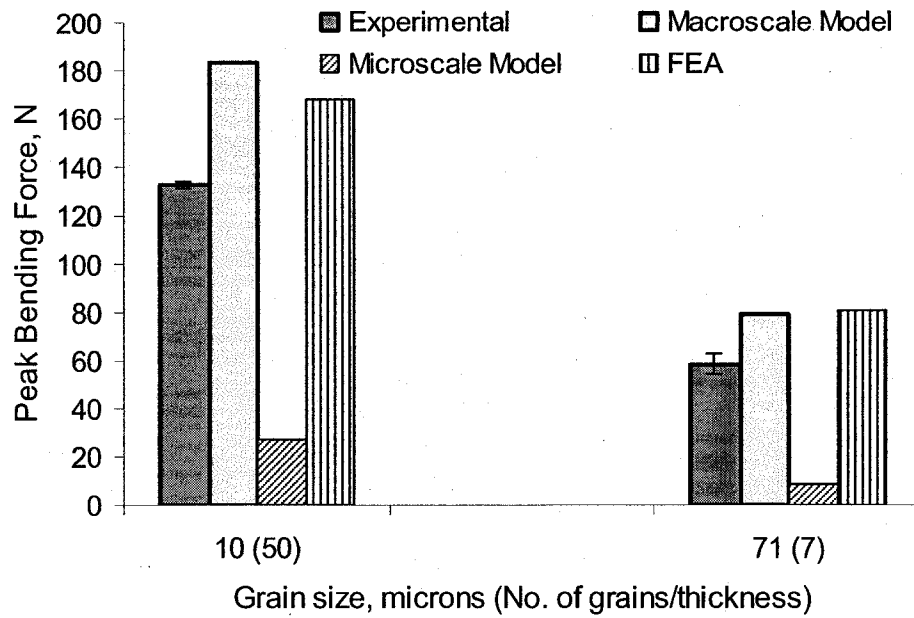
Figure 49 Comparison of FEA predicted peak forces for 0.5 mm specimens with experimental and other models. The FEA models used 10 and 100 micron size grains

Some of the assumptions that were made with regard to these simulations include:

- regular square mesh

- Effect of grain boundaries was neglected

- Isotropic elastic response of the material

- Perfect bonding between grains

- Perfect grain alignment

- Regular uniform grains among others

Keeping these assumptions in mind the results that were obtained were reasonable and go to show that this commercially available software works reasonable well for macroscale processes. For the 0.1 mm microscale cases the

103

peak forces simulations are significantly higher than the experimental values. This follows the surface layer model for microforming. For the 0.5 mm cases the simulation results are very close to those of the macroscale model. As stated previously, the 0.5 mm (100 μm) does not follow the expected pattern as there are only 7 grains through the thickness thus the microscale model was expected to provide a better prediction.

Despite the fact that this was a preliminary investigation it has been shown that the increased scatter size effects can be observed in the modeling of microscale processes using Marc Mentat. The accuracy of these results is dependent on the accuracy of the plastic material constants that are used to characterize the anisotropy of the material and the assumptions listed on the previous page.

104

CHAPTER IV

CONCLUSIONS

As the race towards further miniaturization of components and systems continues, it is crucial to have process models that can accurately predict process parameters at the microscale. In this dissertation macroscale bending and extrusion process models were investigated for use with microscale processes. New microscale process models are proposed that predict peak forces more accurately than the existing macroscale models. A specimen was deemed to be in the microscale if it had no more than approximately fifteen grains through the thickness.

Bending

The accuracy of the models investigated was governed by two critical bending process model assumptions viz. the shape of the formed wall and the strain distribution through the material thickness. For the microscale data (both brass and aluminum), the models that assumed a linear strain distribution and a straight formed wall provided the most accurate predictions of the peak force. As the number of grains through the thickness and the length of the formed wall

105

decreases, a linear strain distribution through the thickness and a straight formed wall are physically more reasonable assumptions. Alternatively, for the macroscale data, models that include a logarithmic strain distribution and a curved formed wall provided more accurate peak bending force results. For the mesoscale cases, the experimental results were in between the microscale and the macroscale process model predictions. Based on this work, it can be concluded that size effects in the bending process model assumptions exist and need to be correctly accounted for in order to accurately model the process. It should be noted that there were a few anomalous cases that did not follow the trends observed such as the

- 0.5 mm (heat treat II) brass specimen with only seven grains through the thickness,

- 0.254 mm (325 $^{\circ}$C), 0.5 mm (575 $^{\circ}$C) and 1.588 mm (450 $^{\circ}$C) aluminum cases.

The reasons for these anomalies may include material deformation history that may not have been completed eliminated with the heat treatment done, such as in the case of the 0.254 mm (325 $^{\circ}$C) aluminum specimen with ten grains through the thickness. Other anomalies such as the one for the 0.5 mm brass (heat treat II) may have been due to specimen size effects. Those with less than one grain through the thickness, most probably were reflecting the fact that the grain orientation can be either favorable as is observed with the 1.588 mm (575 $^{\circ}$C) aluminum specimens or unfavorable as is the case with the 0.5 mm (575 $^{\circ}$C) aluminum specimens.

<u>Extrusion</u>

The accuracy of the models in predicting the peak force for a microextrusion process is governed by the manner in which the increased shear force is accounted for as the grain and specimen size change.

- ➢ The standard macroscale slab model assumes a shear force that is independent of grain and specimen size. This leads to under-predicting the extrusion force for microscale specimens by as much as 7%
- ➢ The modified slab model uses a shear force term that is a function of the grain size and die geometry. This improves the predictions for microscale cases for the two smallest dies to within 2.7%

Again due to specimen size effects, the peak force for 2.00/1.33 mm (heat treat II) case with nine grains through the thickness is more accurately predicted by the macroscale model.

<u>Finite Element Analysis</u>

The commercial FEA package that was used (MSC. Marc) in the modeling and simulation of the flanging process was found to capture increased scatter size effects with increasing grain size. It also over predicted the peak forces for microscale simulations as would be expected. These results show that it is possible to obtain rough estimates of size effects using commercially available

107

FEA software if appropriate plastic anisotropic constants that characterize the material microstructure are used.

FUTURE WORK

Possible future work includes the following investigations

1. Material property size effects using microscale tensile tests instead of trying to determine microscale material properties using specimens that have only one dimension in the microscale

2. Material property size effects using microcompressive tests so that any effects of changing strain hardening rates with strain especially when studying high strain processes like microextrusion

3. Possibility of measuring in situ strain across the specimen thickness during microbending tests using digital imaging correlation. This would help us to understand the distribution of strain in the sheet and how it responds to miniaturization of the specimen

4. High temperature microforming

5. FEA modeling including the effect of grain boundaries and grain shape

108

REFERENCES

1. In-Stat, "An Industry in Transition: 2006 MEMS Forecast", Product Number IN0603149ESCA, 2006.

2. Ehmann K.F., D. Bourell, M.L. Culpepper, T.R. Kurfess, M.Madou, K. Rajurkar, R.E DeVor, (2004), "International Assessment of Research and Development in Micromanufacturing: *Final Report*", *World Technology Evaluation Center*.

3. Kocks U.F., Tomé, C.N., Wenk, H.-R., (2000) "*Texture and anisotropy*: Preferred orientations in polycrystals and their effect on materials properties", Cambridge University Press, New York, ISBN -13 978-0-521-79420-6

4. Internal Precision http://www.internalprecision.com/ , Haywar, CA USA

5. Geißdörfer, S., Engel, U., Geiger, M., "FE-simulation of microforming processes applying a mesoscopic model", *International Journal of Machine Tools & Manufacture* 46 (2006), pp. 1222-1226

6. Armstrong R.W., "On Size Effects in Polycrystal Plasticity," *J. Mechanics & Physics of Solids* Vol. 9, 1961, pp. 196-199

7. Tiesler, Nicolas A., "Microforming – Size effects in friction and their influence on extrusion processes", *Wire* Vol. 52 Iss.1, 2002

8. Krishnan, N., Cao, J., Dohda, K., "Study of the size effect on friction conditions in microextrusion: Part 1 – Microextrusion experiments and analysis:, Accepted to *ASME Journal of Manufacturing Science and Engineering*, (August 2006)

9. Mori L., Krishnan N., Cao J., and Horacio Espinosa, "Study of the Size Effects and Friction Conditions in Micro-extrusion: Part II—Size effect in dynamic friction for brass-steel pairs", accepted to *ASME Journal of Manufacturing Science and Engineering*, 2007

109

10. Martin, G., Tsang S., "The plastic bending of beams considering die friction effects (Die friction effects on plane stress and plane strain in plastic bending of steel and titanium alloy beams)", *Asme, Transactions, Series B-Journal of Engineering for Industry.* Vol. 88, pp. 237-250. Aug. 1966

11. Raulea, L.V., Goijaerts, A.M., Govaert, L.E., Baaijens, F.P.T., "Size effects in the processing of thin metal sheets", *Journal of Materials Processing Technology* 115, 2001, pp44-48

12. Geiger, M., Kleiner, M., Eckstein, R., Tiesler, N., and Engel, U., "Microforming," *CIRP Ann.,* 50(2), 2001, pp. 445-462

13. Kals, R., Vollertsen, F., Geiger, M., "Scaling effects in sheet metal forming in": H.J.J. Kals, et al. (Eds) *Proceedings of the fourth International Conference on Sheet Metal,* Vol. II, Enschede, 1996, pp. 65-75

14. Cao, J., Krishnan, N., Wang, Z., Lu, H., Liu, W., Swanson, A., "Microforming: Experimental Investigation of Extrusion Process for micropins and its numerical simulation using RKEM", *Journal of Manufacturing Science and Engineering,* Vol. 126, 2004, pp 642-652

15. Parasiz, S.A., B.L., Kinsey, N. Krishnan, J. Cao, and M. Li, "Investigation of deformation size effects during Microextrusion", accepted *ASME J. Man. Sci. and Eng.* (2007)

16. Stölken, J.S., Evans, A.G., "A microbend test method for measuring the plasticity length scale", *Acta Mater.* Vol.46, No. 14, 1998, pp5109-5115

17. Geiger, M., Vollertsen, F., Kals, R., "Fundamentals of the manufacturing of sheet metal microparts", *Annals of the CIRP* vol. 45, 1, 1996, pp. 277-282

18. Chakrabarty, J., Lee, W.B., Chan, K.C., "An exact solution for the elastic/plastic bending of anisotropic sheet metal under conditions of plane strain", *International Journal of Mechanical Sciences* 43, 2001, pp. 1871-1880

110

19. Engel, U., Eckstein, R., "Microforming-from basic research to its realization", *Journal of Materials Processing Technology"*, 125-126, 2002, pp. 35-44

20. Eckstein, R., Engel, U., "Behavior of the grain structure in micro sheet metal working", Metal Forming 2000, Pietrzyk et al (eds), 2000 Balkema, Rotterdam, ISBN 9058091570, pp. 453-459

21. Diehl, A.; Engel, U.; Geiger, M., "Mechanical Properties and bending behaviour of metal foils", 4M 2006, 2nd International Conference on Multi-Material Micro Manufacture, 2006, Grenoble, pp. 297-300

22. Diehl, A.; Engel, U.; Geiger, M., "Investigation of the spring-back behaviour in metal foil forming", *Proceedings of the 24th IDDRG-conference*, Besancon, Frankreich, 2005

23. Kalpakjian S., Schmid S.R., (2006), *Manufacturing Engineering and Technology*, Pearson Prentice Hall, New Jersey, ISBN 0-13-148965-8 pp. 445

24. Wang, C., Kinzel, G., Altan, T., "Mathematical modeling of plane –strain bending of sheet and plate", *Journal of Materials Processing Technology*, 39, 1993, pp. 279-304

25. Lehrstuhl für Fertigungstechnologie (LFT), Friedrich-Alexander-Universitat, Erlangen-Nurnberg, Germany, 1993

26. Hansen, N., "The effect of grain size and strain on the tensile flow stress of Aluminium at room temperature", *Acta Metallurgica*, Vol. 25, 1977, pp. 863-869

27. Hatch, J.E., (Ed), *"Aluminum: Properties and physical metallurgy"*, American Society of Metals, Metals Park Ohio, 1984, ISBN 0-87170-176-6

28. Eckstein, R., "Scherschneiden und Biegen metallischer Kleinstteile – Materialeinfluss und Materialverhalten. *Dissertation, Universität Erlangen-*

111

Nürnberg. Bamberg: Meisenbach, [Geiger, M., Feldmann, K., Reihe Fertigungstechnik, Band 142], 2003, ISBN 3-87525-193-8

29. Key-to Metals, "Annealing of aluminum and aluminum alloys", http://www.key-to-metals.com/Article139.htm

30. Ludwik, P., "Engineering study of sheet bending", Verlag des Deutschen Polytechnischen Vereins, Böhmen, Technische Blätter Vol. 35, 1903, pp. 133-159

31. Hill, R., "The mathematical theory of plasticity", Oxford University Press, 1998, ISBN-10-0198503679

32. Hosford, W.F., Cadell, R.M., *Metal Forming Mechanics and Metallurgy*, 2nd ed. 1993, ISBN 0135885264

33. Budynas, R.G., *Advanced Strength and Applied Stress Analysis*, McGraw-Hill Book Company, Inc. 1977, pp. 239-240 ISBN 0-07-008828-4

34. Huang, Y., Gao, H., Nix, W.D., Hutchinson, J.W., "Mechanism-based strain gradient plasticity – II, Analysis", *Journal of the Mechanics and Physics of Solids* 48, 2000, pp. 22-128

35. Boyer, H.E., 1987, *"Atlas of stress-strain curves"*, ASM, ISBN 0-87170-240-1
36. Avitzur B., (1979), *Metal Forming: Processes and Analysis*, Robert Krieger Pub. Co., Inc., NY.

37. Bhupatiraju, M., M. & R., Greczanik, (2005), " ASM Handbook Vol. 14A Metalworking: Bulk Forming –Cold Extrusion", Ed. Semiatin, S.L. The Materials Inform. Soc., Materials Park, OH.

38. Sheppard, T., "Temperature changes occurring during extrusion of metals: Comparison of Bulk, Numerical and Integral Profile Predictions with Experimental Data", Materials Science and Technology, Vol. 15, April, 1999, pp. 459-463

112

39. Lange K., (1985), *Handbook of Metal Forming*, McGraw-Hill Inc.

40. Groover M.P., (1996), *Fundamentals of Modern Manufacturing: Materials, Processes and Systems*, Prentice Hall, New Jersey

41. Kinsey, B., Ehmann, K., Espinosa, H., Liu, W.K., Krishnan, N., and Li, M., (2005) "Microforming processes – preliminary investigations and developments", *Proceedings of 2005 DMII Grantees Conference*, MPM 0400267, Scottsdale, AZ, Jan. 3-6

42. Parasiz, S.A., Kinsey, B.L., Krishnan, N., Cao, J., "Characterization and investigation of deformation during microextrusion using x-ray texture analyses", Proceedings of the 2007 International Manufacturing Science And Engineering Conference MSEC2007, October 15-17, 2007, Atlanta, Georgia, USA

43. Altan T., S. Oh, H.L. Gegel, (1983), "Metal Forming: Fundamentals and Applications", *ASM,* ISBN 0-87170-167-7

44. Avitzur, B., (1983), *Handbook of Metal-Forming Processes*, John Wiley & Sons

45. Geiger, M., A. Meßner, U. Engel, R. Kals, F. Vollertsen, "Design of Micro-forming Processes – Fundamentals, Material Data, and Friction Behaviour", in: P. Standring (Ed.), Chipless 2000– Advancing Chipless Component Manufacture, *Proceedings of the Ninth International Cold Forging Congress,* Solhull, UK, FMJ Int. Publ. Ltd., Redhill 1995, pp. 155-164

46. Kocks, U.F., "The Relation Between Polycrystal Deformation and Single-Crystal deformation", *Metal. Trans.*, Vol. 1, 1970, pp. 1121-1143

47. Logan, D.L., *A First Course in the Finite Element Method*, Thomson, 4th ed. ISBN 0-534-55298-6, 2007

48. Choi, C., Kwon, J., Oh, K., H., and Lee, D., N., 1997, "Analysis of Deformation Texture Inhomogeneity and Stability Condition of Shear Components in f.c.c. Metals", *Acta Mater*, 45, 12, pp.5119-5128

49. MSC.Software Corporation, "User's Guide: Volume B: Element Library", www.mscsoftware.com

50. MSC.Software Corporation, "User's Guide: Volume A: Theory and User Information", www.mscsoftware.com

114

APPENDICES

115

APPENDIX A

MatLab code for the:

Curved wall model:

An example using the 0.127mm thickness, 575 °C heat treated case

```
thetac_01273=0;
thetac_01273(m)=thetac_01273;
theta2_01273=zeros(1,60);
theta1_01273=zeros(1,60);
S1_01273=zeros(1,60);
S1final_01273=zeros(1,60);
theta1f_01273=zeros(1,60);
thetas_01273=zeros(1,60);
C4_01273=zeros(1,60);
C5_01273=zeros(1,60);
C6_01273=zeros(1,60);
C7_01273=zeros(1,60);
C8_01273=zeros(1,60);
SE=zeros(1,60);
SEfinal_01273=zeros(1,60);
thetacf=zeros(1,60);
thetaR=zeros(1,60);
phRpp=zeros(1,60);
phREp=zeros(1,60);
phS1=zeros(1,60);
phSE=zeros(1,60);
u1=zeros(1,60);
u2=zeros(1,60);
```

```
Y1=zeros(1,60);

M_01273=zeros(1,60);

t=0.127; %mm
Rd=3*t; %mm
Ld=10*t; %mm
width=10*t; %mm
Rp=3*t; %mm
K_01273=145.1; %N/mm^2 Strength hardening coefficient
E=68900; %N/mm^2
sigmayield=24.8; %N/mm^2
F=2/sqrt(3); %Anisotropic index
n_01273=0.291; %Strain hardening exponent
v=0.33;   %Poisson's ratio
mu=0.2;  %Friction coefficient
I=width*t^3/12; %Second moment of area
Rpp=Rd+t/2;
C2_01273=2*width*K_01273*F^(n_01273+1)/(n_01273+2)*(t/2)^(n_01273+2);
C1_01273=3*t*(n_01273+2)*C2_01273/(4*(n_01273+3));
C3_01273=(2/3*(sigmayield*(1-v^2)/E)^2)*sigmayield*width;

%Elastic bending moment
ME=width*t^2*sigmayield/(6*(1-v^2)); %Equation 12
MA=(6*(I*K_01273*F^(n_01273+1))/(2+n_01273))*(t/(2*Rpp))^n_01273*(1+3/2*(
n_01273+2)/(n_01273+3)*(t/(2*Rpp)))*(1/t);  %Equation 24

j=1;
```

'The desired bending angle is given as theta2 radians: This provides the initial value of desired bending angle theta2 which enables the first estimate of S1 be calculated'

```
    m=1;

    depth_01273(m)=0;
    P_01273(m)=0;
  for thetawanted=0:0.05:1.5
    theta2_01273(m)=thetawanted;
    thetac_01273(m)=theta2_01273(m);
    theta1_01273(m)=theta2_01273(m);


    %Using simple straight tangent approach
    S1_01273(j)=(Ld/cos(theta2_01273(m)))-(Rp+Rd+t)*tan(theta2_01273(m));
%Equation 35
    S1final_01273(m)=S1_01273(j);
    theta1f_01273(m)=theta1_01273(m);
    thetas_01273(m)=MA*(1-v^2)*S1final_01273(m)/(2*E*I);
    C4_01273(m)=ME/(MA*S1final_01273(m));    %Equation 17
    C5_01273(m)=C4_01273(m)*ME*(1-v^2)/(E*I); %Equation 21
    C6_01273(m)=S1final_01273(m)/MA*C3_01273;
    C7_01273(m)=S1final_01273(m)*C2_01273/MA;
    C8_01273(m)=3*t*(n_01273+2)*C7_01273(m)/(4*(n_01273+3));

    %Elastic radius of curvature
    RE=E*I/(ME*(1-v^2));
    REp=RE+t/2;

    SE(j)=S1final_01273(m)-1/C4_01273(m);
```

118

```
SEfinal_01273(m)=SE(j);
theta1_01273(m+1)=theta2_01273(m)+thetas_01273(m); %Equation 23
theta1f_01273(m+1)=theta1_01273(m+1);


%The new Punch sheet contact angle thetac is given as
theta_01273(m+1)=theta1_01273(m)+2*C6_01273(m)*(REp-Rpp)-
n_01273/(n_01273+1)*C7_01273(m)*((1/Rpp)^(n_01273+1)-
(1/REp)^(n_01273+1))-(1+n_01273)/(2+n_01273)*C8_01273(m)*...
    ((1/Rpp)^(n_01273+2)-(1/REp)^(n_01273+2))-
C5_01273(m)/2*(S1final_01273(m)-SEfinal_01273(m))^2; %Equation 28
thetacf(m+1)=theta_01273(m+1);


S1_01273(j+1)=(Rp+Rd+t)*(theta1f_01273(m)-thetacf(m));
S1final_01273(m+1)=S1_01273(j+1);
C4_01273(m+1)=ME/(MA*S1final_01273(m+1));
SE(j+1)=S1final_01273(m+1)*(1-ME/MA);
SEfinal_01273(m+1)=SE(j+1);


count(m)=1;
while (S1_01273(j+1)-S1_01273(j))/S1_01273(j+1)>0.0005


thetas_01273(m+1)=MA*(1-v^2)*S1final_01273(m+1)/(2*E*I);
C4_01273(m+1)=ME/(MA*S1final_01273(m+1));    %Equation 17
C5_01273(m+1)=C4_01273(m+1)*ME*(1-v^2)/(E*I); %Equation 21
C6_01273(m+1)=S1final_01273(m+1)/MA*C3_01273;
C7_01273(m+1)=S1final_01273(m+1)*C2_01273/MA;
C8_01273(m+1)=3*t*(n_01273+2)*C7_01273(m+1)/(4*(n_01273+3));


%Elastic radius of curvature
RE=E*I/(ME*(1-v^2));
```

119

```
REp=RE+t/2;

theta1_01273(m+2)=theta2_01273(m)+thetas_01273(m+1); %Equation
23
theta1f_01273(m+2)=theta1_01273(m+2);

%The new Punch sheet contact angle thetac is given as
theta_01273(m+2)=theta1_01273(m+1)+2*C6_01273(m+1)*(REp-Rpp)-
n_01273/(n_01273+1)*C7_01273(m+1)*((1/Rpp)^(n_01273+1)-
(1/REp)^(n_01273+1))-(1+n_01273)/(2+n_01273)*C8_01273(m)*...
((1/Rpp)^(n_01273+2)-(1/REp)^(n_01273+2))-
C5_01273(m+1)/2*(S1final_01273(m+1)-SEfinal_01273(m+1))^2;
%Equation 28
thetacf(m+2)=theta_01273(m+2);
S1_01273(j+2)=(Rp+Rd+t)*(theta1f_01273(m+2)-thetacf(m+2));

SE(j+2)=S1_01273(j+2)*(1-ME/MA);
SEfinal_01273(m+1)=SE(j+2);
count(m)=count(m)+1;
S1final_01273(m+1)=S1_01273(j+2);

j=j+1;
end


thetaR(m)=thetacf(m)+n_01273/(n_01273+1)*C7_01273(m)*((1/Rpp)^(1+n_
01273)-
(1/REp)^(1+n_01273))+(1+n_01273)/(2+n_01273)*C8_01273(m)*((1/Rpp)^(
2+n_01273)-(1/REp)^(2+n_01273));
```

120

```
phRpp(m)=sin(thetaR(m))*(n_01273*C7_01273(m)*(1/Rpp)^(1+n_01273)+(n
_01273+1)*C8_01273(m)*(1/Rpp)^(2+n_01273));


phREp(m)=sin(thetaR(m))*(n_01273*C7_01273(m)*(1/REp)^(1+n_01273)+(n
_01273+1)*C8_01273(m)*(1/REp)^(2+n_01273));


phS1(m)=sin(thetaR(m))*(n_01273*C7_01273(m)*(1/(abs(S1final_01273(m))
))^(1+n_01273)+(n_01273+1)*C8_01273(m)*(1/(abs(S1final_01273(m))))^(2
+n_01273));


phSE(m)=sin(thetaR(m))*(n_01273*C7_01273(m)*(1/abs(SEfinal_01273(m))
)^(1+n_01273)+(n_01273+1)*C8_01273(m)*(1/abs(SEfinal_01273(m)))^(2+n
_01273));


   N=7000;
  deltaR(m)=(REp-Rpp)/N;
  deltaS(m)=(S1final_01273(m)-SEfinal_01273(m))/N;
  for k=1:N
     R2k_1(m)=Rpp+(2*k-1)*deltaR(m);
     R2k(m)=Rpp+2*k*deltaR(m);
     S2k_1(m)=SEfinal_01273(m)+(2*k-1)*deltaS(m);
     S2k(m)=SEfinal_01273(m)+2*k*deltaS(m);


  end


  TR2k(m)=0;
  TR2k_1(m)=0;
  TS2k(m)=0;
```

```
        TS2k_1(m)=0;

for k=1:N-2
        TR2k1(m)=sin(thetaR(m))*(n_01273*C7_01273(m)*(1/R2k(m))^(1+n_0127
        3)+(n_01273+1)*C8_01273(m)*(1/R2k(m))^(2+n_01273));

        TS2k1(m)=sin(thetaR(m))*(n_01273*C7_01273(m)*(1/abs(S2k(m)))^(1+n_
        01273)+(n_01273+1)*C8_01273(m)*(1/abs(S2k(m)))^(2+n_01273));
        TR2k(m)=TR2k(m)+TR2k1(m);
        TS2k(m)=TS2k(m)+TS2k1(m);
End

for k=1:N-1
        TR2k_11(m)=(sin(thetaR(m))*(n_01273*C7_01273(m)*(1/R2k_1(m))^(1+n
        _01273)+(n_01273+1)*C8_01273(m)*(1/R2k_1(m))^(2+n_01273)));

        TS2k_11(m)=(sin(thetaR(m))*(n_01273*C7_01273(m)*(1/abs(S2k_1(m)))^
        (1+n_01273)+(n_01273+1)*C8_01273(m)*(1/abs(S2k_1(m)))^(2+n_01273
        )));
         TR2k_1(m)=TR2k_1(m)+TR2k_11(m);
         TS2k_1(m)=TS2k_1(m)+TS2k_11(m);
        End

u1(m)=deltaR(m)/3*((phRpp(m)+phREp(m))+2*TR2k(m)+4*TR2k_1(m));
u2(m)=deltaS(m)/3*((phSE(m)+phS1(m))+2*TS2k(m)+4*TS2k_1(m));
Y1(m)=u1(m)+u2(m);
depth_01273(m+1)=Y1(m)+(Rd-(Rd+t/2)*cos(thetacf(m)))+(Rp-
        (Rp+t/2)*cos(theta1f_01273(m)))+t;
```

```
M_01273(m+1)=(K_01273*F^(n_01273+1)*width*t^2)/(2+n_01273)*(t/(2*Rpp))^n
        _01273*(1+1.5*(n_01273+2)/(n_01273+3)*t/(2*Rpp));
Length(m+1)=Ld*((1-(2*Rd*sin(theta1f_01273(m)))/Ld)+(tan(theta1f_01273(m))-
mu)...
        /(1+mu*(tan(theta1f_01273(m))))*((depth_01273(m+1)/Ld)-(Rd/Ld)*(1-
        cos(theta1f_01273(m)))));
P_01273(m+1)=M_01273(m+1)/(Length(m+1));
PC =K_01273*sigmayield*width*t^2/Ld ; % Peak Force model equation for the
bending force


    m=m+1;
end


% Experimental data is loaded and then plotted
N01273=xlsread('C:\Documents and Settings\Richard\Desktop\Bending
Experiment\ Data\ 0.127mm\575\force_disp_0127_575','Sheet1');


plotE_01273(:,1)=N01273(:,1);
plotE_01273(:,2)=N01273(:,2);
plot_01273(:,1)=depth_01273;
plot_01273(:,2)=P_01273;


figure(1)
plot(N01273(:,1),N01273(:,2),plot_01273(:,1),plot_01273(:,2))
xlabel('depth mm'),ylabel('Bending Force N')
title('0.127 mm Thickness Experimental vs CW Predicted
Force','FontWeight','bold')
legend('Exp. Heat treat 3','Pred. Heat treat3')
```

123

Straight Wall Model

0.127 mm Thickness 575 Heat Treat Samples

```
clf reset
disp('Assuming isotropy and plane strain.')


('Obtain value of n -work hardening exponent from tensile test data')
('Read the displacement data from the given files')
('Calculate the value of the force P using the expression above.')
t=0.127 % mm
width_0127=10; % mm
F=2/sqrt(3);
K_01273=145.1; %units are N/mm^2
B=Rg^2+(2*Rd*Rg); %units are mm^2
L=Rd+Rg;  %units are mm
sigmayield_01273=24.8; % MPa
E_0127=68900; % GPa
v=0.33;
n_01273=0.291;
%Applying boundary condition at the very start of the process

j=1;
P_01273(j)=0;
depth_01273(j)=0;
j=j+1;
for y1=0.01:.01:8*t
    depth_01273(j)=y1;
```

```
C(1)=Ld^2+depth_01273(j)^2-2*depth_01273(j)*Rd+Rd^2;
C(2)=-2*Ld*Rd^2;
C(3)=2*depth_01273(j)*Rd^3-Rd^2*depth_01273(j)^2;
x_roots=roots(C);
x_roots1_01273(j,1)=real(x_roots(1,1));
x_roots1_01273(j,2)=real(x_roots(2,1));


    %picks out correct root so it is less than or equal to the die opening length
    and stores it as the correct value of x2

if j<146
    x_01273(j)=x_roots1_01273(j,2);
else
    x_01273(j)=x_roots1_01273(j,1);
end
y_01273(j)=(Rd-sqrt(Rd^2-x_01273(j)^2));

%Calculates the wrap angle
x2(j)=Ld-x_01273(j);
theta(j)=atan((depth_01273(j)-y_01273(j))/x2(j));

Length(j)=(n_01273+2)*Ld*((1-(Rd*sin(theta(j)))/Ld)+ (tan(theta(j))-
            mu)/(1+mu*tan(theta(j)))*((depth_01273(j) /Ld)-(Rd/Ld)*(1-
            cos(theta(j)))));

    P_01273(j)=(K_01273*F^(n_01273+1)*width_0127*t^2)*(t/(2*Rpp))^n_0127
            3*(1+(3*(n_01273+2)*t/(2*(n_01273+3)*2*Rpp)))/(2*Length(j))
            ;% Wang model

j=j+1;
```

125

```
end

N01273=xlsread('C:\Documents and Settings\Richard\Desktop\ Bending
Experiment\Data\0.127mm\575\force_disp_0127_575');
plot_01273(:,1)=depth_01273(j-1);
plot_01273(:,2)=P_01273(j-1);




%Comparison of plots of 0.127 mm Thickness experimental versus Predicted
Results

figure(1)
plot(N01273(:,1),N01273(:,2),depth_01273,P_01273)
xlabel ('depth mm'), ylabel('Bending Force N')
title('0.127 mm Thickness Experimental vs SW Predicted
Force','FontWeight','bold')
legend('Experimental 575 heat','Pred 575 Heat treat')

xlswrite('C:\Documents and Settings\Richard\Desktop\Bending
Experiment\Data\Comparisons\plots_01',plot_0127,'sheet1','E4');

% 'Experimental Heat treat3 peak force = '
PmaxE_01273 = max(N01273(:,2)) %'Newtons'

% 'Predicted Heat treat2 peak force = '
PmaxP_01273 = max(P_01273) %'Newtons'
```

Curved Wall Modified Moment Model:

```
clear reset
clear
```

126

%0.127 mm Thickness, 575 Heat treat Samples

t=0.127 % mm

width =10*t; % mm

Rd=3*t;

Rp=3*t;

Ld=10*t;

K_013=145.1; %N/mm^2 Strength hardening coefficient

E=68900; %N/mm^2

sigmayield_013=24.8; %N/mm^2

F=2/sqrt(3); %Anisotropic index

n_013=0.291; %Strain hardening exponent

v=0.33;   %Poisson's ratio

mu=0.2; %Friction coefficient

I=width*t^3/12; %Second moment of area

Rpp=Rp+t/2;

C2=2*width*K_013*F^(n_013+1)/(n_013+2)*(t/2)^(n_013+2);

C1=3*t*(n_013+2)*C2/(4*(n_013+3));

C3=(2/3*(sigmayield_013*(1-v^2)/E)^2)*sigmayield_013*width; %Elastic bending moment

ME=width*t^2*sigmayield_013/(6*(1-v^2)); %Equation 12

MA=(6*(I*K_013*F^(n_013+1))/(2+n_013))*(t/(2*Rpp))^n_013*(1+3/2*(n_013+2)/(n_013+3)*(t/(2*Rpp)))*(1/t); %Equation 24

j=1;

thetac_013=0;

127

'The desired bending angle is given as theta2 radians: This provides the initial value of desired bending angle theta2 which enables the first estimate of S1 be calculated'

```
m=1;
thetac_013(m)=thetac_013;
depth(m)=0;
P(m)=0;
m=m+1;
for thetawanted=0.01:0.01:1.5
    theta2(m)=thetawanted;
    thetac_013(m)=theta2(m);
    theta1(m)=theta2(m);
    %Using simple straight tangent approach
    S1(j)=(Ld/cos(theta2(m)))-(Rp+Rd+t)*tan(theta2(m));   %Equation 35
    S1final_013(m)=S1(j);
    theta1f_013(m)=theta1(m);
    thetacf_013(m)=thetac_013(m);


    % thetas(m)=(3*K_013*F^(n_013+1))/(2+n_013)*(1-
    v^2)/E*(t/(2*Rpp))^n_013*(1+3/2*(n_013+2)/(n_013+3)*t/(2*Rpp))*S1(j
    )/t;          %Equation 24
    thetas(m)=MA*(1-v^2)*S1final_013(m)/(2*E*I);
    C4(m)=ME/(MA*S1final_013(m));   %Equation 17
    C5(m)=C4(m)*ME*(1-v^2)/(E*I); %Equation 21
    C6(m)=S1final_013(m)/MA*C3;
    C7(m)=S1final_013(m)*C2/MA;
    C8(m)=3*t*(n_013+2)*C7(m)/(4*(n_013+3));
    %Elastic radius of curvature
    RE=E*I/(ME*(1-v^2));
    REp=RE+t/2;
```

128

```
SE3(j)=S1final_013(m)*(1-ME/MA);
SEfinal_013(m)=SE3(j);
theta1(m+1)=theta2(m)+thetas(m); %Equation 23
theta1f_013(m+1)=theta1(m+1);


%The new Punch sheet contact angle thetac_013 is given as
      thetac_013(m+1)=theta1(m+1)+2*C6(m)*(REp-Rpp)-
      n_013/(n_013+1)*C7(m)*((1/Rpp)^(n_013+1)-(1/REp)^(n_013+1))-
      (1+n_013)/(2+n_013)*C8(m)*...
((1/Rpp)^(n_013+2)-(1/REp)^(n_013+2))-C5(m)/2* (S1final_013(m)-
      SEfinal_013(m))^2; %Equation 28
thetacf_013(m+1)=thetac_013(m+1);


    % SA(j+1)=log(abs(cos(thetacf_013(m+1))))-
    log(abs(cos(theta1f_013(m+1))));
    % SAE(j+1)=thetacf_013(m+1)-theta1f_013(m+1);
S1(j+1)=(Rp+Rd+t)*(thetacf_013(m+1)- theta1f_013(m+1));
S1final_013(m+1)=S1(j+1);
C4(m+1)=ME/(MA*S1final_013(m+1));
SE3(j+1)=S1final_013(m+1)*(1-ME/MA);
SEfinal_013(m+1)=SE3(j+1);


count(m)=1;
while (S1(j+1)-S1(j))/S1(j+1)>0.0001


thetas(m+1)=MA*(1-v^2)*S1final_013(m+1)/(2*E*I);
C4(m+1)=ME/(MA*S1final_013(m+1));    %Equation 17
C5(m+1)=C4(m+1)*ME*(1-v^2)/(E*I); %Equation 21
C6(m+1)=S1final_013(m+1)/MA*C3;
```

129

```
C7(m+1)=S1final_013(m+1)*C2/MA;
C8(m+1)=3*t*(n_013+2)*C7(m+1)/(4*(n_013+3));
%Elastic radius of curvature
RE=E*I/(ME*(1-v^2));
REp=RE+t/2;


theta1(m+2)=theta2(m)+thetas(m+1); %Equation 23
theta1f_013(m+2)=theta1(m+2);
%The new Punch sheet contact angle thetac_013 is
thetac_013(m+2)=theta1(m+2)+2*C6(m+1)*(REp-Rpp)-
    n_013/(n_013+1)*C7(m+1)*((1/Rpp)^ (n_013+1)-(1/REp)^(n_013+1))-
    C8(m)*((1/Rpp)^(n_013+2)-(1/REp)^(n_013+2))-
    C5(m+1)/2*(S1final_013(m+1)-SEfinal_013(m+1))^2; %Equation 28
thetacf_013(m+2)=thetac_013(m+2);


SE3(j+2)=S1(j+2)*(1-ME/MA);
SEfinal_013(m+2)=SE3(j+2);
count(m)=count(m)+1;
S1final_013(m+2)=S1(j+2);


j=j+1;
end
% Calculates the curvature for the elasto-plastic region using the NR method
h=1;
i=1;
R_013total=0;
for S=0:S1final_013(m)
  for S=0:SEfinal_013(m)
    R_013(h)=2;
```

```
f_R013(h)=real(S1final_013(m)-C6(m)*R_013(h)^n_013-
        C7(m)*R_013(h)^(-n_013)-C8(m)*R_013(h)^-(n_013+1)-
        S);
fp_R013(h)=real(-C6(m)*R_013(h)^(n_013-
        1)+n_013*C7(m)*R_013(h)^(-n_013-
        1)+(n_013+1)*C8(m)*R_013(h)^-(n_013+2));
R_013(h+1)=R_013(h)-f_R013(h)/fp_R013(h);
h=2;
f_R013(h)=real(S1final_013(m)-C6(m)*R_013(h)^n_013-
        C7(m)*R_013(h)^(-n_013)-C8(m)*R_013(h)^-(n_013+1)-
        S);
fp_R013(h)=real(-C6(m)*R_013(h)^(n_013-1)+
        n_013*C7(m)*R_013(h)^(-n_013-1)+(n_013+1)
        *C8(m)*R_013(h)^-(n_013+2));
R_013(h+1)=R_013(h)-f_R013(h)/fp_R013(h);
h=3;
while R_013(h)-R_013(h-1)>0.01
f_R013(h)=real(S1final_013(m)-C6(m)*R_013(h)^n_013-
        C7(m)*R_013(h)^(-n_013)-C8(m)*R_013(h)^-(n_013+1)-
        S);
fp_R013(h)=real(-C6(m)*R_013(h)^(n_013-1)+
        n_013*C7(m)*R_013(h)^(-n_013-1)+(n_013+1)
        *C8(m)*R_013(h)^-(n_013+2));
R_013(h+1)=R_013(h)-f_R013(h)/fp_R013(h);
h=h+1;
end
R_013total=R_013total+R_013(h);
i=i+1;
end
R_013av=R_013total/i;
```

131

```
ka_013ep=1/R_013av;

% Curvature of the elastic plastic region
i=1;
ka_013eav=0;
ka_013etotal=0;
for S=SEfinal_013(m):0.01:S1final_013(m)
        ka_013e(m)=C5(m)*(S1final_013(m)-S);
        ka_013etotal=ka_013etotal+ka_013e(m);
        i=i+1;
    end
    ka_013eav=ka_013etotal/i;
end
ka_013p=1/Rd;


  ka_013Total(m)=1/Rd;
ka_013Total(m)=ka_013p+ka_013eav+ka_013ep;


ka_013Total(m)=(Rd*sin(theta1f_013(m+1))/Ld)*ka_013p+(SEfinal_013(m+1)*co
s(theta1f_013(m+1))/Ld)*ka_013eav+(Ld-
SEfinal_013(m+1)*cos(theta1f_013(m+1))-Rd*theta1f_013(m+1)) *ka_013ep;


        thetaR(m)=thetacf_013(m)+n_013/(n_013+1)*C7(m)*((1/Rpp)^(1+n_013)-
(1/REp)^(1+n_013))+(1+n_013)/(2+n_013)/(n_013+2)
*C8(m)*((1/Rpp)^(2+n_013)-(1/REp)^(2+n_013));


phRpp(m)=sin(thetaR(m))*(n_013*C7(m)*(1/Rpp)^(1+n_013)+(n_013+1)/(n_013
+2)*C8(m)*(1/Rpp)^(2+n_013));
```

132

```
phREp(m)=sin(thetaR(m))*(n_013*C7(m)*(1/REp)^(1+n_013)+(n_013+1)/(n_013
+2)*C8(m)*(1/REp)^(2+n_013));


phS1(m)=sin(thetaR(m))*(n_013*C7(m)*(1/(abs(S1final_013(m))))^(1+n_013)+(n
_013+1)/(n_013+2)*C8(m)*(1/(abs(S1final_013(m))))^(2+n_013));


phSE3(m)=sin(thetaR(m))*(n_013*C7(m)*(1/abs(SEfinal_013(m)))^(1+n_013)+(n
_013+1)/(n_013+2)*C8(m)*(1/abs(SEfinal_013(m)))^(2+n_013));


    N=5000;
    deltaR(m)=(REp-Rpp)/N;
    deltaS(m)=(S1final_013(m)-SEfinal_013(m))/N;
    for k=1:N
       R2k_1(m)=Rpp+(2*k-1)*deltaR(m);
       R2k(m)=Rpp+2*k*deltaR(m);
       S2k_1(m)=SEfinal_013(m)+(2*k-1)*deltaS(m);
       S2k(m)=SEfinal_013(m)+2*k*deltaS(m);


    end


    TR2k(m)=0;
    TR2k_1(m)=0;
    TS2k(m)=0;
    TS2k_1(m)=0;
    for k=1:N-2


TR2k1(m)=sin(thetaR(m))*(n_013*C7(m)*(1/R2k(m))^(1+n_013)+(n_013+1)/(n_0
13+2)*C8(m)*(1/R2k(m))^(2+n_013));
```

133

```
TS2k1(m)=sin(thetaR(m))*(n_013*C7(m)*(1/abs(S2k(m)))^(1+n_013)+(n_013+1)/
(n_013+2)*C8(m)*(1/abs(S2k(m)))^(2+n_013));
        TR2k(m)=TR2k(m)+TR2k1(m);
        TS2k(m)=TS2k(m)+TS2k1(m);
    end
    for k=1:N-1

            TR2k_11(m)=(sin(thetaR(m))*(n_013*C7(m)*(1/R2k_1(m))^(
            1+n_013)+(n_013+1)/(n_013+2)*C8(m)*(1/R2k_1(m))^(2+n
            _013)));

            TS2k_11(m)=(sin(thetaR(m))*(n_013*C7(m)*(1/abs(S2k_1(
            m)))^(1+n_013)+(n_013+1)/(n_013+2)*C8(m)*(1/abs(S2k_1
            (m)))^(2+n_013)));
        TR2k_1(m)=TR2k_1(m)+TR2k_11(m);
        TS2k_1(m)=TS2k_1(m)+TS2k_11(m);
    end


u1_013(m)=deltaR(m)/3*((phRpp(m)+phREp(m))+2*TR2k(m)+4*TR2k_1(m));


u2_013(m)=deltaS(m)/3*((phSE3(m)+phS1(m))+2*TS2k(m)+4*TS2k_1(m));
Y1_013(m)=abs(u1_013(m))+u2_013(m);
depth_013(m)=Y1_013(m)+(Rd-(Rd+t/2)*cos(thetacf_013(m))) +(Rp-
(Rp+t/2)*cos(theta1f_013(m)))+t;
        M(m)=(K_013*width*ka_013Total(m)^n_013*(t/2)^(n_013+2));
        Length(m)=Ld*((1-(Rd*sin(theta1f_013(m)))/Ld) +(tan(theta1f_013(m))-
mu)/(1+mu*(tan(theta1f_013(m)))) *((depth_013(m)/Ld)-(Rd/Ld)*(1-
cos(theta1f_013(m))))));
        P_013(m)=2*(2/sqrt(3))^(n_013+1)*M(m)/((n_013+2)*Length(m));
```

134

```
m=m+1;

end

disp('Experimental data is loaded and then plotted ')
N13=xlsread('C:\Documents and Settings\Richard\Desktop\ Bending
Experiment\Data\0.127mm\575\force_disp_0127_575');

plot_013(:,1)=depth_013 ;
plot_013(:,2)=P_013;
plotE3(:,1)=N13(:,1);
plotE3(:,2)=N13(:,2);
```

Straight Wall Modified Moment Model

```
0.127 mm 575 degree Heat treat Samples
n_013=0.291;
K_013=145.1; %units are N/mm^2
sigmayield_013=24.8; % MPa
E_01=68900; % GPa
v=0.33;
width_01=10*t;

%Applying boundary condition at the very start of the process

j=1;
x1=0;
P_013(j)=0;
depth_013(j)=0;
j=j+1;

% Calculating the depth of punch, moment arm length and the punch force for
increasing bend angles

for y1=0.01:.01:8*t
    depth_013(j)=y1;
    C_013(1)=Ld^2+depth_013(j)^2-2*depth_013(j)*Rd+Rd^2;
    C_013(2)=-2*Ld*Rd^2;
```

135

```
C_013(3)=2*depth_013(j)*Rd^3-Rd^2*depth_013(j)^2;
x_roots_013=roots(C_013);
x_roots1_013(j,1)=x_roots_013(1,1);
x_roots1_013(j,2)=x_roots_013(2,1);

%picks out correct root so it is less than or equal to Ld and stores it as the
correct value of x2

if x_roots_013(2,1)<=0 || j>38.1
    x12(j)=x_roots_013(1,1);
else
    x12(j)=x_roots_013(2,1);
end
y12(j)=sqrt(Rd^2-x12(j)^2)-Rd;

%Calculates the wrap angle
x2_013(j)=Ld-x12(j);
theta_013(j)=asin(x12(j)/Rd);

m=1;
for xp=0:0.01:x12(j)
    x1a(j,m)=xp;
    y1a(j,m)=sqrt(Rd^2-x1a(j,m)^2)-Rd;
    m=m+1;
end

i=1;
for xp2=x12(j)+0.01:0.01:Ld
    x2b(j,i)=xp2;
    y2b(j,i)=y12(j)-(x2b(j,i)-x12(j))*tan(theta_013(j));

    i=i+1;
end




xa_013=x1a';
xb_013=x2b';
ya_013=y1a';
yb_013=y2b';
n=1;
for i=1:size(xa_013(:,j))
    x_013(i,j)=xa_013(i,j);
    y_013(i,j)=ya_013(i,j);
    n=n+1;
```

136

```matlab
end
n=n-1;
for i=1:size(xb_013(:,j))
    x_013(i+n,j)=xb_013(i,j);
    y_013(i+n,j)=yb_013(i,j);
end


funct1=polyfit(x_013,y_013,2);
    curve(j)=funct1(1)*x_013(j)^2+funct1(2)*x_013(j)+funct1(3);
    curvediff1(j)=2*funct1(1)*x_013(j)+funct1(2);
    curvediff2(j)=2*funct1(1);
    k1_013(j)=-curvediff2(j)/(1+(curvediff1(j))^2)^1.5;
    if k1_013(j)<1/Rd
      k_013(j)=-curvediff2(j)/(1+(curvediff1(j))^2)^1.5;
    else
      k_013(j)=1/Rd;
    end
    k_013(j)=1/Rd;
Length(j)=Ld*((1-(Rd*sin(theta_013(j)))/Ld)+ (tan(theta_013(j))-
        mu)/(1+mu*tan(theta_013(j)))* ((depth_013(j)/Ld)-(Rd/Ld)*(1-
        cos(theta_013(j))))));
P_013(j)=4*(2/sqrt(3))^(n_013+1)*width_01*K_013*(k_013(j))^n_013*(t/2)^(n_01
        3+2)/((2+n_013)*Length(j));


        j=j+1;
end


N013=xlsread('C:\Documents and Settings\Richard\Desktop\Bending
Experiment\Data\0.127mm\ 575\force_disp_0127_575');
plot_013(:,1)=depth_013 ;
plot_013(:,2)=P_013;


figure(1)
plot(N013(:,1),N013(:,2),depth_013,P_013)
    xlabel('depth mm'), ylabel('Bending Force N')
title('0.127 mm Thickness Experimental vs SWMM Predicted Force Results')
legend('Exp 575 heat treat','Pred 575 Heat treat')

% The peak forces are given as follows:
PmaxE_013 = max(N013(:,2)) % Experimental Heat treat3 peak force in Newtons
PmaxP_013 = max(P_013) %Predicted Heat treat3 peak force in Newtons
experimental_peak=[PmaxE_013];
Predict3=[PmaxP_013];
```

xlswrite('C:\Documents and Settings\Richard\Desktop\Bending
Experiment\Data\Comparisons\Bend_Force_AI',Predict3,'sheet1','K2');

<u>Labview Program</u>

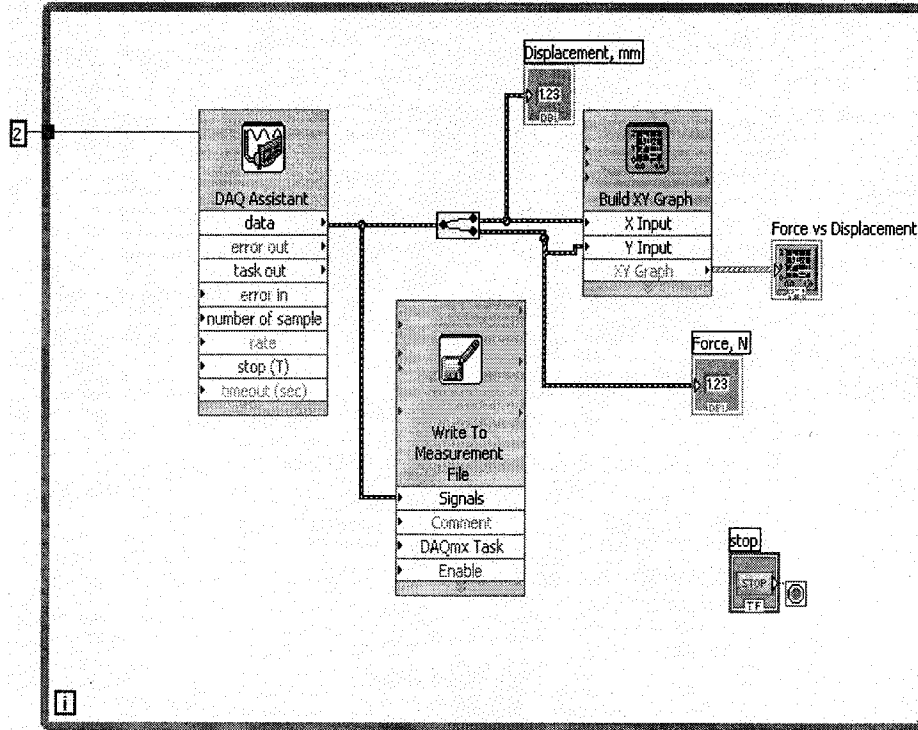Figure A50 shows the block diagram of the data acquisition program (Bender.vi)
used.

Figure A50 – Bender.vi – used for all bending tests

<u>Bender.vi parameters – DAQ Assistant:</u>
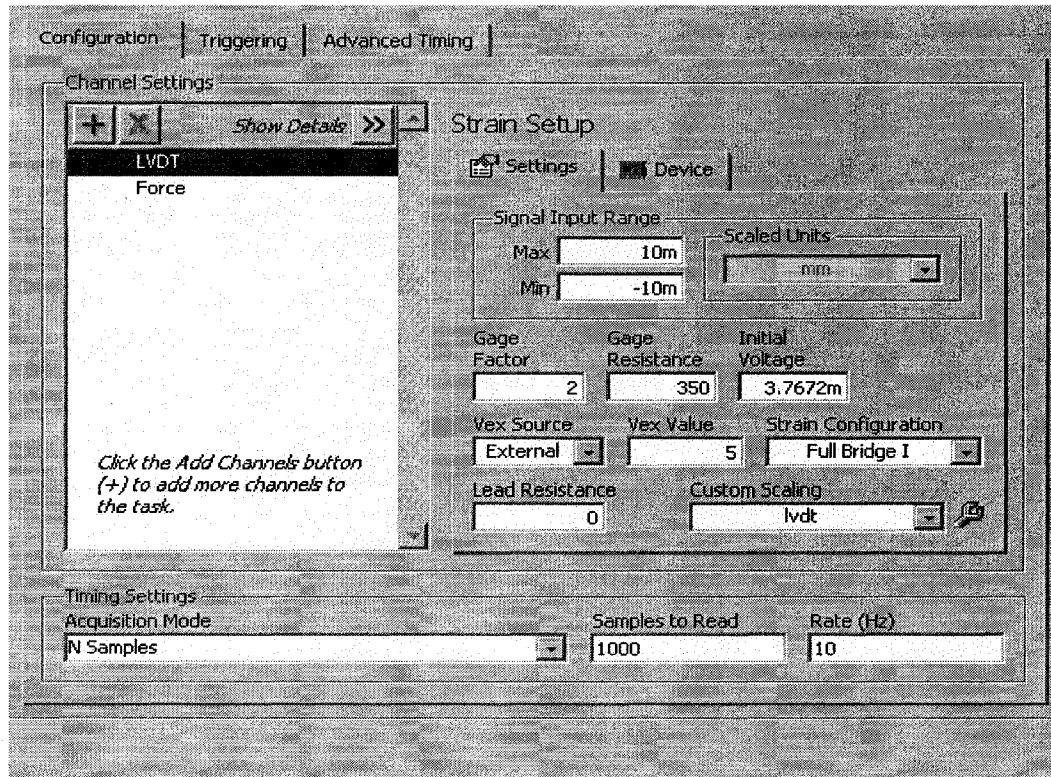These are input by clicking on the appropriate tab as shown in Figure A51.

138

Figure A51 – DAQ Assistant Parameters

The settings mentioned below were applied for LVDT and Force.

Power supply:

The National Instrument 9237 module does not output enough current to power the load cell and the LVDT owing to its 150mW limit (see NI9237 manual). Thus a precision external source of power was used for the experiments, using 10V for the LVDT and the 25lbs and 1000lbs load cell. 5V was used while using the 1000gm load cell in accordance to the manufacturer's specifications.

      Vex Source – External, 10V – 1.5-0.5mm
      Vex Source – External, 5V – 0.127 & 0.25mm

For this purpose, a Sorensen Laboratory DC Power Supply, LM 18-10 was used, with power being input to the NI 9237 unit.

Custom scaling:

Clicking on the wrench like object on its side in Figure A51 opens the edit box shown in Figure A52. The linear scale option was used This was completed for the LVDT and Force transducer using the slope values as explained in the main part of the thesis.

139

Lab view reads data as strain, which had to be converted to units of displacement or force for the LVDT and the load cell respectively.
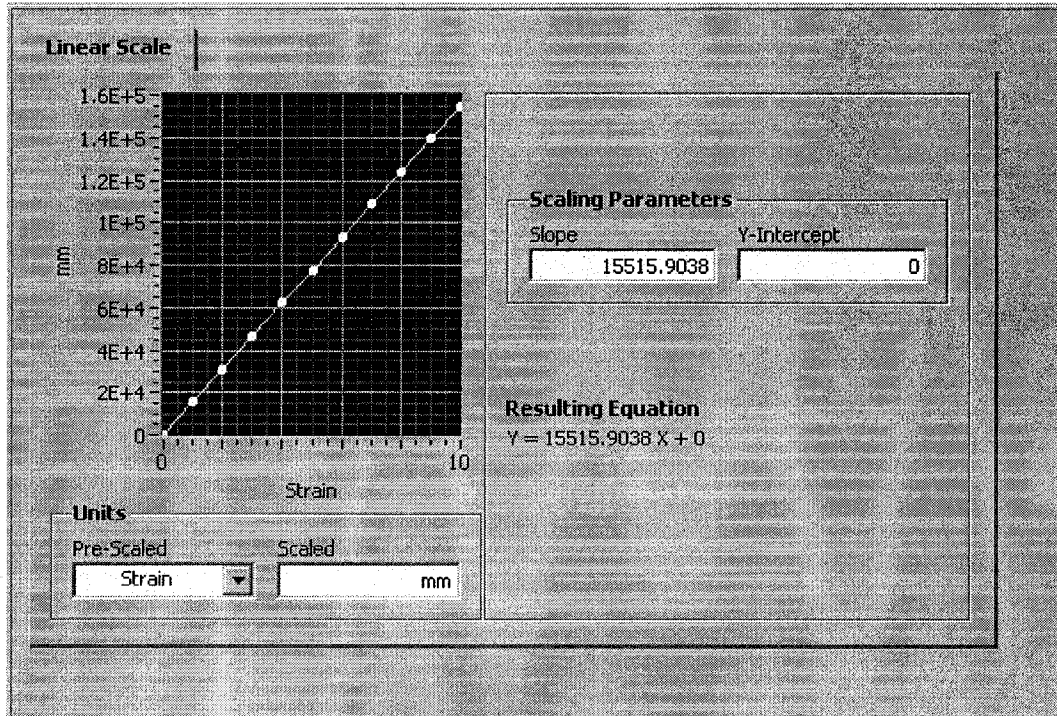

Figure A52 Strain/Force relation factor (slope)

The manufacturer's calibration certificate was used for calculating the factor ('Slope' in Figure A52) shown in **Table A10**.

Table A10 Input (strain)/output unit relation factor (slope)

Device	Slope(using certificate)
LVDT	15515.9038
Load cell – 1000gms	18876.275
Load cell – 25lbs	99320.145
Load cell – 1000lbs	4567584.839

Timing settings:
    Application Mode – N Samples
    Samples to read – 1000.
    These were chosen so that a complete force-displacement curve could be obtained. After taking 1000 samples, the program would stop automatically.

140

Sampling frequency of 10Hz was used to ensure a linear frequency response for the LVDT.

Strain configuration: Full Bridge I (for foil type sensor)
Gauge resistance: From calibration data. Table A11 shows the values for the LVDT and the load cells:

Table A11 Gauge resistances

Device	Gauge resistance(Ohms)
LVDT	350
Load Cell – 1000lbs	353
Load cell – 25lbs	352
Load cell – 1000gms	356

Gauge factor: 2 (for foil type of sensor)

Strain Calibration:
Strain Calibration was carried out once before a set of samples of same thickness were tested, to ensure the force and displacement were set to zero. The steps followed in this calibration are outlined in Figure A53 to Figure A55
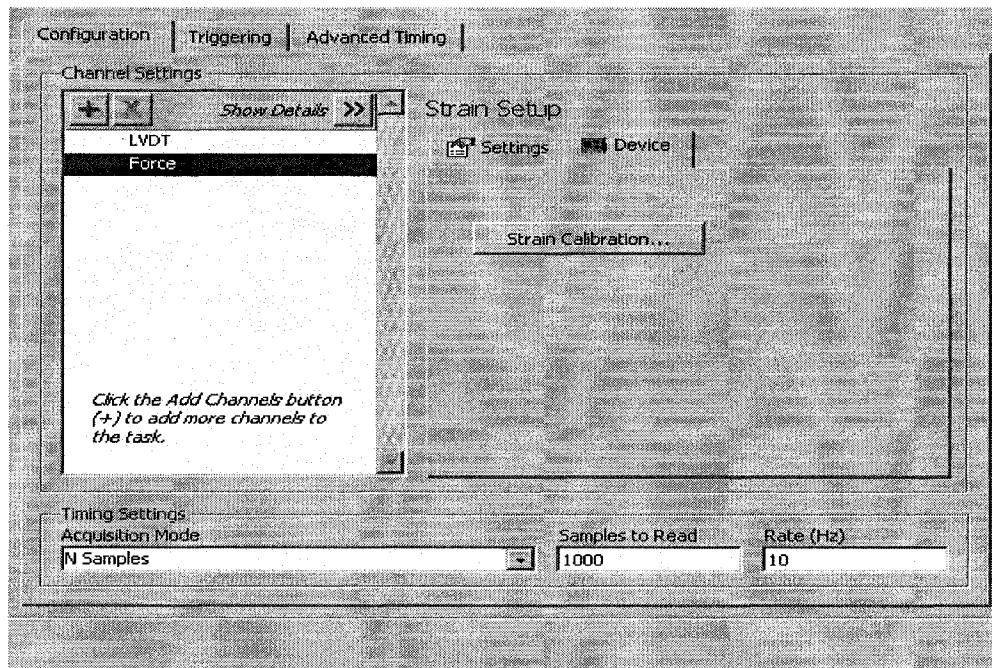

Figure A53 Strain Calibration before running tests

141

Steps in Strain Calibration :

1. Ensure the device is switched on and the punch, dies have been loaded and is ready for testing and the LabView program (Bender.vi) is running.
2. Click 'Device' tab in DAQ Assistant
3. Click 'Strain Calibration'. The window shown in Figure A54 appears.
4. Check 'Enable Offset Nulling'.
5. Click 'Next'. The window shown in Figure A55 appears.
6. Click 'Calibrate'. An error message is displayed if 'Signal Input Range' in Figure A51 is incorrect. Replace the values with those shown in the error message.
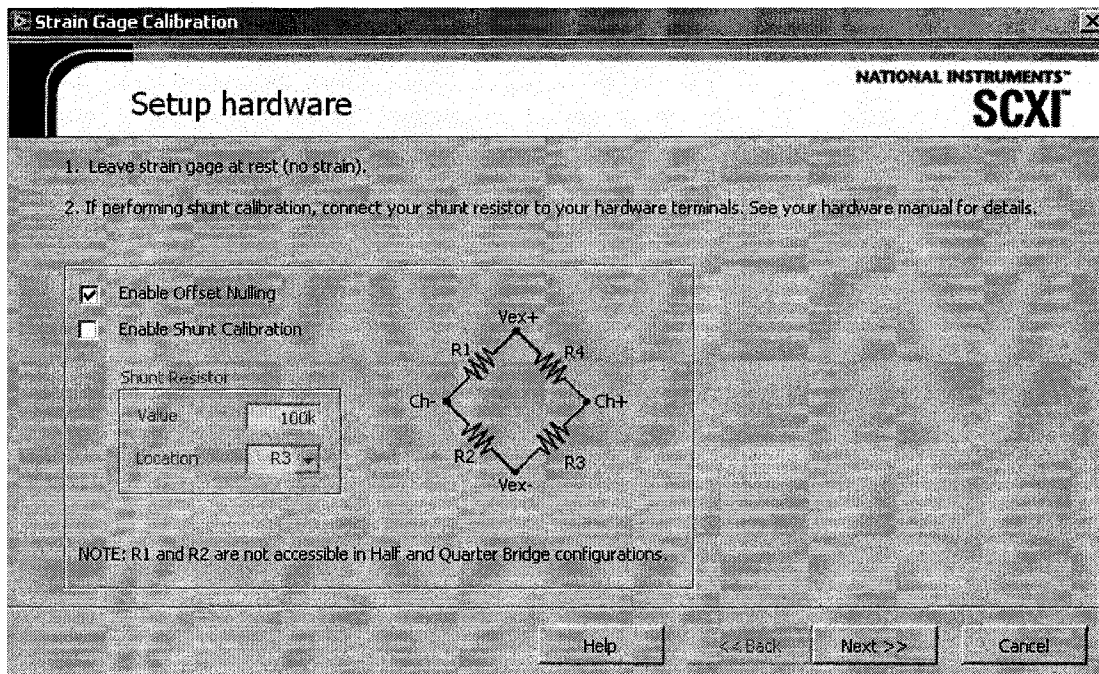

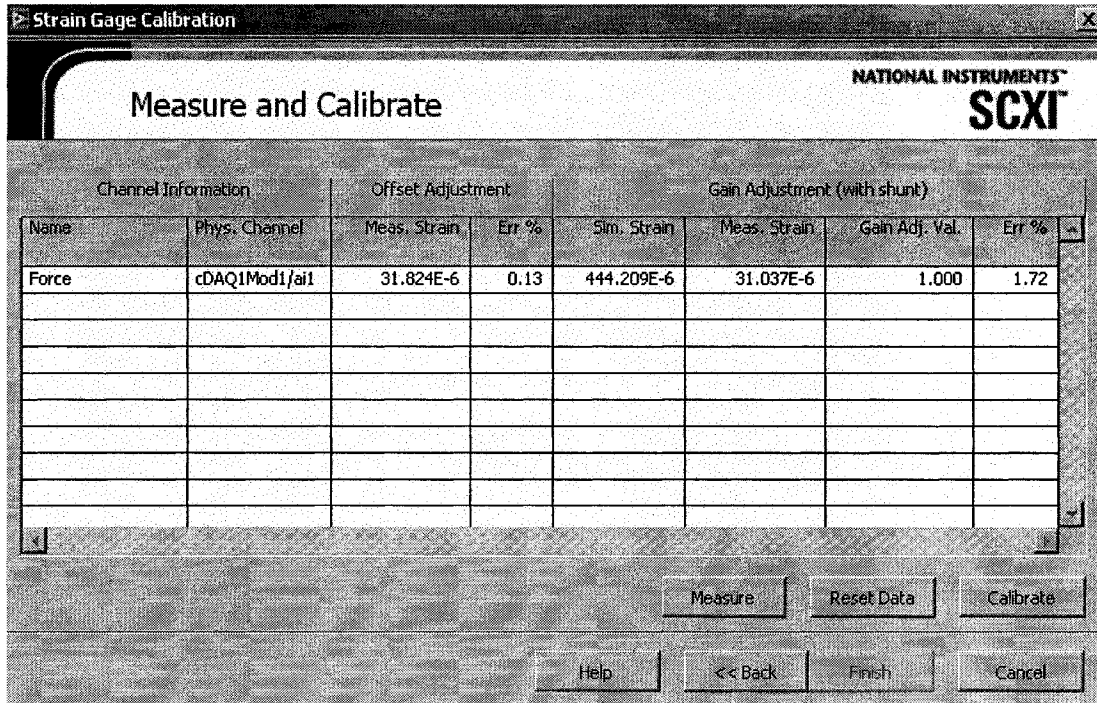Figure A54 Strain Calibration window

142

Figure A55 Strain Calibration, Next window

<u>Signal Input Range</u> (Figure A55): If the Signal Input Range was not in range, an error message showed up. The range would have to be modified according to values shown.

<u>bender.vi parameters – Write to Measurement File:</u>

Double click on 'Write to Measurement File' in the schematic diagram (Figure A50) to open the window shown in Figure A56.
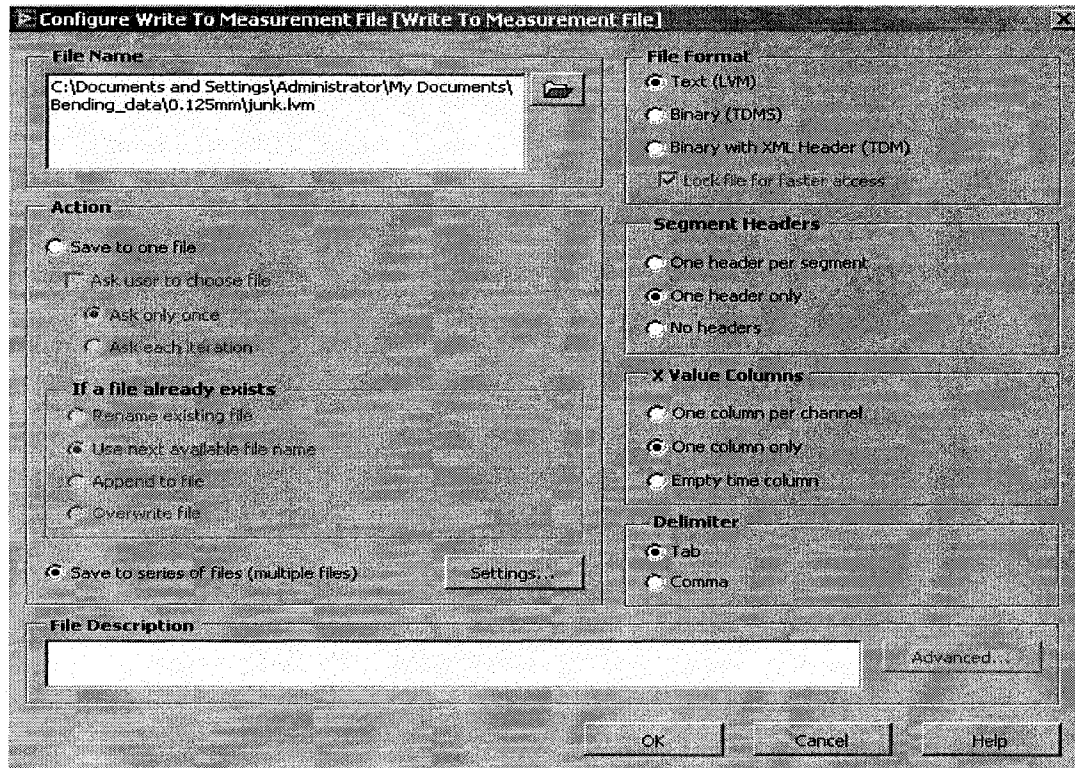
143

Figure A56 Writing data parameters

File name: Files were named in sequence of tests – sample_001.lvm, sample_002.lvm etc. at a pre-specified location.
File format: Text (LVM)

Placing samples:

1.5mm – 0.25mm: Samples were placed towards one end of the punch.
0.127mm – These had to be placed towards the middle of the punch to provide more uniform loading (Figure A58).

Placing them towards the end resulted in an uneven loading as shown Figure A57, which may have been due symmetry errors in the punch.
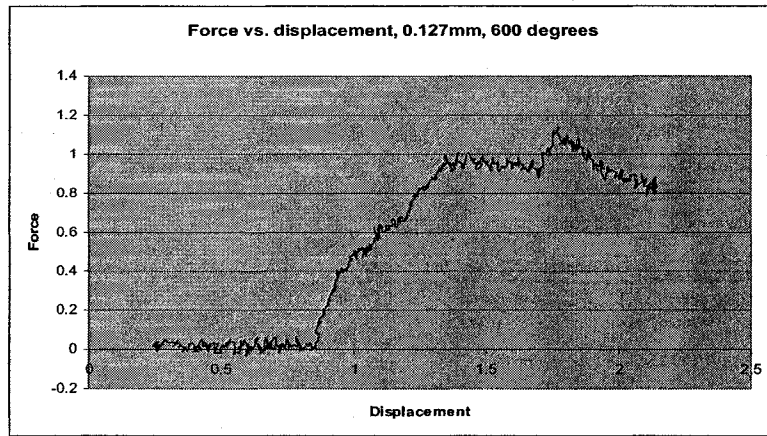
144

Figure A57 Punch force versus punch displacement plot for a non-uniformly
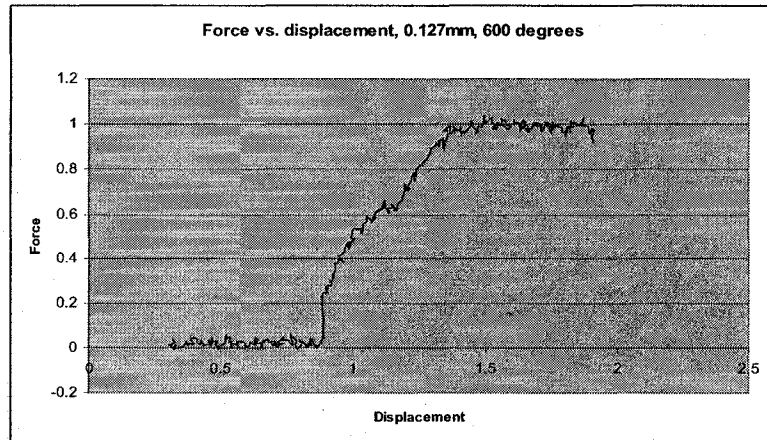loaded 0.127 mm 1100-H18 Aluminum specimen

Figure A58 Punch force versus punch displacement plot for a uniformly loaded
0.127 mm 1100-H18 Aluminum specimen

Depth of Stroke:

A depth of 8t was used for most tests. However, for some cases, 8t was not
sufficient. Some tests were then conducted at 9t to assure a peak force was
reached as the force data may still have been increasing.

145

APPENDIX B

Implementation of FEA Using Marc Mentat

Table B12 FEA Implementation details

Attribute	Details of implementation
Mesh	Element #11 quad
Geometric properties	Planar – plane strain – thickness = 10, assumed strain,
Material properties	Isotropic elastic – E=110 GPa, v=0.34 Anisotropic plastic K_0, K_{45}, K_{90} and n_0, n_{45} & n_{90} for α brass
Contact	Contact bodies :- deformable (sheet), rigid (punch) & rigid (die) All bodies touching with no friction
Boundary conditions	Fixed displacement of all nodes on the left edge
Load cases	Load case 1 & 2: Static Multi-step criteria: Convergence testing: Relative/absolute - displacements Time – 1 sec for each case
Job	Mechanical – plane strain, large strain, updated Lagrange with Multiplicative decomposition

146